EXPULSION INVESTIGATION AND FRACTURE CHARACTERISTICS IN SPOT WELDED ADVANCED HIGH STRENGTH AUTO STEELS

by

Chao Ma

Bachelor of Science in Material Science & Engineering
Electrical Engineering
Harbin Institute of Technology, China, 1995 &1996

A thesis presented to Ryerson University
in partial fulfillment of the requirements for the degree of
Master of Applied Science in the Program of Mechanical Engineering

Toronto, Ontario, Canada, 2006

AUTHOR'S DECLARATION

I hereby declare that I am the sole author of this thesis.

I authorize Ryerson University to lend this thesis to other institutes or other individuals for the purpose of scholarly research.

Chao Ma

I further authorize Ryerson University to reproduce this thesis by photocopying or by other means, in total or in part, at the request of other institutions or individuals for the purpose of scholarly research.

Chao Ma

BORROWER'S PAGE

Ryerson University requires the signature of all persons using or photocopying this thesis. Please sign below provide address and date.

Name	Address	Date

Expulsion Investigation and Fracture Characteristics in Spot Welded Advanced High Strength Auto Steels

© Chao Ma, 2006
Master of Applied Science
in the program of
Mechanical Engineering
Ryerson University

Abstract

Increased use of advanced high strength steels in resistance spot welding (RSW) is necessary for manufacturing safe and affordable vehicles. Unfortunately, the investigation of expulsion monitoring and control of advanced high strength steels (AHSS) is limited. A data acquisition system was designed for monitoring weld expulsion via the measurement of voltage, current, dynamic resistance, electrode force and displacement. Three control strategies were proposed on the basis of the rate of change in the dynamic resistance, the electrode force and the electrode displacement.

Micro-hardness tests, tensile shear tests and fatigue tests were carried out. The expulsion effects on the mechanical properties, fracture modes, and metallurgical features were investigated using optical microscopy, scanning electron microscopy (SEM) and energy dispersive spectroscopy (EDS). Fatigue crack initiation locations were also observed, which were verified by the theoretical stress analysis. In addition, the causes of interfacial fracture were discussed in relation to weld parameters.

ACKNOWLEDGEMENTS

I would like to thank my supervisors Dr. S.D. Bhole and Dr. Daolun Chen for their guidance, support and generosity during my studies at Ryerson University. It is a fortunate opportunity to have two inspired individuals as advisors. Their support and encouragement from different perspectives are highly beneficial to not only my academic research but also my future professional life.

I would like to thank in particular Mr. Gary Boudreau (Market Development and Product Applications, Dofasco), Andy Lee and Elliot Biro (Research and Development department, Dofasco) for their clear explanations, guidance and valuable time.

I am grateful to Natural Sciences and Engineering Research Council (NSERC) of Canada, Premier's Research Excellence Award (PREA), Canada Foundation for Innovation (CFI), Materials and Manufacturing Ontario (MMO), and Ryerson Graduate Scholarship (RGS) for the financial support and Dofasco Inc. Canada for allowing me to use their facilities.

I would like to extend my thanks to all my friends and colleagues at Ryerson University for helping me and keeping my spirits up. Special thanks are owed to R. Churaman, A. Machin, Q. Li and J. Amankrah for strong support to easy access to the facilities.

Last but not least, I would like to express my deepest gratitude to my loving wife for her persistent encouragement, emotional support, and great patience.

TABLE OF CONTENTS

LIST OF TABLES

LIST OF FIGURES

NOMENCLATURE

Acronym	Definition
A/D	Analog to digital
AHSS	Advanced high strength steels
A/SP	Auto/steel partnership
BEI	Back-scattered electron image
CP	Complex phase steel
DAS	Data acquisition system
DC	Direct current
DP	Dual Phase steel
DQSK	Drawing quality and special killed
EDS	Energy Dispersive X-ray spectrometry
FEM	Finite element method
GUI	Graphical user interface
HAZ	Heat Affected Zone
HDG	Hot-dipped galvanized
HSLA	High strength low alloy steel
HSS	High Strength Steels
ID	Identification mark
IF	Interstitial free steel
JIS	Japanese industrial standards
MART	Martensitic steel
MFDC	Medium frequency direct current

MWS	Minimum weld size
OM	Optical microscope
PID	Proportional-integral-derivative
PIF	Partial interfacial fracture
RD	Rolling direction mark
RMS	Root mean square
RSW	Resistance spot welding
RWMA	Resistance Welding Manufacturing Alliance
SAE	Society for automotive engineers
SCR	Silicon controlled rectifier
SEI	Secondary electron image
SEM	Secondary Electron Microscopy
SWS	Stabilization weld size
TRIP	Transformation-induced plasticity steel
UHSS	Ultra-High Strength Steels
ULSAB-AVC	Ultra light steel auto body - advanced vehicle concepts
UTS	Ultimate tensile strength
WS	Weld spacing
YS	Yield strength

Symbol		Units
I	Welding current	kA
60G	Coating weight of zinc	g/m^2
H	Heat generated during welding	Cal/gm
R	Resistance	Ω
R_b	Bulk resistance of material to be welded	Ω
R_e	Contact resistance at the electrode-sheet interface	Ω
R_s	Contact resistance at the sheet-sheet interface	Ω
T	Welding time	Cycles
t	Sheet thickness	mm

Definitions

Anchor Weld	The first of two welds made on a peel test sample.
Coupon	A single, small piece of test material with specified dimensions that is used to make up test samples.
Current	The effective (RMS) welding current of a spot weld that is measured at the secondary side of the welding transformer.
Current Range	Also known as "weld lobe" is the difference in welding current between the Imin and Imax currents on lobe diagram.
Current Setting	The programmed welding current (in kA) of an electronic spot weld controller that is capable of constant current control or the % Heat or % Current setting that is used to

	set the welding current on some constant-voltage-type welding controllers.
Depth of Field	The ability of maintaining focus across a field of view regardless of surface roughness.
Effective Welding Current	The integrated current (amperage) of a weld that is equivalent in its heating or power capability to pure DC (direct current).
Electrode Face Diameter	The mean diameter of the electrode surface (which contacts the sheet surface) before the electrode is dressed. This dimension is the as-ordered or as-machined diameter measured prior to electrode installation.
Expulsion	The ejection of molten metal from the faying interface (interface between the two test coupons) of the sample. Expulsion may be verified by destructive peel testing of the sample and observing whether metal "whiskers" or "fingers" are evident at the interface.
Fracture or Pullout Mode	The failure pattern of the weld button after peel testing.
Full Interfacial Failure	A spot weld fracture mode where the entire weld nugget (fused area of a spot weld) fails through the plane of the weld.
Micro-hardness/ Metallographic Sample	A test sample (taken from one of the hold time sensitivity panels) that is sectioned across the centerline of the weld (perpendicular or parallel to the length of the sample from which it is extracted), mounted, polished,

	and etched for metallographic examination and micro-hardness testing.
Minimum weld size	The minimum weld-button size is calculated by using the following formula: MWS = $4\sqrt{t}$, where t = avg. sheet thickness in mm, rounded to the closest 0.01 mm, and where MWS is rounded to the closest 0.1 mm.
Panel Coupon	A coupon used to make up a panel sample.
Panel Sample	A stackup of two panel coupons used for making rows of welds during the weld quality endurance test.
Partial Interfacial Failure	A spot weld fracture mode where part of the weld nugget (fused area of a spot weld) fails through the plane of the weld and some portion of the weld pulls out as a partial button.
Peel Test	A destructive test for spot weld quality and button size that involves mechanically separating the lap joint by peeling.
Peel Test Coupon	A coupon, cut from a coupon strip in with its length parallel to the direction of rolling, used to make up a peel test sample.
Peel Test Sample	A lap-joint test sample, composed of two peel test coupons having a specified overlap and standard size, which is used to determine weld button size and fracture mode of a resistance spot weld.
Rolling Direction Mark	A mark made prior to coil-edge removal along the coil edge of a steel sheet, as shown in Figure 3.3, that

	identifies the rolling direction. Also see the definition of Transferred RD Mark.
Shear Tension Test	A destructive test to measure spot weld strength and button size with the test weld in the same plane (shear orientation) as the applied load.
Shear Tension Coupon	A coupon, cut from a coupon strip (see Figure 3.8) in accordance with Table 3.4 with its length parallel to the direction of rolling, used to make up a shear tension test sample.
Shear Tension Sample	A lap-joint test sample, composed of two shear test coupons having a specified overlap and standard size, that is used to determine the shear strength of the test weld and its fracture mode.
Stabilization Weld Size	The stabilization weld size, used during the electrode-face and weld-size stabilization procedure, is calculated by using the following formula. SWS = 0.9 X target dressed face diameter SWS is rounded to the closest 0.1 mm.
Test Weld	The weld made on any sample that is to be used to determine weld size, weld strength, and/or button fracture mode.
Weld Button	The part of a spot weld, including all or part of the nugget, which tears out during destructive testing of welded samples.
Weld Button Size	The average of the minor and major dimensions of the weld button.

% Current.	The designation for the control used to set the welding current on some constant-voltage welding controllers.
% Heat	The designation for the control used to set the welding current on some constant-voltage welding controllers.

CHAPTER 1

INTRODUCTION

Automotive companies are increasingly leaning towards the use of more advanced high strength steels (AHSS) to reduce weight and improve performance of optimal crashworthiness (passenger safety), superior formability, and weldability [1]. The most common AHSS steels include the dual-phase (DP) steels, complex-phase (CP) steels, transformation-induced plasticity (TRIP) steels, and martensitic (MART) steels. The higher initial work hardening rate along with the excellent uniform and total elongation combine to give much higher ultimate tensile strength and lower yield strength (YS) to ultimate tensile strength (UTS) ratio than conventional steels or high-strength low-alloy (HSLA) steels of similar yield strength [2]. The preferred fabrication method is resistance spot welding (RSW) for its simple and cheap operation with typically 2,000 to 5,000 welds in a vehicle assembly [3]. The challenge of using the thinner coated AHSS steels in the industry is that they are readily inclined to exhibit expulsion. Also, the presence of the coating results in the accelerated degradation of the welding electrodes, leading to earlier expulsion and frequent replacement or re-dressing of the electrodes [4]. The causes of expulsion are both technical and human related. Technically, expulsion can be avoidable in most circumstances if suitable welding schedules are used, sufficient force is applied, the material surface is well prepared, and the electrodes are in good condition. For human related factors, the automobile industry believes that the occurrence of expulsion yields good information on weld melting which is used as a

visual indicator of a "correct" welding process, a quality assurance evaluation [4]. To achieve a weld size as large as possible to meet certain requirements, the prevalent practice for uncoated low carbon steels is to use a large welding current, which often deliberately exceeds the expulsion limit in production to reduce variations in weld quality caused by random factors [5, 6]. However, for the coated high strength steels, this practice reduces the weld strength due to the loss of metal and the formation of discontinuities such as voids and porosity, and also leads to an easily corroded weld surface [5, 7]. It is, therefore, important to have the capability to monitor or predict expulsion events so that modifications to welding parameters or other remedial actions can be initiated to reduce the incidence of expulsion.

Moreover, in automotive industry and testing labs, the definition of the quality of the spot welds can differ. Accordingly, the tests and criteria used to distinguish the bad welds are different. Among all quality control tests, peel tests and pry checking tests are simple and easy to do, thus widely used in the plant. Static tensile shear tests and fatigue tensile shear tests are the two common testing methods to observe quantitatively the mechanical properties of spot welded joints [8]. The tensile shear and fatigue test performance of spot welded joints has been a significant factor in vehicle design.

The purpose of this study is to evaluate the weld quality by detecting and classifying the expulsion with multiple sensors simultaneously for a hot-dipped galvanized (HDG) DP600 steel, observe the fracture characteristics of spot welded specimens from the tensile shear test and tensile fatigue test which is related to the load mode,

and then study the fatigue crack initiation with experimental and theoretical analysis. Possible strategies for the process control are also discussed.

CHAPTER 2

LITERATURE REVIEW

2.1 Introduction to Resistance Spot Welding

RSW is a major sheet-metal joining process in many industries, such as the automotive and appliance industries. Elihu Thompson invented this process in 1877[3]. RSW applications have grown enormously since the first sheet-welded automobile was introduced in 1933. Due to the higher joining speed, RSW machines can be associated with automated robotic welding cells in a car assembly plant.

RSW, which is normally performed on pedestal welders, consists of a power supply for generating large currents and a pneumatic cylinder for applying a force on the metal sheets to be welded. After the electrodes squeeze the sheets, a large current is applied through the workpiece. The heat produces the temperature which exceeds the metal melting point to generate a molten nugget. The amount of current can be controlled by adjusting the conducting angle of a silicon controlled rectifier (SCR) with a microcontroller-timer [8]. The electrodes are water cooled, so the metal to electrodes contact is kept below the melting point. RSW is an extremely fast process involving electrical, thermo-mechanical and metallurgical variables. Complexity also arises from the variety of base metals to be welded, coating on the surface, and types of welding machines. Commercially available machines include pedestal press type welders and various gun-type welders, e.g., C-gun and scissor gun welders.

The power source of these guns can be single phase AC, three phase AC or medium frequency DC (MFDC) [3].

2.1.1 Principle of Resistance Spot Welding

Figure 2.1 shows a schematic diagram of the spot welding operation. Two or more metal sheets (base metals) are placed between two water-cooled copper electrodes and are subjected to a large squeeze pressure. A relatively large current is then passed at a low value of voltage through the sheets being welded. The resistance offered to the flow of electric current produces heat. The heating (H) is related to the electrical power input, expressed as [8],

$$H = K * I^2 * R * T \tag{2.1}$$

where, K is the heat loss factor, I is the current, R is the resistance and T is the time for which weld current is passed through the sheets (weld time).The heat produced causes the interface to melt and form a solid joint. The joint formed at the interface of the two sheets (faying interface) is called a 'button' or 'nugget'.

The total resistance 'R' between the two electrodes consists of three components: the bulk resistance of the sheet, R_b, the contact resistance at the electrode-sheet interface, R_c, and the contact resistance at the faying interface, R_f. Thus, for sheets of the same material and equal thickness [8],

$$R = 2R_b + 2R_c + R_f \tag{2.2}$$

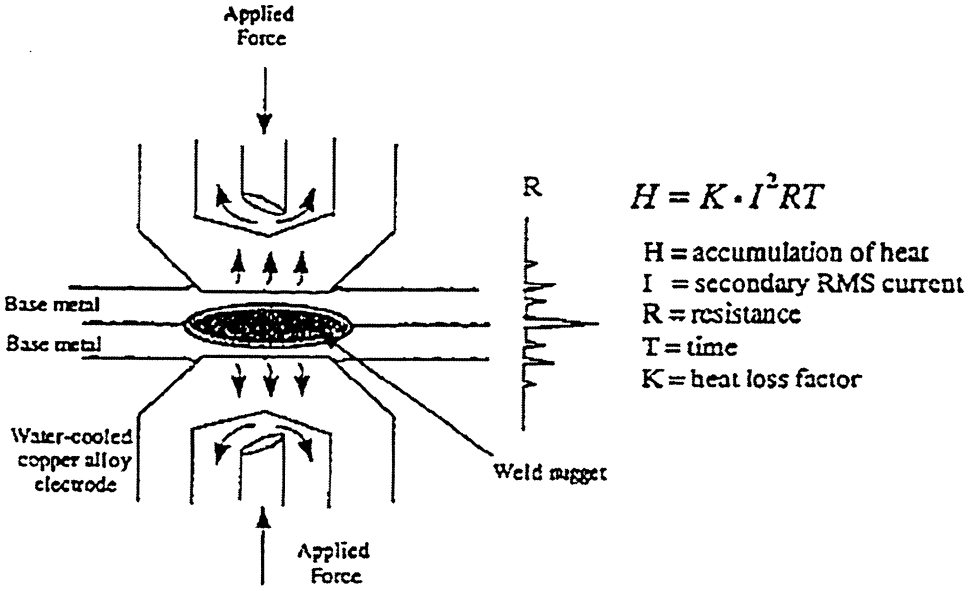

Figure 2.1 Principle of resistance spot welding. [8]

The maximum resistance to the flow of current is offered by the faying interface [9]. Therefore, the maximum heat is generated at the faying interface causing a local fusion.

The electrodes transmit sufficient pressure to upset the joint slightly to produce a better joint. The amplitude and duration of the welding current must be controlled accurately to facilitate the growth of the nugget. A typical spot welding operation is controlled by a weld schedule, whose time steps are controlled by a spot welding controller. A weld schedule is usually divided into four steps, as shown in Figure 2.2:

1. Squeeze time, or the time between the first application of electrode force and the first application of welding current.

2. Weld time, or the actual time the current flows.

3. Hold time, or the period during which the electrode force is applied and the welding current is shut off.

4. Off time, or the period during which the electrodes are not contacting the workpieces.

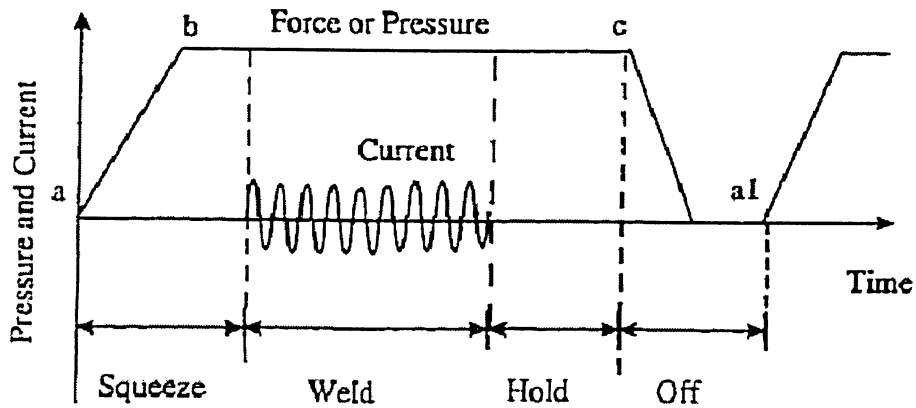

Figure 2.2 An illustration of a weld schedule. [3]

Burn-through, cracks, porosities and distortion are avoided by controlling the heat input through suitable current and weld time selection. During the spot welding of two sheets, a joint should be formed at the faying interface and not at the electrode-sheet interface. The cooling water circulated inside the electrodes avoids excessive electrode heating and joint formation (sticking) at the electrode-sheet interface [8].

2.1.2 Nugget Growth and Expulsion Phenomenon in RSW

Among the four stages, squeeze, weld, hold, and off, the weld stage is important. During the weld stage, the interface melts to form a solid joint. The joint formation in galvanized steels (steels coated with zinc) is different from that of uncoated steels [10-15].

During the squeeze cycle (Figure 2.2), the sheets are squeezed between the two electrodes. There is no thermo-mechanical phenomenon taking place during this stage. When two metal sheets are brought into contact, their surfaces will touch only at points where the tips of asperities on one surface meet those of the other. With increasing pressure, these asperities will flatten, but the actual points of contact will only be a fraction of the apparent contact area.

Once the current begins to flow, the regions of points of contact will heat up and soften, thereby allowing other asperities to touch and become heated. This process continues until the entire area softens and all the asperities come into contact. Thus, for the first few welding cycles, the breakdown of insulating films and asperities takes place. The fall of asperities is much faster for galvanized steels due to the softness and low melting temperature of zinc [14,15]. In zinc-coated steels, surface film breakdown and contaminants form local hot spots that may be detrimental to the electrode tip life. The first few cycles involve heating of zinc and Fe-Zn alloys on the electrode-sheet interface and melting of zinc coating at the faying interface. The molten zinc will then start to be forced away from the centre of the electrode tips to form a liquid 'halo'. A mechanical seal starts to develop at the periphery of the

electrode contact area. The seal is formed at both the faying and electrode-sheet interfaces. The electrodes are forced through the zinc coating at the periphery. The seal traps the remaining zinc and weld metal between the electrode tips at both interfaces. The increase in the halo size with the formation of the seal leads to an increase in the area of current flow. Then, iron to iron contact formation starts. When a substantial amount of metal reaches the melting or softening temperature, the faying interface collapses to form a softened surrounding material. If the same amount of current continues to flow, the material is abruptly expelled at the sheet-sheet interface. This is called expulsion [8].

The seal formed at the faying interface keeps the substrate (steel) in place as it is heated to the softening temperature, melts and forms a weld. The seal also keeps the material from squeezing out radially. As a result, the material is constrained, and thermal expansion pushes the electrodes apart (away from each other). Once the thermal expansion becomes large enough, the seal is broken and molten metal is suddenly free to expel radially. Another mechanism of expulsion occurs when the molten steel over 1500^0C gets close to the zinc boiling point at 907^0C [14]. This boiling zinc may force the electrodes apart and expel both zinc and iron. Figure 2.3 shows a typical example of the expulsion.

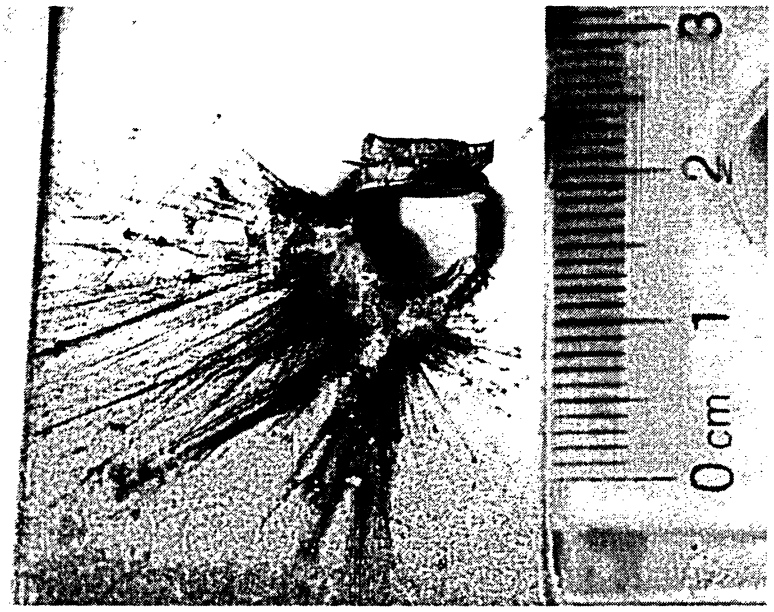

Figure 2.3 Nugget expulsion showing breaking of zinc halo and metal seal.

2.2 Recent Studies on Expulsion Monitoring and Control

It has been shown that expulsion can be identified from the most widely used parameters for sensing: (1) electrical variables: secondary voltage, primary or secondary current, dynamic resistance; (2) mechanical variables: electrode force, and electrode displacement [6,10,16-18]. Various other techniques have been used in the laboratory or for assembly, such as ultrasonic method, acoustic emission method, and infrared technique [19-22]. Expulsion has been studied in terms of both detection and prediction based on the above parameters [3].

2.2.1 Recent Studies on Expulsion Detection

For expulsion detection, many methods have been developed. Dickinson et al. [11] designed a monitoring device to simultaneously record the voltage, current, power, and resistance and analyzed the relationship between these parameters and the nugget formation. They proposed that resistance and energy input could be used to control the process for the uncoated steels. However, there is some inaccuracy due to the low sampling rate. Gould and Peterson [12,13] evaluated nugget development and dynamic parameters with the help of voltage, current, resistance and electrode displacement for uncoated HDG, electrogalvanised drawing quality and special killed (DQSK) low carbon steels. They found that each group was quite different in its nugget development behaviour. Gedeon *et al.* [10,14,15] developed methods to reduce the errors in the measurement of the voltage, current, dynamic resistance, force, and displacement for uncoated, HDG and galvannealed low carbon steels. They concluded that, for both steels, the dynamic resistance and displacement curves provided significant information while force curves were of little use since the inertia of the welding head reduced the response sensitivity. Chien and Kannatey-Asibu [6] investigated acoustic emission, electrode displacement, force, and dynamic resistance to correlate with the nugget formation for a HDG low carbon steel. They found that force signals provide the most information on the nugget formation. Apparently, Chien and Kannatey-Asibu [6] and Gedeon *et al.* [10] have conflicting conclusions for the electrode force signals. Farson *et al.* [23] monitored the expulsion via measurements of voltage, displacement and force change for small scale RSW of stainless steels. They reported that all signals have features that correlate with the

occurrence of the expulsion. Podržaj *et al.* [24] designed a neural-network-based system to analyze mild steels and zinc-coated low carbon materials with dynamic resistance, force, and displacement signals, which worked well using only the amplitude of the welding force variation. Meur *et al.* [25] reported an experimental study on the electrothermal contact at the electrode-sheet interface during the RSW which showed that the developed experimental methodology was reproducible and reliable for the measurement of temperature, as well as the estimation of two temporal functions: the thermal resistance of the contact and the partition coefficient of the generated heat flux at the interface. Jou [26] explored a relationship between the percentage heat input and the electrode displacement as a monitoring method for bare and HDG DQSK and high-strength steels. In the spot welding of aluminium, Hao *et al.* [17,27] developed a system to detect the expulsion with several criteria from voltage, displacement, force, and dynamic resistance signals. Using a mid-frequency direct current (MFDC) welder, Ji and Zhou [28] characterized electrode displacement and force for an aluminum alloy and proposed two possible process control strategies. However, the characteristics of spot welds between aluminum and steel using MFDC welder have been shown to be different from those of AHSS steels using AC welder [17,27,29].

2.2.2 Expulsion Prediction Methods with FEM

For the prediction of expulsion and welding process, there are a number of modelling studies using the finite element method (FEM). For expulsion prediction, Zhang [7] analyzed and compared three expulsion prediction models on their merits,

applicable areas and limitations, and concluded that the statistical model directly linked expulsion to welding schedules. Senkara *et al.* [5] developed an expulsion model based on the consideration of the interaction between mechanical and metallurgical processes, which was verified by experiments on an aluminum alloy. One of their conclusions was that the model was equally applicable to other materials. Many attempts to simulate the welding process have employed one- and two-dimensional models [30,31]. More realistic modelling [32-34] has been obtained using finite element packages using their coupled electrothermal analysis. Some investigators have attempted to quantify the resistance mathematically [35-37] and analyze the electrode wear [38-41] which is the key factor for the process prediction accuracy of any model. These models still have some limitations due to inadequate input data to describe the transient conditions in the weld zone [3,4,42,43]. Therefore, direct measurement of process signals seems to be a better way if the process is to be monitored and controlled effectively based on these parameters [28].

2.2.3 Classical Control Techniques

Based on microprocessor techniques, the weld timer is an important part of the welder when it comes to ensure good reproducibility in the conditions from one weld to the next. The timer works synchronously with the main frequency (60Hz). During the actual welding process, the current is measured and corrected through triggering SCR with the rising edge of the clock signal. To keep the nugget diameter big enough and stable from weld to weld, the current density per unit area must be the same. Considering the electrode wear, electrodes need to be dressed and thus the

current stepping function need to be used to compensate for the increase of the tip area. The weld timer is programmed to increase the current in steps to match the enlargement in the contact surface. Certainly, the data which are followed by the timer come from the lobe test experiments: current, force, as well as other parameters chosen to input into the program in a microcontroller [8].

2.2.4 Adaptive Control Techniques

An adaptive controller differs from an ordinary controller in that the controller parameters are variable, and there is a mechanism for adjusting these parameters on-line based on signals in the system.

Real time process control is required to compensate for the electrode wear, oxidized metal surfaces, and part fit-up anomalies. The spot welding machine and process have many control challenges associated with nonlinearities such as time delays, load piston friction, workpiece expulsion and process gain changes. The welding control has to identify these process parameter variations within 10 milliseconds and provide control action within 100 milliseconds to produce a good weld.

Based upon the thermal growth related to nugget formation, Haefner *et al.* [44] designed a real-time adaptive RSW control to derive thermal growth from a measurement of electrode displacement, utilized a least square observer to monitor the electrode displacement, a PID (proportional-integral-derivative) model reference controller, a Smith predictor to compensate for time delays, and a shaped

displacement trajectory command for regulating the heat to the workpiece. Material thermal expansion was used as a control variable detected with a digital optical encoder. Through the adaptive control, the dynamic resistance, which is unknown and time varying, could be obtained using a model-reference adaptive control method or self-tuning method.

The spot welding process exhibits variations from the nominal values which must be compensated for by adaptive control. These variations are exhibited as long-term changes which occur over a period of many welds or the variations may occur between single welded points. The long-term variations are generally related to the electrode/workpiece wear or changes in the machine calibration. The short-term variations in the welding process occur as a result of the changes in the contact resistance. The standard procedure for non-adaptive control in RSW relies on a manual adjustment of a constant heat bias at the start of each shift or setup to compensate for variations in the machine and the electrodes. The manual adjustment requires frequent off-line measurements of the weld nuggets on coupons between periods of welding parts and does not compensate for the process parameter variations which occur during the weld. The adaptive control compensates for the variations of each weld and the real time process changes (from weld to weld).

The real time spot welding adaptive control embodies several novel control techniques which are integrated in a unique combination to provide a method of

controlling the weld nugget size over a wide range of process variability. These components are [44]:

1. Least square estimator as an observer.

2. Pre-compensator for shaping the target displacement command.

3. Model reference control with Smith predictor and PID compensator.

4. Control logic.

However, the reference model of the adaptive control method is difficult to build and may need to be designed individually for different materials, coatings, and welders.

2.2.5 Artificial Intelligence (AI) techniques

AI techniques, relying less on mathematical process representation, may be ideal for controlling the highly non-linear process of RSW. It is felt that a combination of the neural network, with its mapping and pattern recognition capabilities, and a fuzzy logic controller, with its ability to handle vague and imprecise data, is likely to offer great benefits in overcoming the limitations of existing control systems [4].

Araki *et al.* [45] studied the on-line control of a spot welding machine using a fuzzy adaptive algorithm. Chen *et al.* [46] proposed an algorithm that can evaluate the weld bonding quality of spot welding using a fuzzy estimation. However, this algorithm was not industrially applicable because it required too many input variables and

fuzzy rules. In addition, it had the potential of failing local minima because its design point was bound to the range of tensile strength.

Lee *et al.* [47] developed a neuro-fuzzy Inference system that used an electrode separation signal and dynamic resistance for inferring the tensile strength of resistant spot welds of 0.8mm zinc-coated steel. In selecting the key parameters, an electrode separation signal measured by a laser displacement sensor was selected when no expulsion occurred. The current was measured by a toroidal coil sensor. The system was established by applying a learning process to the parameters as described above and the static tensile strength.

The sequence of events in such a control system would be [47]:

1. Develop satisfactory mathematical models, independently if necessary, to account for heat generation and weld growth in the weld zone, together with the prediction of weld size/microstructure.

2. Use the results of the model to optimize inputs into a neural network.

3. Additional inputs should be considered and chosen from general experimentally-developed trends or monitored variables. These inputs would then be fed into the appropriate neural network.

4. The output from the neural network would then be input into a fuzzy logic controller in order that corrective action can be initiated.

Also, it is most essential that the predictive models should take into account the effects of electrode deterioration since the electrode wear changes many parameters used to formulate the control algorithms. Unless this can be done, the model becomes a research tool only with little benefit to the production.

2.3 Testing of Spot welds

There are some drawbacks of RSW, such as the inability to produce quality welds consistently, and the lack of a reliable and effective quality evaluation method [3]. In the automotive industry and testing labs, the definition of the quality of the spot welds can vary [4]. Accordingly, the tests and criteria used to distinguish the bad welds are different [48]. Among all quality control tests, peel tests and pry checking tests are simple procedures for the quality test, which are especially easy to be applied in the plant. Static tensile shear tests and fatigue tensile shear tests are the two common testing methods to evaluate quantitatively the mechanical properties of spot welds [8]. The tensile shear and fatigue test performance of spot welds continue to be an important consideration in vehicle design.

2.3.1 Lobe Test

Spot weldability of a specific material can be determined with the weld lobe diagram. Welding force, current, and time are the three major parameters that determine the nugget size. They can be controlled on a welding machine. Given certain electrodes, different materials require different combinations of the parameters to produce

acceptable welds. A graph showing the function of the nugget size with the current and time under a certain force level is usually developed to guide the machine setup. This type of graph is called a weldability lobe due to the shape of the area as shown in Figure 2.4. Two curves divide the current-time plane into three regions. From lower-left to upper-right, the three regions are no weld or undersized weld region (resulting in a nugget smaller than the minimum acceptable diameter $4\sqrt{t}$, where t is the sheet thickness), good weld region, and expulsion region (resulting in expulsion or burn through) [3,8,48].

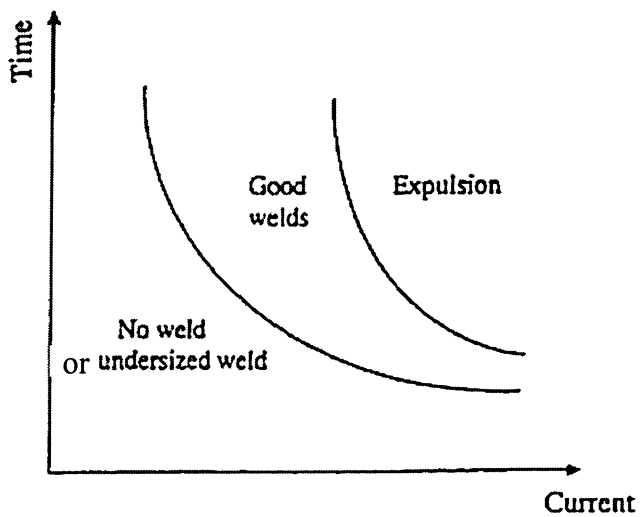

Figure 2.4 A typical weldability lobe. [3]

If the welding parameters are set along any point on the left curve, and a peel test sample is welded with these parameters (I and T), the peel test will result in a minimum acceptable nugget diameter ($4\sqrt{t}$) on the test weld. Welding parameters set

along the right curve will produce expulsion on the test weld. The points inside the lobe curve will guarantee a weld with an acceptable nugget size. Since the weld strength is directly proportional to the weld diameter, an acceptable nugget size represents acceptable weld strength.

At a specific welding time, the current range in which an acceptable button diameter can be formed is called the 'lobe width' [48]. The lobe width at a specific welding time can be calculated from the lobe diagram by subtracting I_{min} from I_{max}. A larger (robust) lobe width represents a bigger window for the selection of welding parameters and vice verse. A lobe width larger than 2000 A is the acceptable lobe width for uncoated steels and 1500 A for coated steels.

Researchers found that weld lobe widths and their positions depend upon the type of coating, as well as the amount of coating (coating weight) [49]. In general, coated steels have less contact resistance and higher currents are necessary to weld them. Electrode tip wear is an important issue for spot welding of coated sheets. Howe and Kelley [49] showed that coating was constantly being picked up by the electrodes. Zinc on the electrode face changes the topography and electrical characteristics of the electrode face. The degree of topography change depends on the welding conditions and type of coated sheet being welded.

2.3.2 Peel Test and Weld Button Criterion

The peel test consists of peeling apart a spot weld manually. If correlated with the tensile shear test, it makes an ideal control test. The weld button is measured with a calliper and the average diameter, $\overline{D}$, is calculated as follows (see Figure 2.5) [8,48]:

$$\overline{D} = \frac{D+d}{2} \tag{2.3}$$

where, D and d are the maximum and minimum axes according to the pertinent rules, respectively. For crescent, oval, or other irregularly shaped buttons, the calliper is rotated until D and d are located. Note that D and d are not necessarily perpendicular to each other.

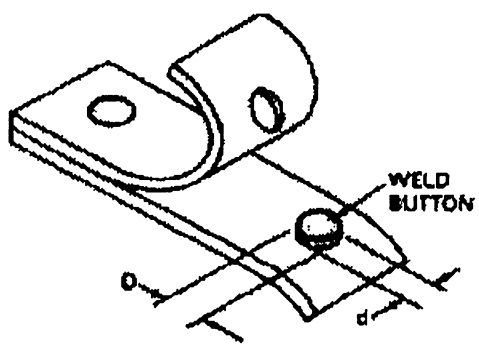

Figure 2.5 Peel test and diameter measurement. [8]

If the calculated nugget $\overline{D}$ is not within specified limits, the welding parameters are adjusted to get the required size of the nugget. The volume of the button plays an

important role as almost all mechanical properties of the spot welded joint are related to it. The weld diameter is directly proportional to the joint strength. The spot weld is said to be good if the average nugget diameter is between the following minimum and maximum nugget diameters. The minimum and maximum nugget diameters are defined as follows [48],

D_{max} = Diameter at the expulsion current,

$D_{min} = 4\sqrt{t}$, where t = the sheet thickness.

2.3.3 Microhardness Test

Specimens are prepared, exercising care to avoid overheating of the weld area in cutting so as not to affect the surface hardness. A second cut parallel to the first should be made to obtain a sample of suitable height to mount in the hardness tester. Figure 2.6 shows a typical hardness test of the cross section of a spot weld.

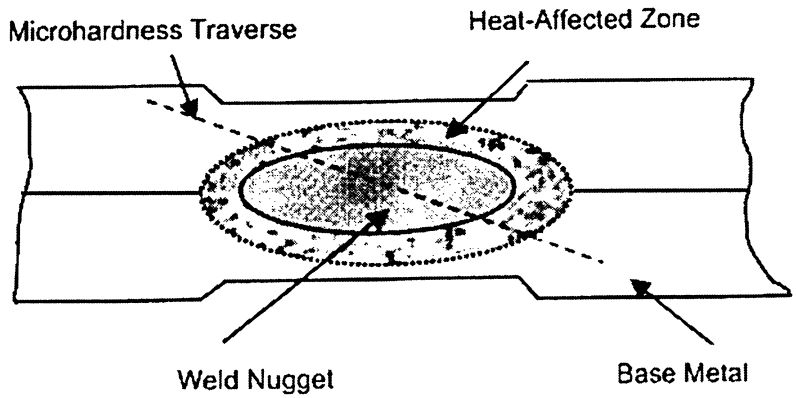

Figure 2.6 Microhardness test on the cross section of weld. [50]

Mililitsky *et al.* [50] investigated the metallurgical features and formation of imperfections in DP600 spot welds. They found no heat-affected zone (HAZ) softening for DP600 as shown in Figure 2.7.

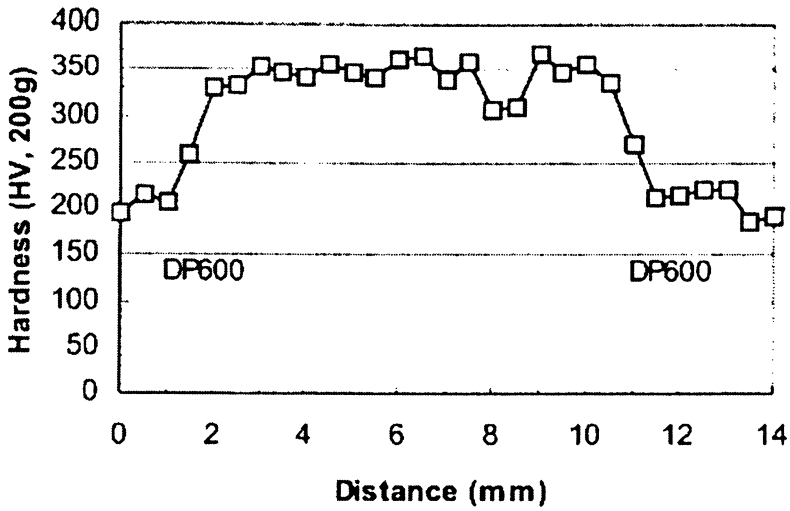

Figure 2.7 Microhardness profile with a hold time of 30 cycles. [50]

2.3.4 Tensile Shear and Fatigue Test

The tensile shear test consists of pulling apart spot welded specimen on a tensile testing machine [48]. In a satisfactory tensile shear test, the weld nugget remains unimpaired and fracture occurs around the periphery of the joint as shown in Figure 2.8 [8].

There are two methods commonly used for fatigue testing depending upon the shape of the specimen [8].

1. Tensile shear fatigue test.

2. Cross tension fatigue test.

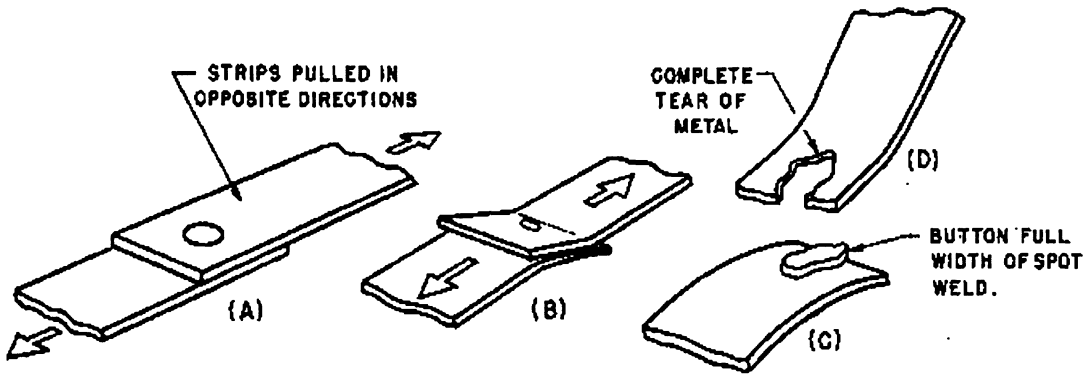

Figure 2.8 Tensile shear test. [8]

Tensile shear specimens can be used to evaluate spot weld fatigue behaviour and to generate data for durability analysis. The load capacity of the testing machine should be compatible with the strength of the spot welds tested. Due to the small load needed to deform the specimen, the machine should be equipped with a specimen protection system to reduce the preload during specimen mounting. The test system shall be verified before initiation and after completion of the program in accordance with ASTM E4, ASTM E467 and ASTM E1012 or the machine shall be calibrated every year [8,48].

2.3.5 Typical Button Failure Modes

Figure 2.9 shows various fracture modes that can be observed from a peel test [51].

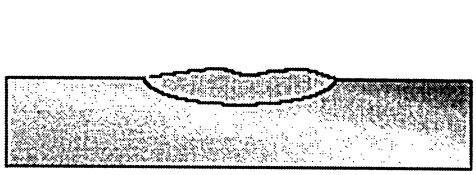

(A) Interfacial Fracture

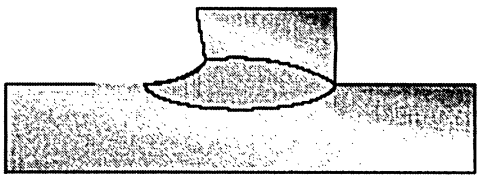

(B) Irregular fracture

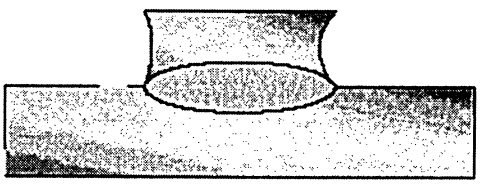

(C) Full button pullout

Figure 2.9 Fracture modes in peel test. [51]

Full button pullout failure modes represent better joint strength and good weld conditions than interfacial or irregular button failures. Interfacial fracture modes are not acceptable failure modes. They represent a weak joint and cracks travel through the weld. In addition to the weld button criterion, the welds should look uniform and have a small indent from the electrode tip. The buttons, which have diameters in the

range of minimum to maximum button diameters and show full button pull-out fracture mode, are called acceptable button diameters [51].

2.4 Recent Studies on Fatigue of DP600

While testing DP600 samples, the interfacial fracture button mode was found, especially with the thicker gauges [52-54]. W. Peterson *et al.* [51] reviewed the weld mechanical properties versus the fracture button modes in the form of button pull-out, thickness fracture, interfacial fracture and no fusion. A. Joaquin *et al.* [54] studied the effect of several factors on RSW, including the effect of the welding power source, electrode tip shape, welding current, material type and thickness, and hold time. Shrinkage voids were found to be one of the main causes for interfacial fracture from tensile shear static and fatigue tests. Some techniques were also developed to reduce shrinkage voids in order to decrease the potential interfacial fracture in resistance spot welds of AHSS. M. Milititsky *et al.* [50] investigated the tensile shear test samples for DP600, and observed shrinkage, solidification cracks and liquid metal embrittlement in some welds. Some factors affecting the formation of the imperfections were discussed, such as weld current and hold time. Some researchers [55,56] reported that high-cycle fatigue lives were independent of strength and microstructure of base materials for three high strength uncoated steels - HSLA, DP, and TRIP, as well as one low strength DQSK steel. They believed that the high-cycle fatigue performance is controlled by sample geometry alone, such as weld nugget size, sheet thickness, and the corresponding joints stiffness. However, HDG DP600 may have different results due to the effect of zinc embrittlement [50].

One of the most important characteristics of fatigue cracks in spot welded joints is the crack initiation location. Cooper and Smith [57] developed a direct current potential difference technique for the measurement of the crack dimensions and concluded that macrocrack propagation dominated the fatigue lives of the order of 2×10^6 cycles. Wang and Barkey [52] investigated the spot weld fatigue crack initiation and propagation processes with an X-ray imaging method and found that the initiation location of the fatigue cracks was 0.2-1.0 mm from the nugget edge of the spot weld. Finite element and theoretical analysis were conducted to identify the maximum stress concentration away from the nugget root. Rathbun *et al.* [55] concluded that the fatigue crack nucleated at a tongue structure of the sheet interface that resulted from the molten material, which was forced out from the weld nugget. But the materials used are all uncoated to avoid the complicated effects from zinc coating.

2.5 Objectives of Research

The enhanced strength of AHSS comes from a higher percentage of carbon and other alloying elements like manganese, nickel, etc. However, the higher carbon equivalent results in a lower weldability, i.e., a small lobe width at a specific welding time. Moreover, the coated zinc makes the welding more challenging and prone to early expulsion, which may severely affect the strength of the weld, surface quality and electrode life.

The present work is aimed at designing a data acquisition system (DAS) to conduct a detailed study of weld schedules so as to understand and predict the onset of weld expulsion in DP600 steel. Variables such as current, electrode force, and welding time that contribute to the expulsion are studied to predict and control the expulsion. Control strategies will be proposed based on the study of the above variables. The fracture surface of failed specimens of tensile shear and fatigue tests will be examined to identify the fatigue crack initiation location and fracture modes in relation to the microstructure change, weld defects, and microhardness.

CHAPTER 3

EXPERIMENTAL PROCEDURE

The current chapter presents the material selection, sample preparation, data acquisition system for detecting the expulsion, equipment and settings for tensile test, fatigue test, microhardness test, optical image analysis system, scanning electron microscopy (SEM), and energy dispersive spectroscopy (EDS).

3.1 Materials and Samples Preparation

This section summarizes the procedure followed for preparing peel coupons, panel coupons, and tensile shear coupons from the supplied sheets. The welded samples were prepared according to Auto/Steel Partnership procedures [48].

The ULSAB-AVC (Ultra Light Steel Auto Body - Advanced Vehicle Concepts) is the most recent addition to the global steel industry's series of initiatives offering steel solutions to the challenges facing automakers around the world to increase the fuel efficiency of automobiles, while improving safety and performance and maintaining affordability. Consistent with the terminology adopted for ULSAB, High Strength Steels (HSS) are defined as those steels with yield strengths between 210 and 550 MPa; Ultra-High Strength Steels (UHSS) are defined as steels with yield strengths greater than 550 MPa. The yield strengths of Advanced High Strength Steels (AHSS) overlap the range of strengths between HSS and UHSS, as shown in Figure 3.1. The principal differences

between conventional HSS and AHSS lie in their microstructures. AHSS are multi-phase steels, which contain martensite, bainite, and/or retained austenite in quantities sufficient to produce unique mechanical properties. Compared to conventional micro-alloyed steels, AHSS exhibit a superior combination of high strength with good formability. This combination arises primarily from their high strain hardening capacity as a result of their lower YS/UTS ratio [2].

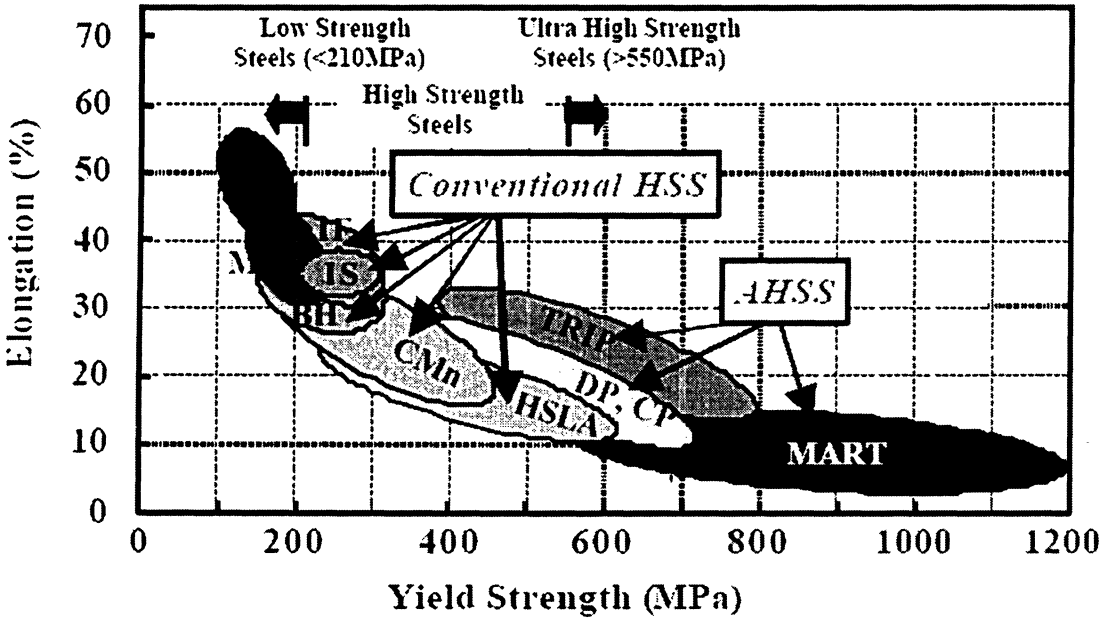

Figure 3.1 Strength-Formability relationships for conventional HSS, and AHSS steels. [2]

The multi-phase AHSS family includes dual phase (DP), transformation induced plasticity (TRIP) and complex phase (CP), and martensite (MART) steels. Figure 3.1

shows the relative strengths and formability (measured by total percent elongation) of conventional strength steels and AHSS steels [2].

The microstructure of DP steels is comprised of soft ferrite and, depending on strength, between 20 and 70% volume fraction of hard phases, normally martensite [2]. Figure 3.2 displays the microstructure of a DP ferrite + martensite steel with 636 MPa UTS. The soft ferrite phase is generally continuous, giving these steels excellent ductility. When these steels deform, the strain is concentrated in the lower strength ferrite phase, creating a unique high work hardening rate exhibited by these steels. The work hardening rate along with the excellent elongation combines to give DP steels much higher ultimate tensile strength than conventional steels of similar yield strength.

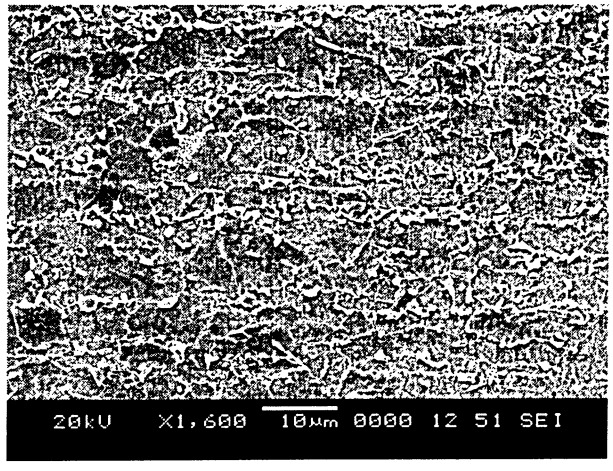

DP600 - 4% Nital Etch

Figure 3.2 Microstructure of DP steel. (Ferrite – grey; Martensite – light)

The material selected in this study is a HDG DP600 steel, which is a popular material for the rocker component in an auto body. (The exact chemical composition is

proprietary information.) The typical mechanical properties of the test material are shown in Table 3.1.

Table 3.1 Mechanical properties of base materials.

Zinc coating weight (g/m^2)	Sheet thickness (mm)	YS (MPa)	UTS (MPa)	Total elongation (%)
74	1.24	370	636	27

3.1.1 Peel and Panel Coupons

DP600 was supplied in the form of sheets sheared to a size of 1200 mm x 1200 mm full coil width. The test materials were sheared so that the transferred "top surface" identification (ID) mark appears on all strips, panels, and coupons of coated sheet steels. The transferred rolling direction mark is only required on all coupon strips prior to coupon shearing and on the material characterization panel. Individual test or panel coupons do not require a rolling direction (RD) mark. About 100 mm of sheet from each sheet coil edge (X and Y in Figure 3.3) were sheared and scrapped to eliminate any potential effects of edge coating weight and sheet thickness variations on the test results [48].

After trimming edge X, the rolling direction mark was transferred to the sheet surface as shown in Figure 3.4. Two types of strips, called peel coupon strips and material characterization panel were sheared from the sheet. Peel coupons were sheared from the peel coupon strip. The material characterization panel was used for determining sheet thickness, coating weight, as well as coating and substrate composition [48]. Figure 3.4 shows a typical layout for extracting peel coupon strips from a trimmed sheet.

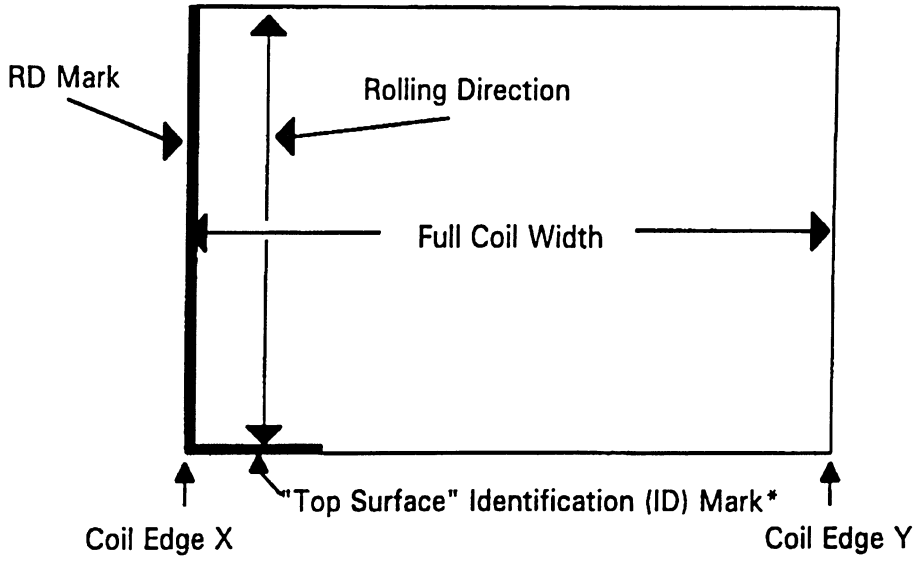

Figure 3.3 Surface and rolling direction marking of sheet. [48]

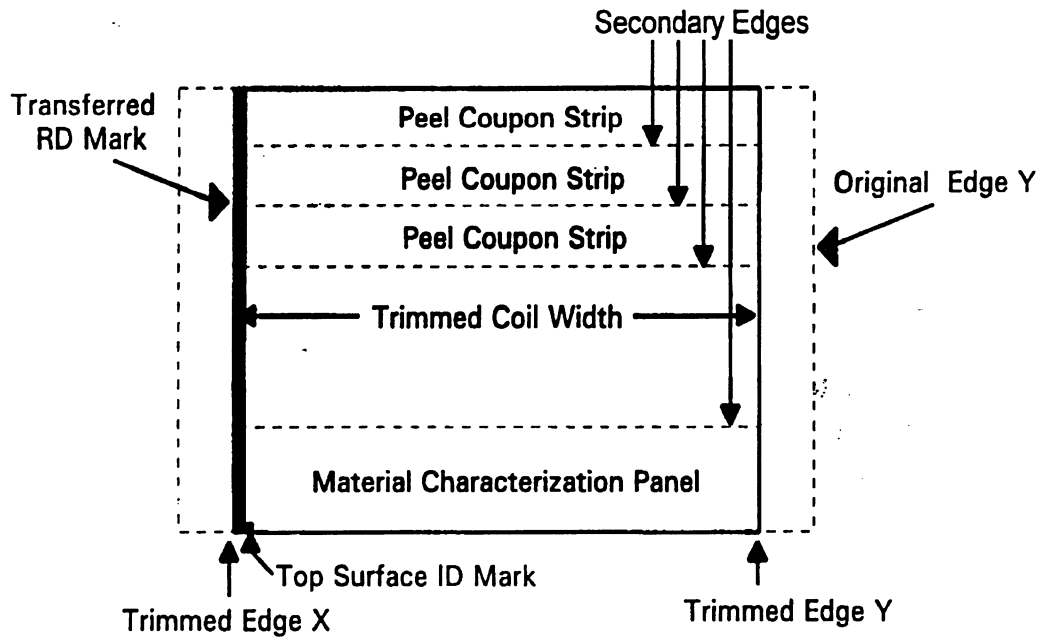

Figure 3.4 Trimmed coil width with transferred RD mark on sheet. [48]

Figure 3.5 shows a layout for shearing peel coupons from peel coupon strips. Figure 3.6 shows peel test coupons and samples for 0.9-1.29 mm thick steel sheets with the details of dimensions given in Table 3.2. Using the RD mark as a reference, top surface ID marks were transferred to the secondary edge of each test coupon strip, as shown in Figure 3.5. Special attention was given to keep the transferred RD mark on each strip. From the trimmed test coupon strip, the desired numbers of test coupons were sheared. About 600 peel coupons are necessary for establishing one lobe diagram.

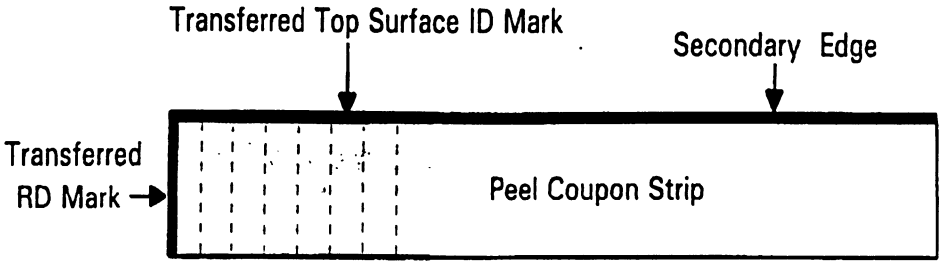

Figure 3.5 Peel coupons sheared from the test coupon strip. [48]

Table 3.2 Dimensions for peel test coupons and samples. [48]

Sheet Thickness (mm)	L[(a)] (mm)	W[(a)] (mm)	WS[(b)] (mm)	A[(b)] (mm)	B[(b)] (mm)
0.90 – 1.29	120	40	40	20	30

Note: (a) Tolerance: ±1 mm, (b) Tolerance: ±3 mm.

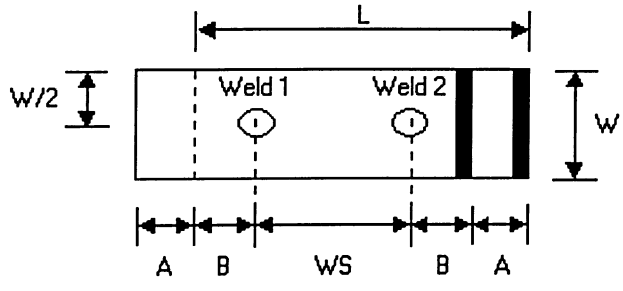

Figure 3.6 Schematic diagram of peel test samples. [48]

Figure 3.6 also shows that the specified weld spacing (WS), given in Table 3.2, shall be maintained between the anchor weld (1st weld) and the test weld (2nd weld) on all peel samples.

Figure 3.7 shows the layout used for cutting the panel coupons. Panel coupons for weld and electrode face stabilization were sheared from the test coupon strips according to the dimensions specified in Table 3.3.

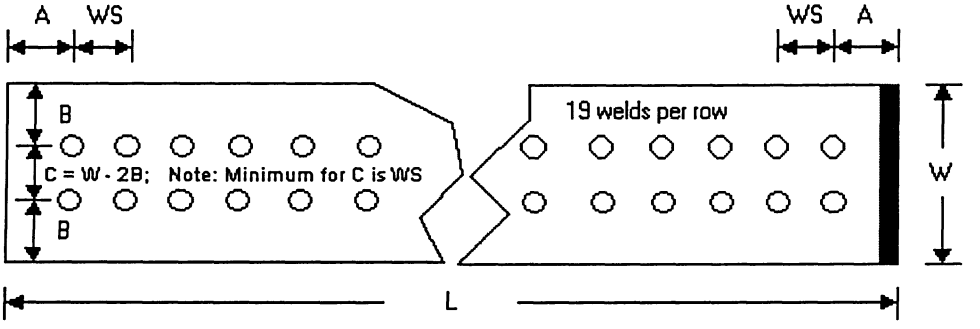

Figure 3.7 Panel coupons sheared from the test coupon strip. [48]

Table 3.3 Dimensions for panel coupon. [48]

Sheet Thickness (mm)	L[a] (mm)	Minimum W[b] (mm)	WS[c] (mm)	A[d] (mm)	B[e] (mm)
0.90 - 1.29	400	64	18	23	23

Note: (a) L = (18 x WS) + 2A + 30; Tolerance: ± 5 mm; (b) W may be increased to ease handling; (c) WS = 3 x dressed electrode-face diameter; Tolerance: ± 3 mm; (d) A = the minimum edge distance; No specific tolerance; (e) Tolerance: ± 3 mm

All peel and panel coupons were kept 'as is' after being sheared to simulate the actual welding conditions.

3.1.2 Tensile Shear Samples

The dimensions for the tensile shear samples are shown in Figure 3.8 and Table 3.4 based on the A/SP standard [48]. Because all test welds on these samples are single welds, the current required to produce the proper weld size may be slightly different from the current that is required for the peel test.

Table 3.4 Dimensions for shear tension samples. [48]

Sheet Thickness(mm)	Coupon Length L[(a)](mm)	Coupon Width W[(b)] (mm)	Overlap O[(b)] (mm)	Sample Length SL[(a)] (mm)	Unclamped Length UL[(b)] (mm)	Gripped Length GL[(a)] (mm)
0.60 -1.29	105	45	35	175	95	40

Since the tensile shear specimen is asymmetrical in its plane, two spacers having the same thickness are welded at the grip sections of the specimen to reduce the sheet bending and nugget rotation. There is also a fixture to be used to easily hold the shear tension samples to be welded.

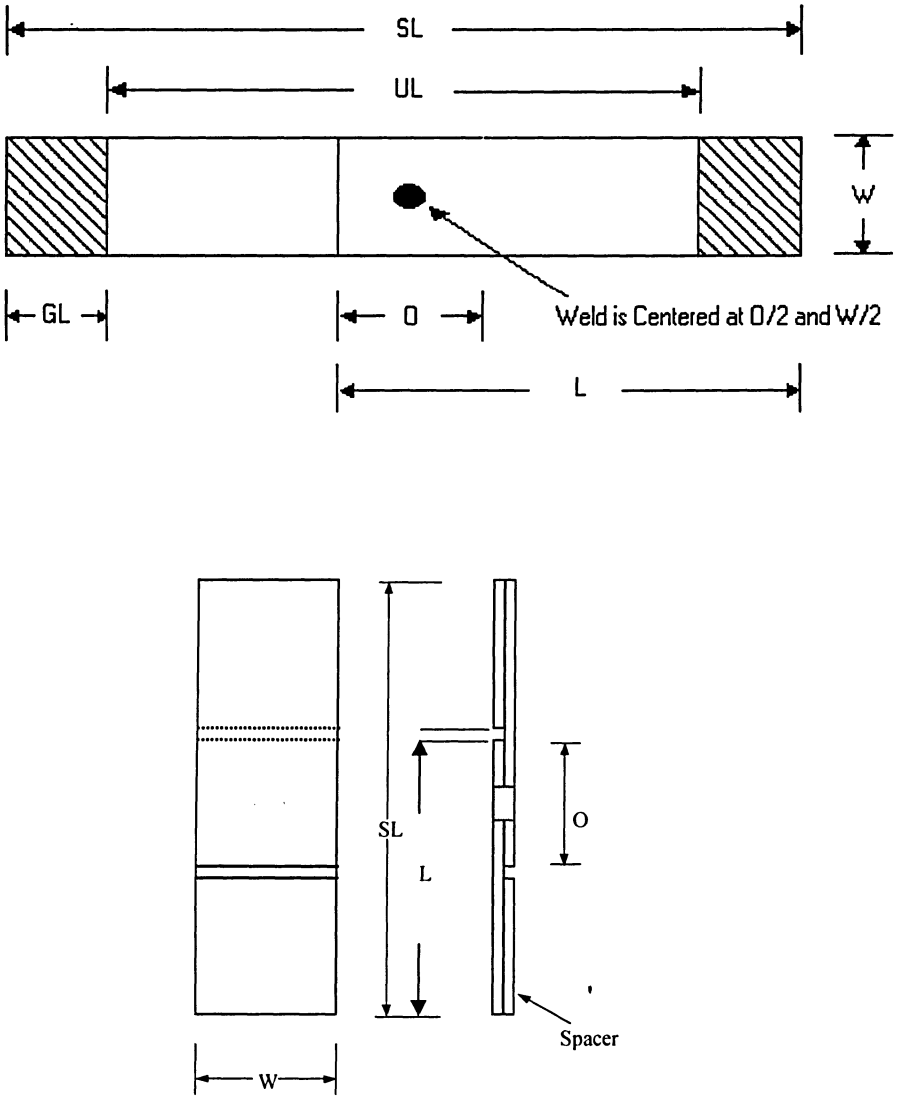

Figure 3.8 Schematic for shear tension samples. [48]

3.2 Equipment and Testing

This section summarizes the equipment and testing parameters followed by the collection of process signals, mechanical testing, and microstructural examinations.

3.2.1 Welder and Related Equipment

Figure 3.9 shows a single phase, 60 Hz (a cycle corresponding to 0.01667 second for a current frequency of 60 Hz), AC, 50 kVA pedestal resistance spot welder used in the present work. The welder has a microprocessor-based digital MEDAR legend control with an automatic voltage compensation. The transformer is capable of producing about a 100 A secondary current increment per 1% current setting increment from 60% to 98%. The electrode force application system is pneumatic.

Figure 3.10 shows a MIYACHI, MM-121 B high precision weld checker used to measure secondary current and time (or cycles) in the present study, which is used to compare with the reading from the DAS. It is capable of measuring and monitoring RMS values of the welding current at the first cycle of AC. The measured values were displayed digitally on the front panel.

The spot welder used in this study has a pneumatic force application system. The required electrode force was set in the spot welder. A piezo electric portable force gauge (Tuffaloy: model 601-8300MD, capacity 3000 lbs) shown in Figure 3.11 was used to check if the required force was maintained across the electrode tips. The tip of the force gauge was inserted between the gaps of two electrodes. A full welding force was applied by pressing the pedal. The force was displayed on the digital display of the force gauge.

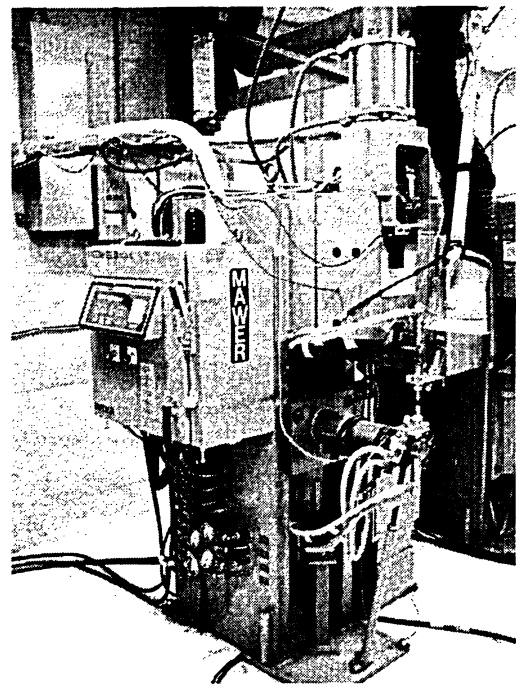

Figure 3.9 A 50 kVA AC spot welding machine.

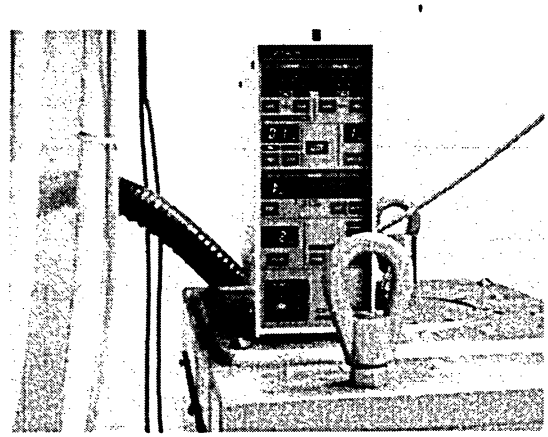

Figure 3.10 MIYACHI, MM-121B high precision weld checker.

Figure 3.11 Portable force gauge (Tuffaloy 601-8300MD).

3.2.2 Welding Parameters

Welding schedules were prepared and implemented based on the A/SP standard and the field practice [48]. Table 3.5 shows the weld schedule for 1.10-1.29 mm thick mild steels.

Table 3.5 Welding parameters for 1.10-1.29 mm thick mild steel sheets. [48]

Sheet Thickness (mm)	Electrode				Weld Time (cy)	Short Hold Time (cy)	Long Hold Time (cy)	Welding Rate (w/min)
	Type No.	Dressed face Dia. (mm)	Force (kN)	Cooling (l/mm)				
1.10 – 1.29	3	6.0	3.1	4.0	14	5	90	20

Three different weld times were selected by adding and subtracting four cycles from the mean weld time given in A/SP schedule. The welding current was set to a value that should result in a "no-fusion" condition on the test weld (i.e., the 2nd weld on the peel sample) at the highest welding time. The welding current was increased in intervals of

100 A by setting the percent current increment in 1%. Once the minimum acceptable nugget diameter ($4\sqrt{t}$) was achieved for a particular weld time, the point corresponding to the current and weld time was plotted on the lobe diagram.

The current was increased by another 100 A and three different peel samples were welded at each welding time (e.g., 10, 14 or 18 cycles). This procedure was repeated until the expulsion was observed on the test weld for each weld time. The expulsion points were also plotted on the lobe diagram. While conducting this procedure, the weld times were selected in a random order. The random sequence of the weld was achieved by selecting a coin randomly from three identical coins, each coin representing a particular weld time. For every material combination under consideration, the final lobe plotted was the average of three different lobes. The detailed weld lobe data can be found in appendix A. Based on the lobe width, a welding time of 18 cycles was chosen to determine the proper welding schedule. The typical welding parameters used in this investigation are given in Table 3.6. Other welding conditions used were 35-cycle squeeze time and 10-cycle hold time based on the field application. Electrodes with a 6.0 mm diameter flat tip end made of copper alloy of RWMA class II were used. The welding currents used for the three groups of fatigue samples were 6.83 kA, 8.14 kA, and 8.54 kA, respectively.

Table 3.6 Typical welding conditions used.

Welding conditions				
Squeeze time (cycle)	Welding time (cycle)	Force (kN)	Hold time (cycle)	Electrode diameter (mm)
35	18	3.34	10	6.0
35	18	2.00	10	6.0

3.2.3 Data Acquisition System

The data acquisition system was set up to measure four variables: tip voltage, welding current, electrode force, and displacement. A schematic of the DAS system is shown in Figure 3.12 [58]. The electrode voltage was measured between the two electrode tips. The current was measured by a toroidal coil attached to the bottom arm and then was integrated to get the actual value of the welding current. The dynamic resistance was calculated from the tip voltage and the welding current. A strain gauge (load cell) was installed on the upper arm of the electrodes to measure the dynamic squeeze force. A digital length gauge was used to measure the electrode displacement. The signal-conditioning box provides the isolation, amplification, and scale for the analog-to-digital (A/D) converter card in the computer. The data acquisition was accomplished with National Instruments Labview software at a sampling rate of 15 kHz per channel. The acquired signals were also processed with a software filter and analyzed with Labview software.

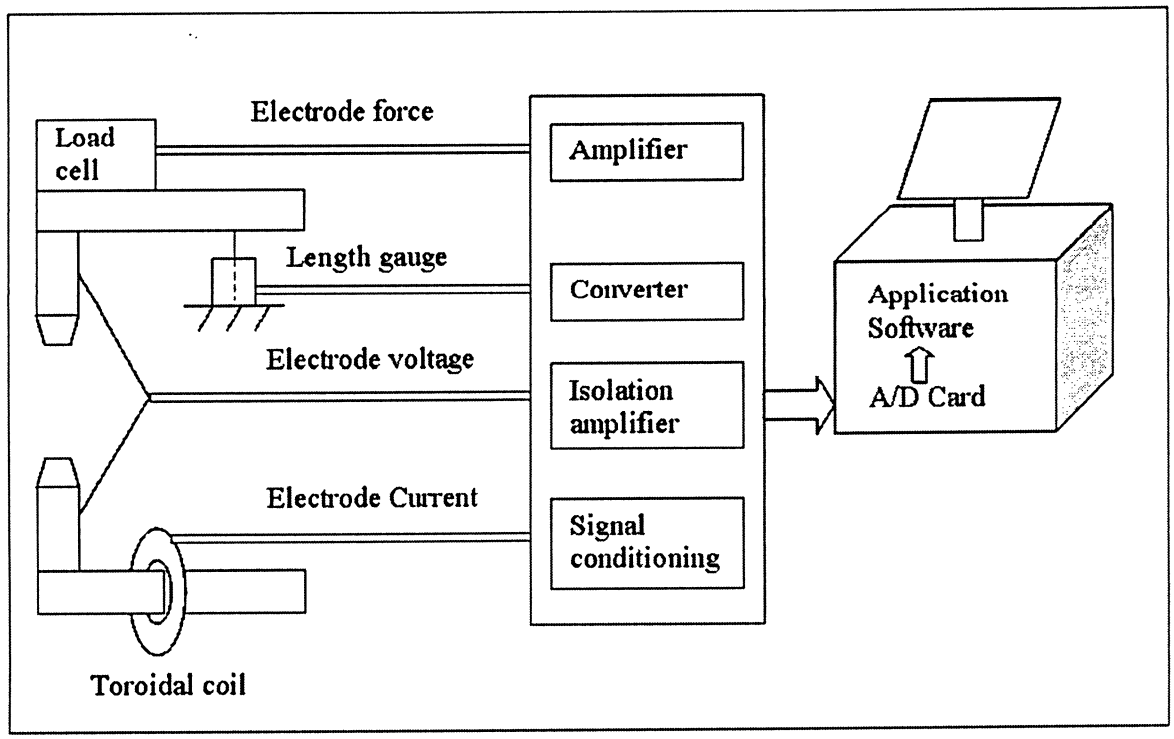

Figure 3.12 A schematic illustration of the data acquisition system. [58]

3.2.4 Equipment and Settings for Peel, Tensile and Fatigue Tests

Figure 3.13 shows digital callipers, locking pliers, edge cutter pliers, tongs, copper lever tube and bench vise used for the peel test [59]. Locking pliers (10 inch) and a copper lever tube were used for pulling the two sheets apart in the peel test. Edge cutter pliers (8 inch) were used for removing burrs and lips from the weld button. Mitutoyo, series 500 Imperial model digital callipers with an accuracy of ± 0.01 mm were used for measuring the button diameter. The measuring method according to the A/SP standard was followed [48]. Typically, three nugget diameters were averaged for each welding condition.

Figure 3.14 and Figure 3.15 show the computerized testing machines for the tensile shear test (SATEC – universal testing machine – model: 60HV with 60000 lb capacity) and the fatigue tests (Instron 8801), respectively. The tensile shear and fatigue tests were conducted based on A/SP and Japanese industrial standards (JIS-Z-3138) [48,60,61]. For the tensile shear tests, a crosshead speed of 10 mm/min was used to capture and qualify the static characteristics of the weld. The fatigue tests were carried out in the load control mode using a sine waveform with a frequency of 50 Hz and a R-ratio (i.e., the ratio of the minimum load to the maximum load) of 0.1. The specimen was mounted in the load control mode under the zero-load set point.

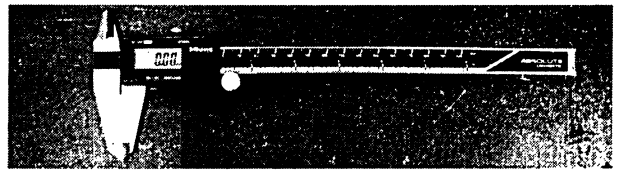

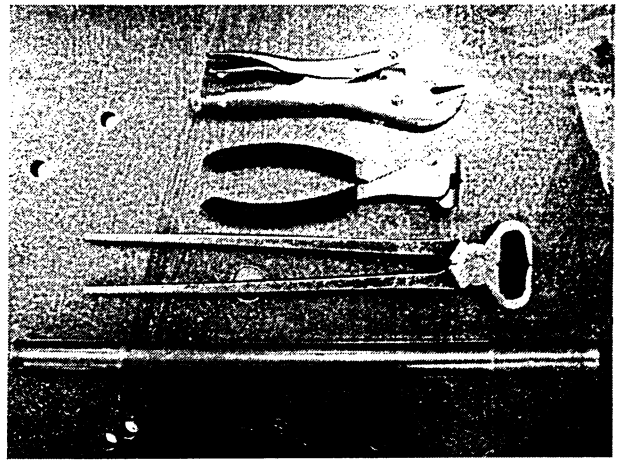

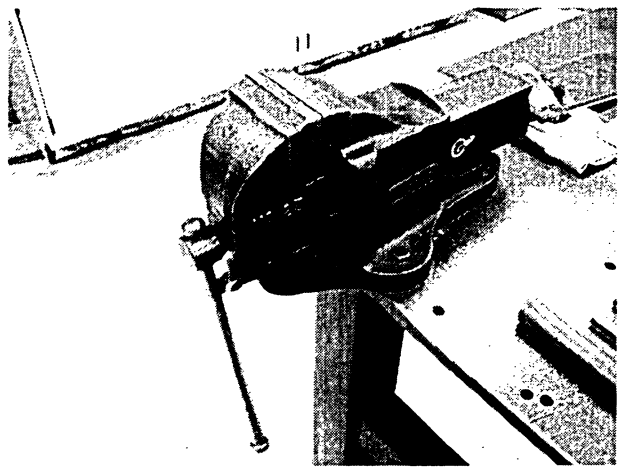

Figure 3.13 Equipment for peel test.

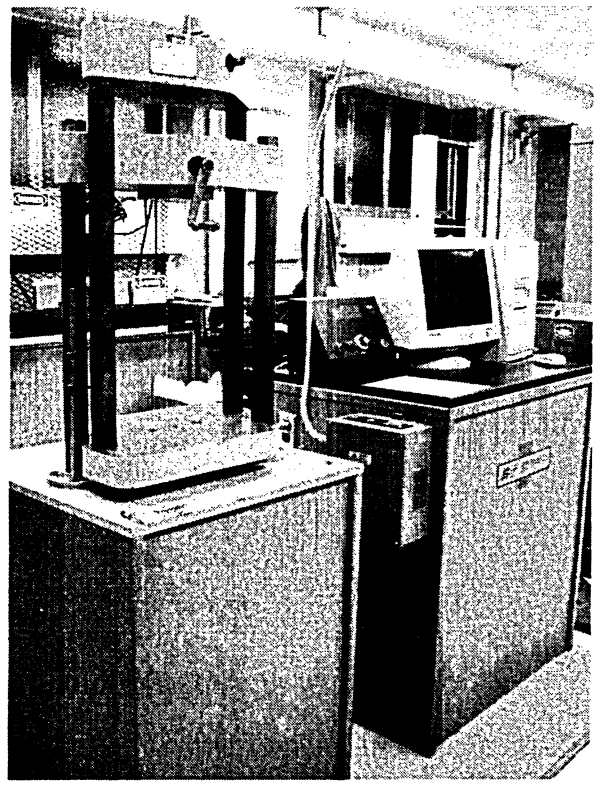

Figure 3.14 Equipment for tensile tests (SATEC 60HV).

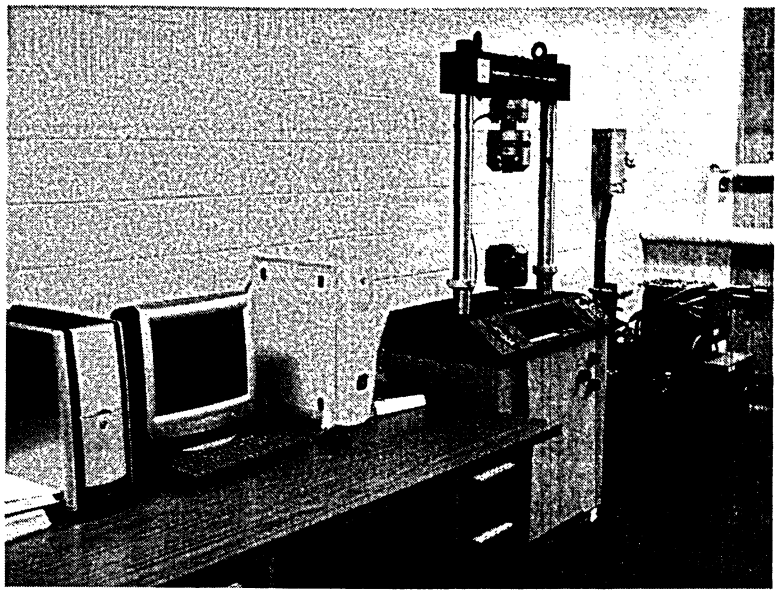

Figure 3.15 Equipment for fatigue tests (Instron 8801).

3.2.5 Microhardness Tester

Spot weld specimens for the microhardness, optical microscopy and SEM were sectioned, mounted, grounded, and polished with carbide paper, diamond paste, and fine colloidal silica [62]. Table 3.7 shows the procedure used for the surface preparation. Automatic mounting machine (BUEHLER SIMPLIMET-2000), and an automatic grinding and polishing machine (LECO AP-60/VP-160) were used, respectively. A BUEHLER MICROMET-5100 was used for the microhardness tests. The microhardness measurements were made at 0.010 inch (0.254mm) intervals using the Vickers scale at an applied load of 500 g, which was converted to Rockwell microhardness. The path of conducting the microhardness tests is shown in Figure 3.16.

Table 3.7 Typical procedures of surface preparation. [62]

Mounting	Bakelite			
Grinding	SiC Grit (Size)	Time (secs)	Wheel Speed (rpm)	Pressure (psi/MPa)
	180	120	300	30/0.21
	320	60	300	30/0.21
	600	60	300	30/0.21
Polishing	6 micron diamond compound/ silk cloth/microid extender	240	250	25/0.17
	1 micron diamond compound/ red felt cloth/microid extender	120	250	25/0.17

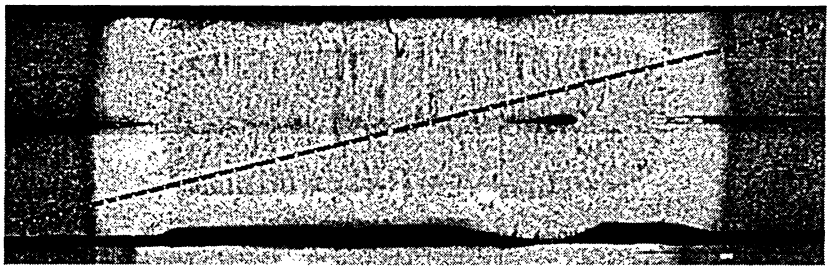

Figure 3.16 The selected path for microhardness tests.

3.2.6 Metallography and Image Analysis

A Clemex image analysis system shown in Figure 3.17 was used for the optical microstructural examination. It is comprised of a Clemex CMT software adaptable to ASTM and ISO standards, a Nikon optical microscope (10X eye piece, five different object lens with magnifications of 5x, 10x, 20x, 40x, and 100x), a high-resolution digital camera, and a high performance computer to carry on the detailed analysis.

The characteristics of weld size were observed in another two ways: (i) from the cross section of the weld nugget as shown in Figure 3.18(a); (ii) from the imprint section of the weld nugget as shown in Figure 3.18(b). The microstructure was observed by the optical microscopy after etching with a solution of 10g picric acid and 100 ml CH_3OH. For analyzing the general microstructure, samples were etched with a 4% Nital reagent.

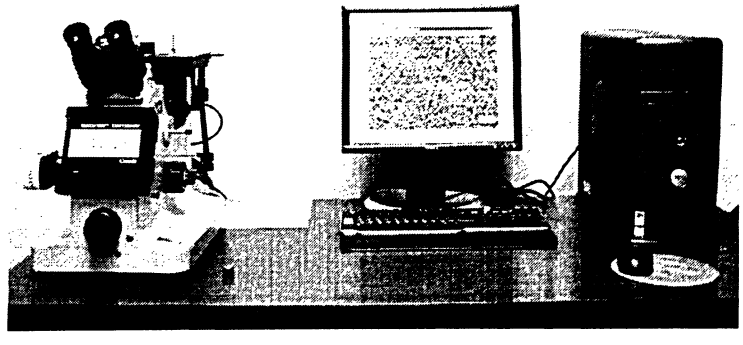

Figure 3.17 Image analysis system (Clemex).

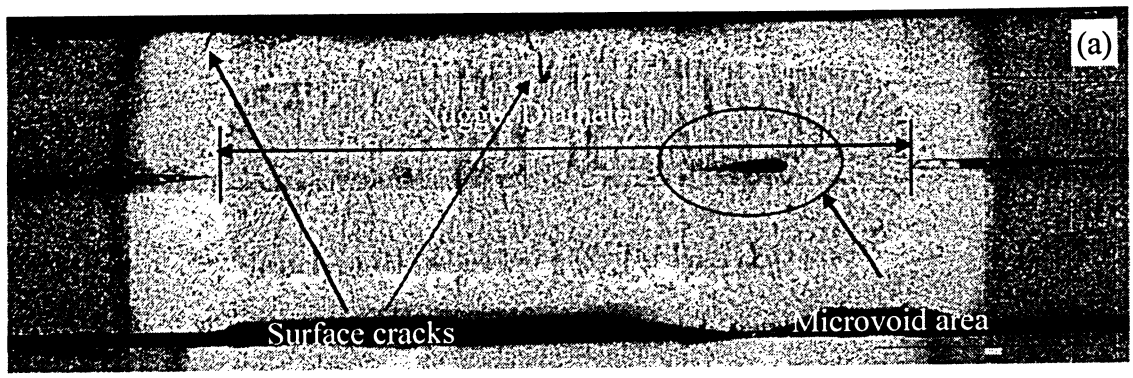

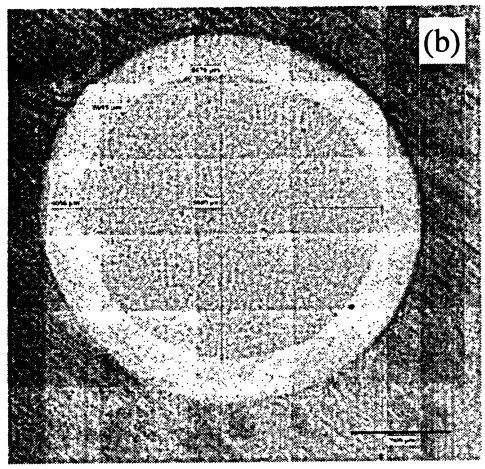

Figure 3.18 Nugget diameter and microstructure examination of spot welds:

(a) Cross section; (b) Imprint section.

3.2.7 SEM and EDS

The microstructures and fracture features at the different regions in the cross section of the spot welds were examined using the SEM. The chemical compositions in the area of interest were conducted using energy dispersive x-ray spectroscopy (EDS), including

high resolution mapping. The JSM-6380LV shown in Figure 3.19 is a high-performance scanning electron microscope with an embedded energy dispersive X-ray analyzer which allows for seamless observations and has a high resolution of 3.0 nm. The customizable graphical user interface (GUI) allows the instrument to be intuitively operated, and Smile Shot™ software ensures optimum operation settings. Standard automated features include auto focus/auto stigmator, auto gun (saturation, bias and alignment), and automatic contrast and brightness [63]. The resolution of the SEM is much higher than an optical microscope (OM) because the electrons accelerated to 10,000 keV have a wavelength of 0.12 Angstroms, while the visible light has wavelengths from 4,000 to 7,000 Angstroms. The typical depths of field for OM and SEM are shown in Table 3.8 [64]. The equipped three detectors – secondary electron detector, backscattered electron detector, energy dispersive X-ray detector, can be used. The general microstructure of the test material was revealed after etching with a 4% Nital reagent.

Table 3.8 Typical depth of field for OM and SEM at different magnifications. [64]

Magnification (X)	OM (μm)	SEM (μm)
10	250	1000
1200	0.08	24
10,000	--	10

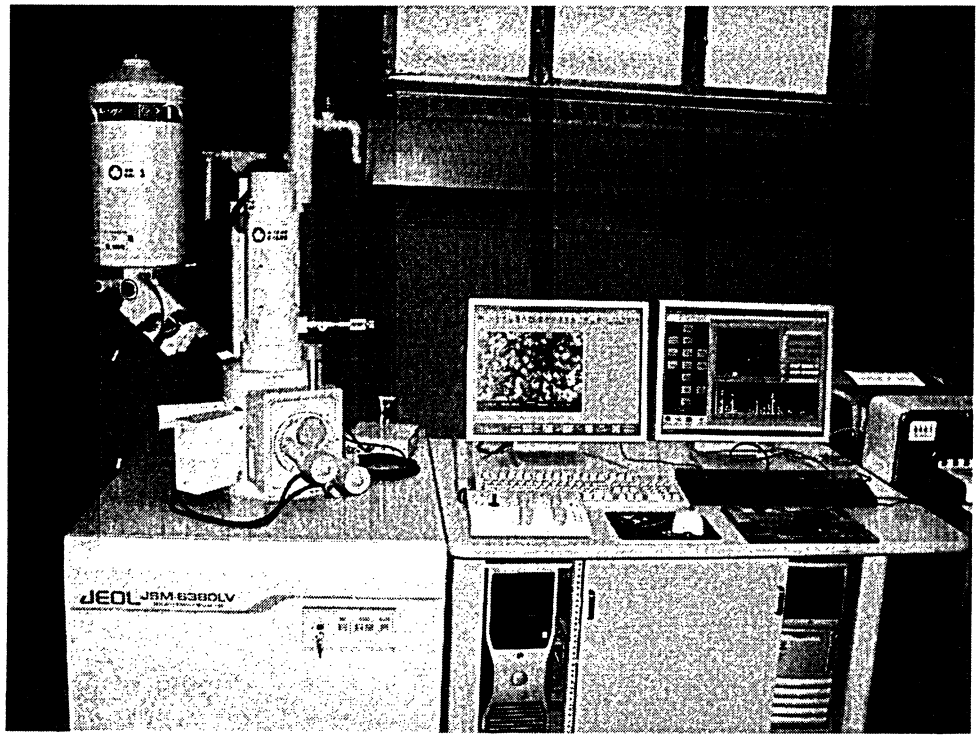

Figure 3.19 SEM with EDS (JSM-6380LV).

3.3 Electrode Wear Consideration

Fresh electrodes were used for establishing each lobe and were installed properly to avoid misalignment and had to be dressed before the start of the welding.

3.3.1 Electrode Installation

Before installing the electrodes into the holders, they were coded T (for top) and B (for bottom) with a marker. The electrodes were installed in the adapters and the cooling tubes were adjusted. An adequate electrode force (less than the target welding force) was applied temporarily to set the electrodes. Electrode alignment was checked by

visual inspection. Adjustments were made to eliminate any misalignment. Full welding pressure was applied to seat the electrodes in the adaptors.

3.3.2 Electrode Dressing

The electrode were dressed if the electrode faces were not parallel to each other and had lower face diameters than specified. A 400 grit dressing file was inserted between the electrodes. The electrodes were brought together using a low (< 20 kgF) electrode force to prevent excessive material removal. Then the file was rotated in ~180^0 and then back. The electrodes were then retracted and the file was cleaned. To achieve a smoother finish on electrodes faces, an emery paper was folded on an uncoated piece of steel sheet and inserted in-between the electrodes. The electrodes were brought together and the emery paper was rotated 180^0 one way and then the other [48]. Electrode dressings were applied only if the machined electrode face diameter was less than the specified (± 1 mm) or if the electrode face did not have a smooth finish.

3.3.3 Electrode Conditioning and Weld Stabilization

The electrode face of each electrode was stabilized before using it for determining the lobes. The stabilization of electrodes is necessary because the as-machined electrode faces did not give a good repeatability of results.

Figure 3.20 shows the variation of the weld button size and current with increasing number of welds for new electrodes [48]. It shows that the button diameter and weld current vary in a dynamic pattern at the beginning of the use of a new electrode. To

compensate for this dynamic behavior of new electrodes, a weld size stabilization procedure is necessary at the start of each lobe test. This procedure conditions the faces of the fresh electrodes. The stabilization procedure requires approximately 80 to 250 welds. After the stabilization electrode faces get conditioned and show less variation in the button size. Thus, the stabilization promotes reproducibility of the test results. The stabilization procedure consists of adjusting the welding current when needed to maintain a specified or fixed weld size. As seen in Figure 3.20, during stabilization, the current is increased until the button size reaches a critical size called the stabilization weld size (SWS). SWS can be defined as 90% of the dressed face diameter. (e.g., SWS = 5.4 mm for a 6.0 mm dressed face diameter). The SWS was rounded to ± 0.1 mm.

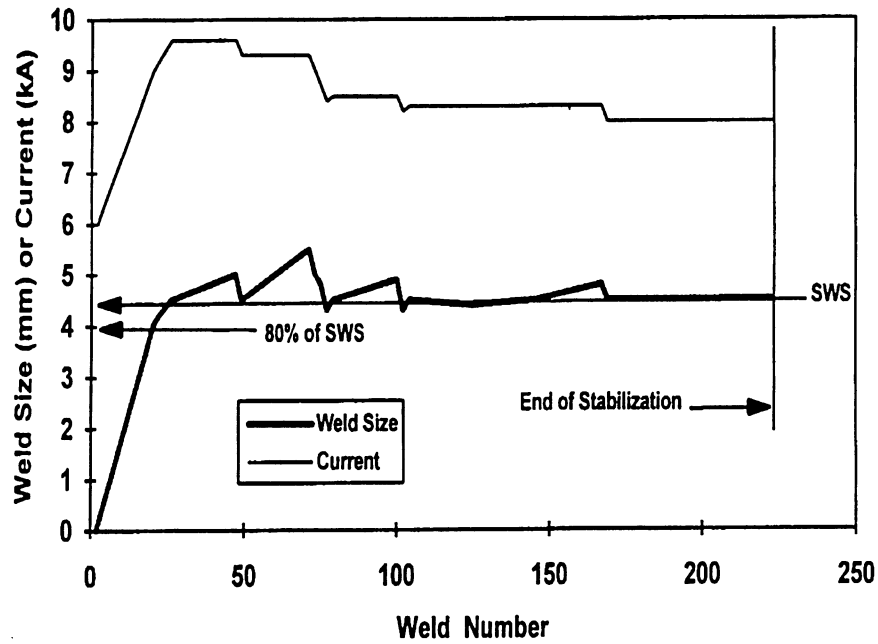

Figure 3.20 Graphical example of typical stabilization procedure. [48]

In all cases, only the test weld (2nd weld) of the peel samples was used for establishing button size and fracture mode [48].

3.3.4 Procedure for Electrode Face and Weld Stabilization

The following steps were used for the electrode stabilization [48]. During the stabilization process, the button size was determined through the peel test and calliper measurement.

1. Based on the test data previously obtained, welding parameters were set to a value that results in a no-fusion condition on the test weld of a peel sample. No fusion is the condition where there is no button formation of any size at the faying interface.

2. If a button of any size was obtained, the current setting was reduced by an interval of 1000 A.

3. If no fusion was obtained, the current setting was increased in increments of 300 A until a test weld button size of about 70% to 80% of SWS was obtained.

4. Once the weld button size was within 70% to 80% of the SWS, the current setting was increased in the increments of 100 A until the button size was within ± 0.1 mm of SWS.

5. If the weld size was within ± 0.1 mm of SWS, without changing the weld parameter settings, one row of 19 welds was made on the panel sample. All 19

welds should be welded without expulsion. If expulsion at any weld was observed, the process was stopped, the current was reduced by 300 A and steps 4 and 5 were repeated. The direction of the panel movement with respect to the machine throat was maintained as shown in Figure 3.21.

6. After welding a row of 19 welds without adjusting the current settings, two peel samples were welded and the average button size was measured.

7. If the average button size was not greater than + 0.1 mm of SWS, another row of 19 welds was welded.

8. Step No. 7 was repeated once more. If three consecutive 19 weld rows, were welded without expulsion and the button diameter was within ± 0.1 mm of SWS after each 19 weld row, the stabilization procedure was ended.

9. If the average button diameter after step 6 dropped below the SWS, the current was raised in an interval of 100 A and steps 4 to 7 were repeated.

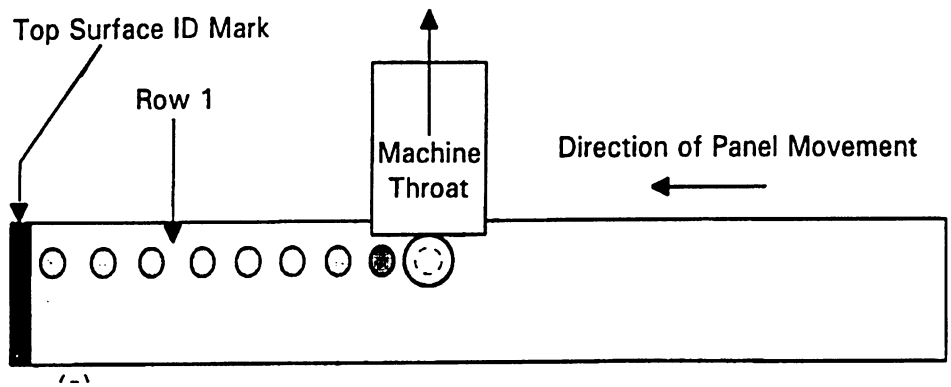

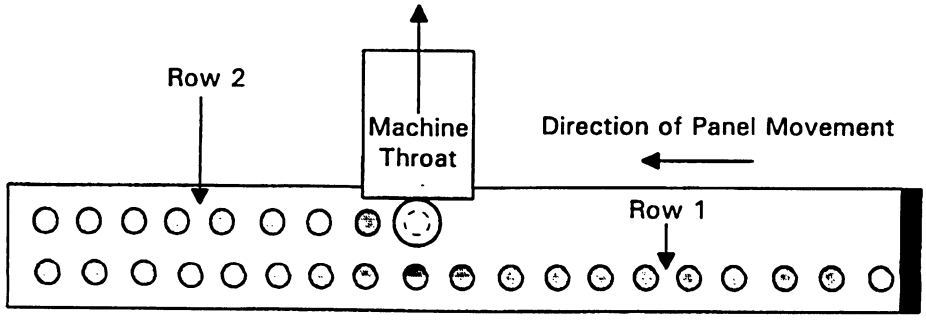

Figure 3.21 Panel sample orientations with respect to the welding machine throat. [48]

After welding three consecutive rows of 19 welds on the panel sample without expulsion at the SWS button size, it was assumed that the electrodes were stabilized. Lobes were then determined with the stabilized electrode tips.

As the welding trial continues, the electrode surface will be worn out. Al in HDG coatings accelerates electrode wear [65]. In this study, DP600 steel having a relatively high Al content in its coatings exhibits relatively short electrode lives of about 2000 welds. The electrodes gave good repeatability and no apparent changes in the process parameters were observed up to 1600 welds. Hence, the practice of changing the electrode after 1600 welds was selected for the present study to minimize or eliminate the electrode wear effect [65].

CHAPTER 4

RESULTS AND DISCUSSION

This chapter presents the results and discussion on the monitoring of welding expulsion and fracture characteristics after tensile shear and fatigue tests. The focus of the current discussion is on the weld expulsion analysis. Weld lobes for HDG DP600 were established according to Auto/Steel Partnership test standards.

4.1 Nugget Growth and Expulsion Monitoring Studies

4.1.1 Weld Lobe Results

The weld lobe diagram obtained for DP600 is shown in Figure 4.1. Two different electrode forces were tested for the lobe diagram. For 3.34 kN electrode force from A/SP standard and field practice, the lobe widths are shown in Table 4.1. Since a larger lobe width represents a bigger window for the selection of welding parameters, which represents a robust process for an acceptable button diameter, it is better to choose the current setting of 18 cycles. The reason that the lower electrode force was not chosen will be discussed later.

Table 4.1 Lobe widths for DP600 steel. [Appendix]

Weld Time (Cycles)	Lobe width (A)
18	1670
14	1270
10	1200

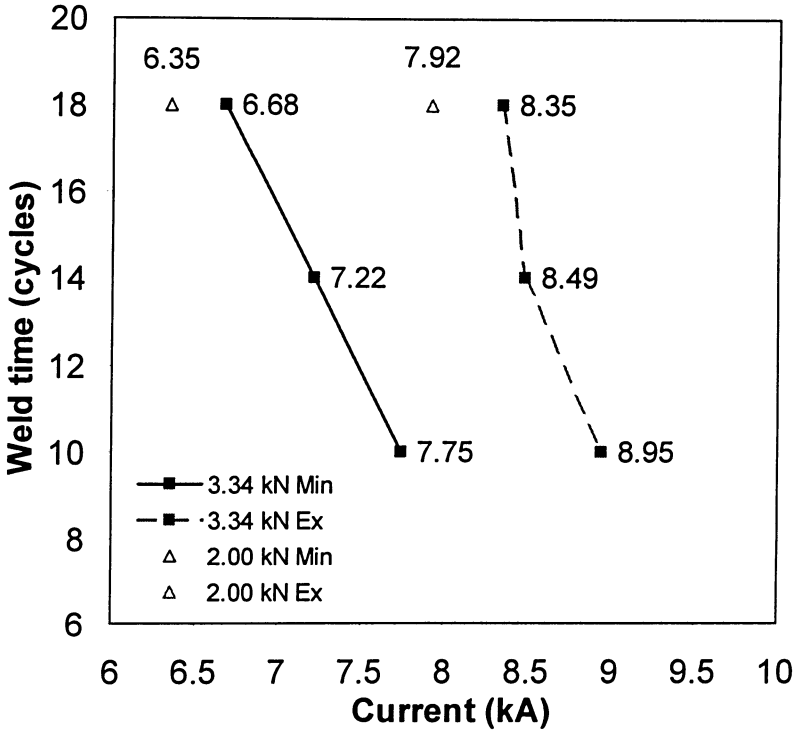

Figure 4.1 Lobe test diagram of DP600 steel.

4.1.2 Voltage and Current Feature Identification

The voltage of the transformer is controlled by the silicon controlled rectifier (SCR). The SCR starts to fire and lets the current pass when the firing command is given. The SCR will stay open until the current becomes zero. The voltage and current traces have waveforms as shown in Figure 4.2(a)&(b), similar to those observed by Li [3]. In Figure 4.2(c), there is a phase shift between the current and voltage signals because the load of the electrical part in a RSW welder is inductive. It also shows that at a time of 0.28 sec (16 to 17 cycles, which may be seen from Figures 4.7 and 4.8) there is no apparent evidence to determine if the expulsion occurs based only on the voltage and current signals since the peak values of voltage and current change all the time during the welding.

Careful observations of the dynamic features of other expulsion welds at different cycles reveal no good relationship between the voltage or current signals and the occurrence of expulsion.

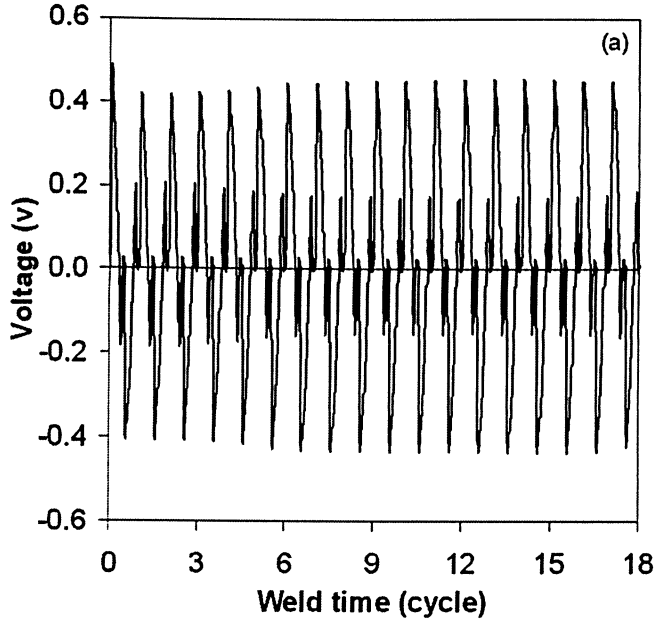
(a)
0.6
0.4
0.2
0.0
-0.2
-0.4
-0.6
Voltage (v)
0
3
6
9
12
15
18
Weld time (cycle)

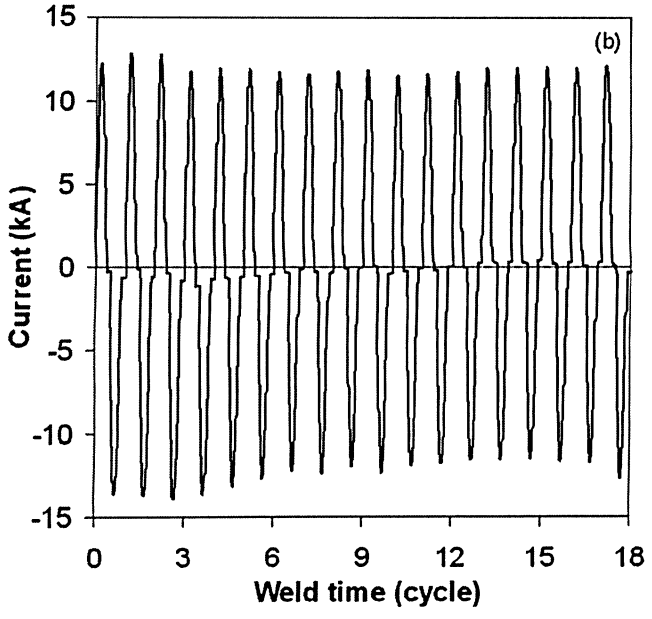
(b)
15
10
5
0
-5
-10
-15
Current (kA)
0
3
6
9
12
15
18
Weld time (cycle)

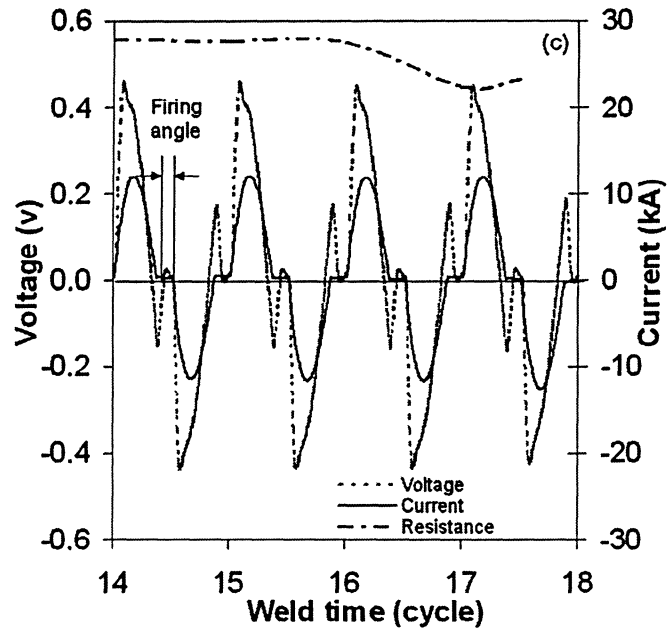

Figure 4.2 Voltage and current curve with expulsion (3.34 kN, 8.35 kA):

(a) & (b) All 18 cycles; (c) Last four cycles enlarged.

4.1.3 Dynamic Resistance Feature Identification

Measurements or calculations of dynamic resistance appear to be one of the most widely accepted procedures to control spot-weld quality [3]. Dynamic resistance is the term given to the varying electrical resistance of the weldment during a spot weld operation. To eliminate the inductive noise in the voltage signal, the resistance can be calculated accurately by using the peak current of the half cycle, where di/dt equals zero and the voltage at that moment (not the peak voltage due to the phase shift). The resistance trace at different current values is shown in Figure 4.3, which includes an

initial steep fall due to the zinc coating becoming completely molten; an almost linear increase due to the increasing bulk heating; a decrease due to the zinc removal and the increase in halo size; again a nearly linear rise of the curve due to the increasing heating of the steel substrate; then a decreasing slope of the curve due to the increase of the contact surface with the steel melting and softening; and finally a sharp drop if the expulsion occurs.

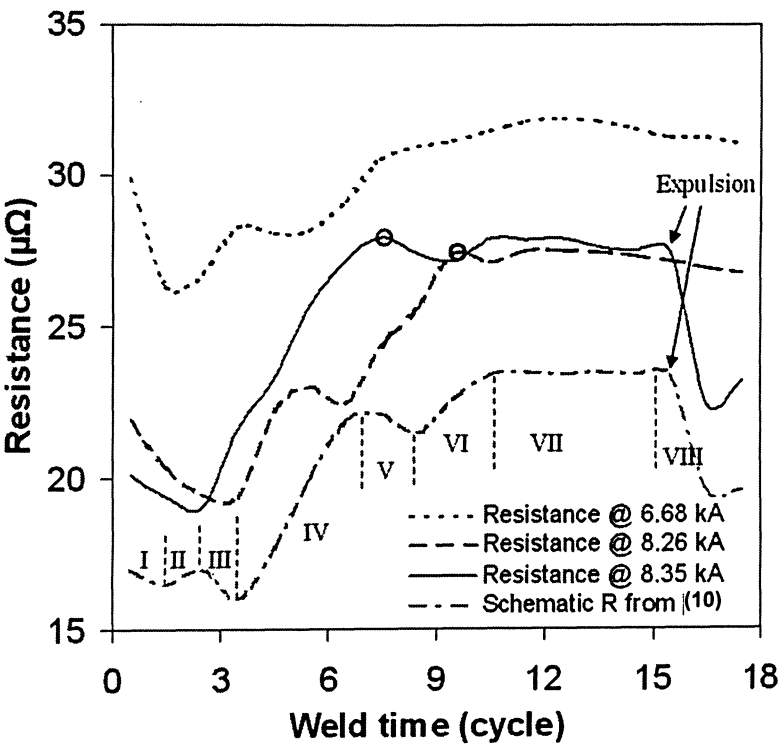

Figure 4.3 Dynamic resistance curves at different current values (3.34 kN).

Gedeon *et al.* [10, 14] identified eight regions in their galvanized steel resistance curve (shown as a schematic resistance curve in Figure 4.3). According to the nugget growth

analysis cycle by cycle [10], region II is primarily due to bulk heating of the coating at the electrode/sheet interface. The reason for the lack of region II in this study is mainly because the bulk resistance increase from the galvanized coating is very small compared to the resistance decrease from the molten interface.

The effect of varying current levels upon the resistance curve is examined for a current range from below the acceptable lobe region to that in the expulsion region with a number of welds made at the 18-cycle weld time, as shown in Figure 4.3. There is an initial spike in the first one to two cycles which rapidly decays. The peak in the dynamic resistance curve is due to the balance between the resistance increase resulting from increasing temperature and the resistance drop due to molten nugget growth and mechanical collapse [11]. Also this peak occurs earlier at higher current values. After the initial spike, the resistance increases rapidly to the peak value. The rate of resistance increase (the slope of the resistance curve) has a mean value between 30 μΩ/s and 80 μΩ/s for currents of 6.68 kA and 8.26 kA, respectively. At a higher value of the current, the slope of the resistance increases very rapidly to the peak and then drops suddenly after the peak due to the occurrence of expulsion. For the current (8.35 kA) resulting in the expulsion, the mean slope of the resistance increase is about 105 μΩ/s.

In this study, the effect of different electrode tip forces on the resistance curve is also determined. The dynamic resistance curves obtained for the electrode forces of 2.00 kN and 3.34 kN are presented in Figure 4.4. With the higher force, a general decrease in the resistance level is seen. A decreasing resistance results in a decrease in the heating rate which makes the peak of the curve shift to longer times. The current at

which the expulsion occurs for the 2.00 kN force is 7.91 kA (82% current control), while the expulsion for the 3.34 kN force occurs at 8.35 kA (84% current control). As the current increases, the heat input increases, and the molten metal quickly grows, with the result that the external electrode force cannot support the internal nugget thermal expansion force. Thus, Figure 4.5 shows that expulsion occurs at a smaller current value for a lower electrode force. Both groups with different electrode forces exhibit a smaller nugget diameter beyond expulsion. Figure 4.6 further shows nugget diameters for high and low electrode force welds for incremental welding times (from 2 to 22 cycles at 2 cycle intervals). It can be seen that a lower electrode force favours a larger nugget diameter.

Recalling Figure 4.4, the resistance curve for the 2.00 kN electrode force shows a fluctuating curve which makes it difficult to control the process. Therefore, it is preferable to operate with a higher force and current to make the RSW process stable and controllable.

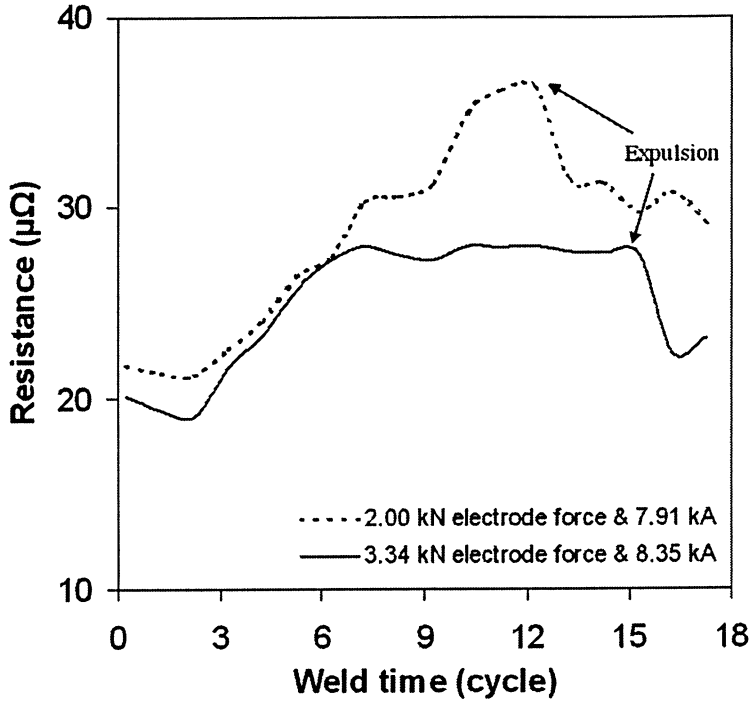

Figure 4.4 Variation of the dynamic resistance with electrode force.

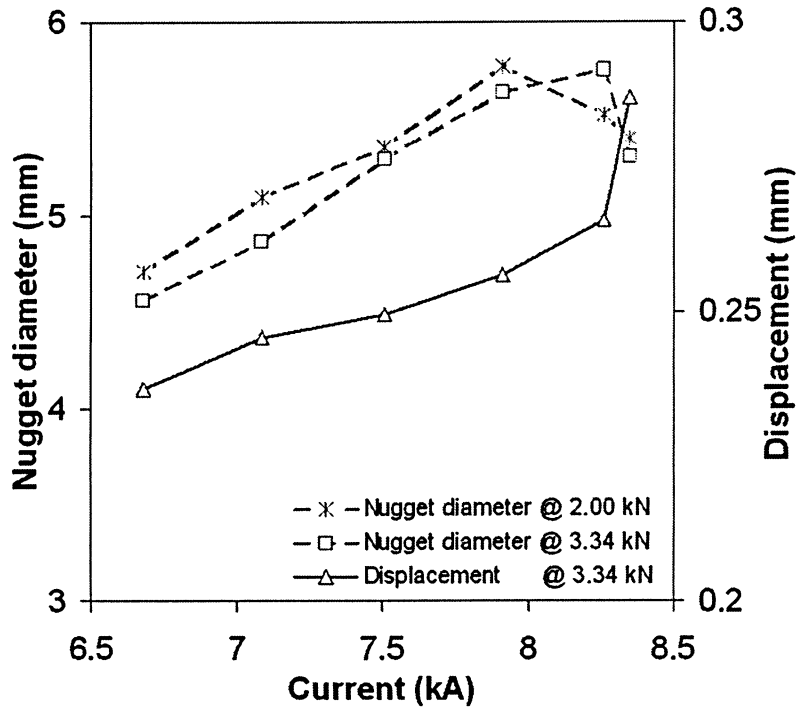

Figure 4.5 Nugget diameter and total displacement versus current.

As shown earlier in Figure 4.3, the expulsion point is marked by a sharp drop in the dynamic resistance curve. This drop is the result of mechanical collapse around the nugget reducing the effective thickness of the material and the increased effective contact area provided by the expelled metal trapped between the sheets [11]. In order to obtain more insight into the criteria for expulsion, the dynamic force and displacement are also measured and identified below.

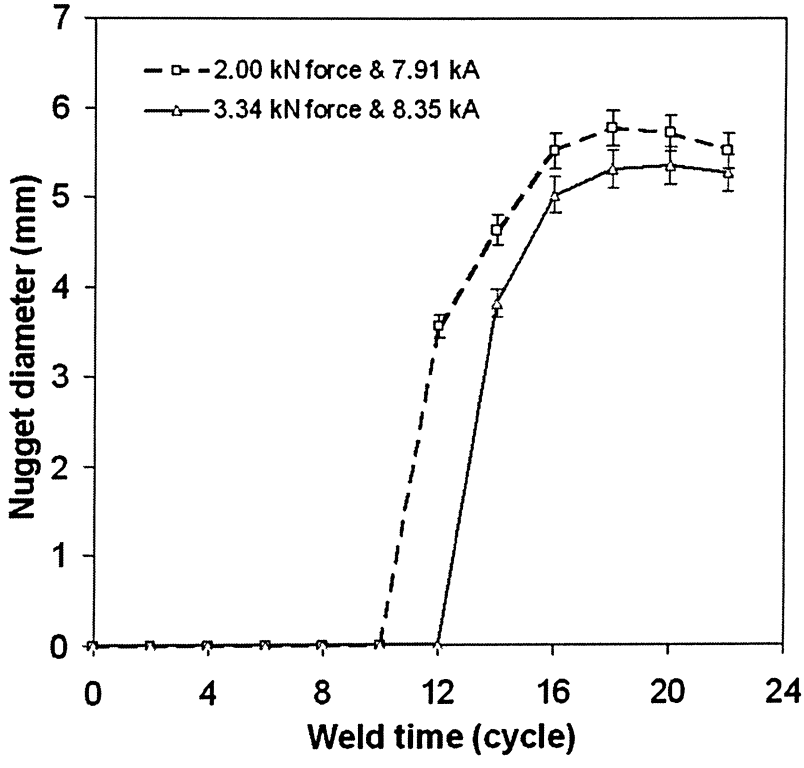

Figure 4.6 Nugget diameter versus weld time with varying electrode force.

4.1.4 Force Feature Identification

In this study, a piezoelectric load cell is used to measure the dynamic electrode force which is a better method for the force measurement [10]. The dynamic electrode force is the sum of the preset electrode force, the electromagnetic force, and the nugget expansion force due to electrode constraint. Thus, the dynamic force curves obtained with the load cell in this study are similar to the ones in references [6, 28]. As shown in Figure 4.7, the dynamic force increases at the beginning of the welding stage, and then decreases after the peak. The dynamic force curve has an oscillating feature due to the vibration of the welding machine characteristics, and the balance between the electromagnetic force and tip force. The electromagnetic force tends to force the electrodes apart and decrease the electrode force along with the nugget growth constraint force.

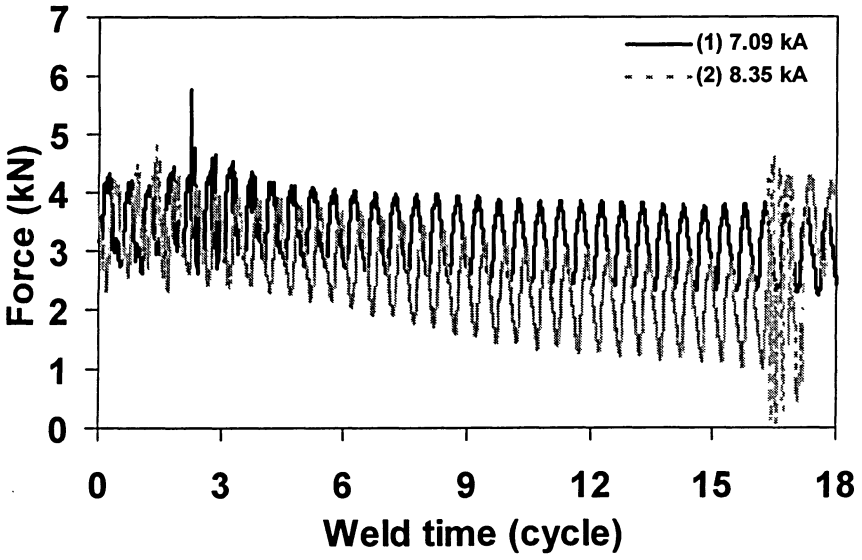

Figure 4.7 Electrode force versus weld time at different current values (3.34 kN).

Figure 4.7 shows the dynamic electrode force curves for a weld time of 18 cycles. When the welding current changes from 7.09 kA to 8.35 kA (with a nugget diameter larger than 4.54 mm), all the peel test coupons failed as pullout buttons, which indicated good welds. Weld expulsion occurs when the current reaches 8.35 kA. From A/SP specifications, the minimum weld-button size (MWS) is calculated using the formula [48],

$$MWS \geq 4\sqrt{t}, \tag{4.1}$$

where t is the average sheet thickness in mm, which is 1.24 mm for DP600 steel. The corresponding minimum required nugget diameter is 4.47 mm.

Therefore, welding currents of 6.68 kA to 8.26 kA with 18-cycle welding time and 3.34 kN electrode force are evidently required to produce a good quality nugget without expulsion.

At each current setting, from the start to the end of the welding current, the dynamic force increases in the first one to two cycles and then gradually declines. The initial rate of force increase over the first two cycles has a mean rate of 16.21 kN/s to 24.33 kN/s, and then the mean decrease rate of the force after the peak is from 1.94 kN/s to 5.22 kN/s for the current values from 6.68 kA to 8.26 kA, respectively. For the current (8.35 kA) resulting in the expulsion, the mean slope of the force increase is 25.21 kN/s and that of the latter force decrease is 6.23 kN/s.

4.1.5 Displacement Feature Identification

The electrode displacement is the result of weldment thermal expansion. It is measured as the displacement from the start of the current application when the electrodes squeeze the two sheet specimens together to the end of current application. When the electrode is forced to move upward because of the nugget thermal expansion, the electrode displacement will increase as shown in Figure 4.8. Sudden downward movement of the top electrode is referred to as a sudden drop in the displacement signature. Figure 4.8 (a-1 and a-2) shows that the displacement curve is approximately a linear function of the weld time. Similar curves have been reported in references [10, 14], in which the curve was separated into 6 distinct regions. The two opposing displacement mechanisms, thermal expansion and removal of material (zinc coating), contribute to the electrode displacement. However, in this study, the thermal expansion from the zinc coating and the steel substrate dominated the displacement trace. The first stage in this curve is a decrease of displacement of about 6 μm at the beginning of the weld stage (within about 0.2 cycle) due to the flattening of the asperities and the easily softened zinc surface as shown in Figure 4.8(b). Then, the thermal expansion of the zinc coating and the steel substrate has a dominant influence on the displacement curve. At 0.1 second (5 to 6 cycles), the zinc coating melts and is pushed away from the centre to form a halo. During this period, the displacement curves exhibit a slowly increasing slope. Next, the thermal expansion again results in the further increase of the displacement curve and reaches a maximum value before the current is shut off. After this, the displacement trace decreases as the holding time begins. If the welding heat input is too high (the current is too high or the welding time is too long), expulsion will

occur before the current is terminated. The sudden drop in the displacement trace thus indicates the expulsion as the material between the electrodes is lost [14].

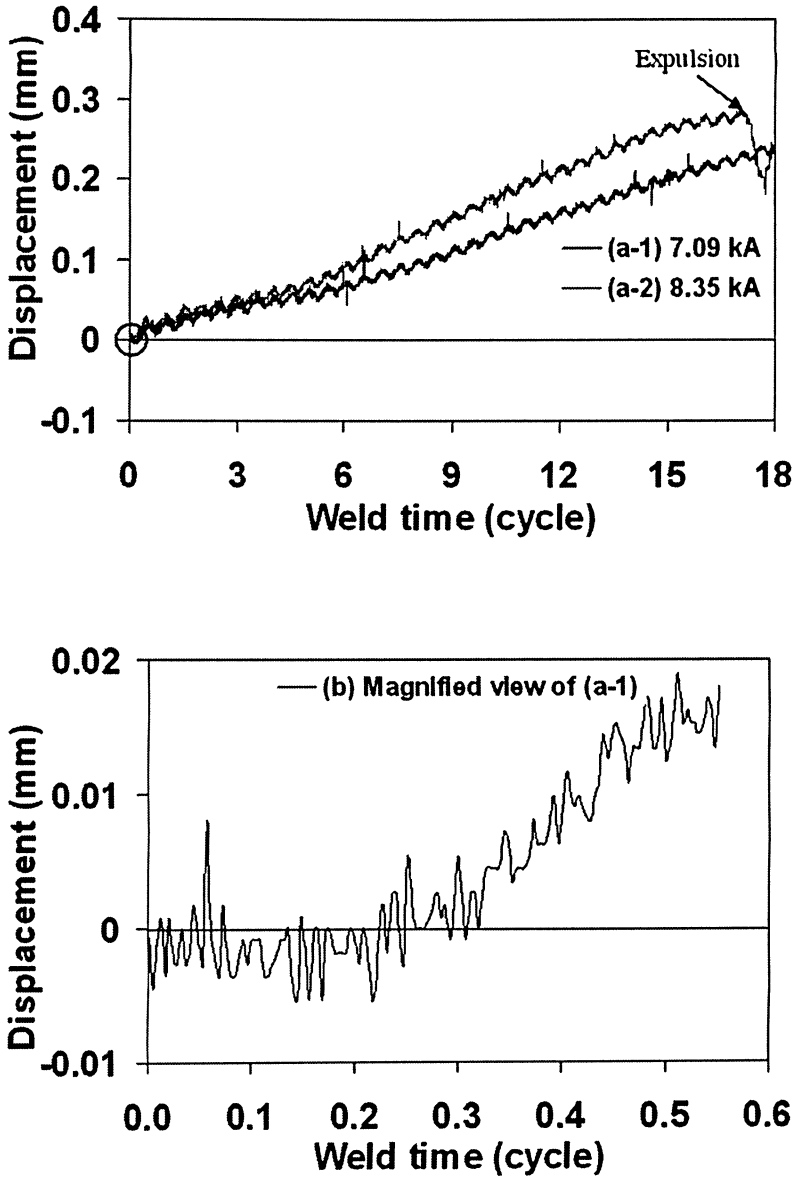

Figure 4.8 Electrode displacement versus weld time at different current values (3.34 kN)

Going back to Figure 4.5, the maximum electrode displacement (the total change of electrode displacement) and the nugget diameter (both averaged over a number of experiments) are plotted against the range of currents from current loading to current unloading. It is seen that both the electrode displacement and the nugget diameter increase almost linearly with the current from 6.68 kA to 8.26 kA. The electrode displacement rapidly increases with increasing current from 8.26 kA to 8.35 kA due to the increasing heat input. Finally, expulsion occurs and the electrode suddenly moves downward (referred to as a sudden drop of the electrode displacement value) as shown in Figure 4.8. The average rate of increase of the displacement over the current range from 6.68 kA to 8.35 kA is about 0.79 to 1.06 mm/s.

4.1.6 Process Control Strategies

As described above, typical voltage, current, dynamic resistance, force and displacement signals under different welding conditions can be measured. A better understanding of the process has been obtained by analyzing these parameters. Based on the present experiments, possible strategies for process control in the RSW of DP steels could be proposed based on the dynamic characteristics of resistance, electrode force and displacement [44]. There are three possible strategies for process control, namely:

I. Monitor the total (or absolute) electrode displacement or the slope of the electrode displacement.

II. Monitor the value of the rate of change of the dynamic resistance between the bottom and the peak of the resistance curve below a specific value during a specific period.

III. Monitor the value of the rate of increase of the electrode force to its peak and the rate of decrease after the peak.

The procedures for implementing the above strategies include the following three steps:

I. Conduct a lobe test to find the proper welding time and current to achieve a satisfactory nugget of good quality and strength without expulsion.

II. Conduct experiments using the DAS to determine the total displacement, and the rate of change of the resistance, force, and displacement by using the experimentally predetermined welding parameters.

III. Input experimental parameters into the process control system to keep the current constant and monitor the parameters simultaneously until the total change in electrode displacement reaches a desired value (described in section 'Displacement feature identification'), or the rate of change of the resistance, force, and displacement reach a certain peak value or starts to drop. The detailed discussion is given below.

In strategy I, since the displacement curve shows an approximate linear increase with weld cycles (Figure 4.8), the total change of displacement or the slope of the displacement curve can be used for control. The relationship between the total change

of displacement and the nugget diameter, presented as a function of the current shown in Figure 4.5, reveals that the total change of displacement correlates well with the nugget diameter for the welds prior to the expulsion. As discussed above, a desired total change of displacement of about 0.27 mm with a weld time of 18 cycles or the slope of the displacement at about 0.90 mm/s could be used to ensure nugget diameters of 5.75 mm based on the current of 8.26 kA.

For strategy II, the average rate of the increasing dynamic resistance between the bottom and the highest peak (solid line circle in Figure 4.3) of the resistance curve during a specific period can be used for control. In this case, the period used to control the rate of the dynamic resistance is from regions IV, V, and VI, in which 6 cycles were found to be essential for good welds. This period will be better for monitoring since the current, electrode force and other process parameters are kept as constant as possible. After the bottom point is monitored and determined, the increasing rate of the next six cycles needs to be controlled below a specified value as determined from experiments. For instance, in this work, a targeted rate of increase of the resistance would be about 80 μΩ/s based on the results of the welding current of 8.26 kA. Moreover, since the practice of changing the electrode at 1600 welds was selected for the present study to minimize or eliminate electrode wear, the threshold values of the increasing rate of dynamic resistance are not sensitive to the wear of the electrode face between electrode changes.

For strategy III, Figure 4.7 shows that the rate of increase of the electrode force is correlated to the nugget formation and growth as shown in Figure 4.8. For example, in

this study, the rate of increase of the force is approximately 24.33 kN/s in the initial two cycles. Then the decreasing rate of the force is approximately 5.22 kN/s in the remaining cycles for a current of 8.26 kA.

The above three strategies for the process control in the RSW of DP steels are proposed on the basis of the characteristics of the dynamic resistance, the electrode displacement and the electrode force. However, strategy I has the drawback that other variables such as the sheet thickness, welding current, and time can also affect the change of displacement [3,44]. The force sensor and its signal-conditioning module are more expensive than the sensors and module for dynamic resistance used in strategy II. The force signal used in strategy III shows that an early force peak with a certain slope and its subsequent force drop with a specific decreasing rate are essential to form a good-sized weld. Monitoring the force signals can achieve a better weld quality. On the other hand, compared to the force signal, the dynamic resistance signal can be obtained more easily and inexpensively. In fact, monitoring the dynamic resistance indirectly monitors the heat input to ensure that the nugget grows properly and evenly without expulsion. However, it should be noted that, whenever there is a change in substrate material or coating characteristics, it is first necessary to establish the lower and upper limits of the range of dynamic resistance and to identify the specific weld periods from the pre-test procedures.

4.2 Mechanical Properties and Fractography

For RSW of HDG AHSS steels, it is very important to investigate the expulsion used to select the process parameters. Expulsion occurs both at the interface between the two sheets and at the electrode-sheet interfaces. Because of the water-cooling within the electrodes, the overwhelming majority of expulsion normally occurs at the interface between the two sheets. From the first part of this study, this expulsion can be observed from the data acquisition system (DAS) [58]. Figure 4.1 describes the results from the lobe test showing the effects of the welding current and welding time on the expulsion at two different electrode forces. Based on the considerations of the larger lobe width at 18 cycles, as well as fewer voids in the fusion zone at a higher electrode force [53], the welding parameters of 18 cycles, 8.1~8.3 kA, and 3.34 kN could be selected for practical field applications to prevent the expulsion which will be explained later.

4.2.1 Microhardness Profile

Figure 4.9 shows a typical micro-hardness profile of the DP600 which exhibited a significant hardness increase from the base metal to the weld. Due to the higher alloy content and high cooling rate, the weld nugget hardness is more than twice of the base metal at approximately 420 HVN. There is no softening in the heat-affected zone (HAZ) observed.

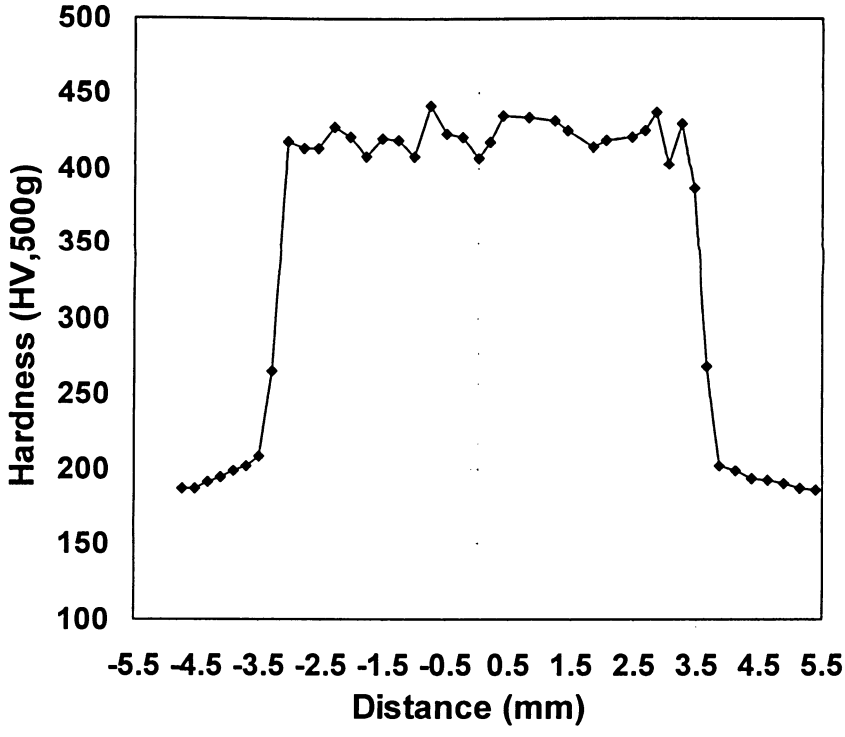

Figure 4.9 Typical microhardness profile for DP600.

4.2.2 Weld Strength – Tensile Properties

A static weld strength test is obtained from the tensile shear test to quantify the static load-carrying capabilities. Figure 4.10 shows the peak fracture force for the spot welds with different current values while other parameters are kept constant. Three of the 17 samples exhibited good pull buttons as indicated by the solid square. Another two samples showed interfacial fracture (IF) with pull button, as indicated by the dotted square. The remaining 12 samples all showed interfacial fracture. The peak fracture force was seen to reach the maximum in the range of current from 8.1 kA to 8.3 kA. In

this current range, the failure mode is also pull button without any interfacial fracture appearance. Beyond this current range, one out of five samples showed pull button and another one interfacial fracture with the pull button. However, the sheets were indented by the electrodes due to overheating beyond the current corresponding to the expulsion. The indentation is related to surface cracks, as shown in Figure 3.18(a), which possibly influences the fracture of welds during testing [50,66,67]. The maximum tensile shear load is 18 kN, and the weld strength was estimated using an empirical formula for the relation between the strength and the hardness [55,77]. The ratio of estimated weld tensile strength to the ultimate tensile strength of base metal is 2.1, as shown in Table 4.2.

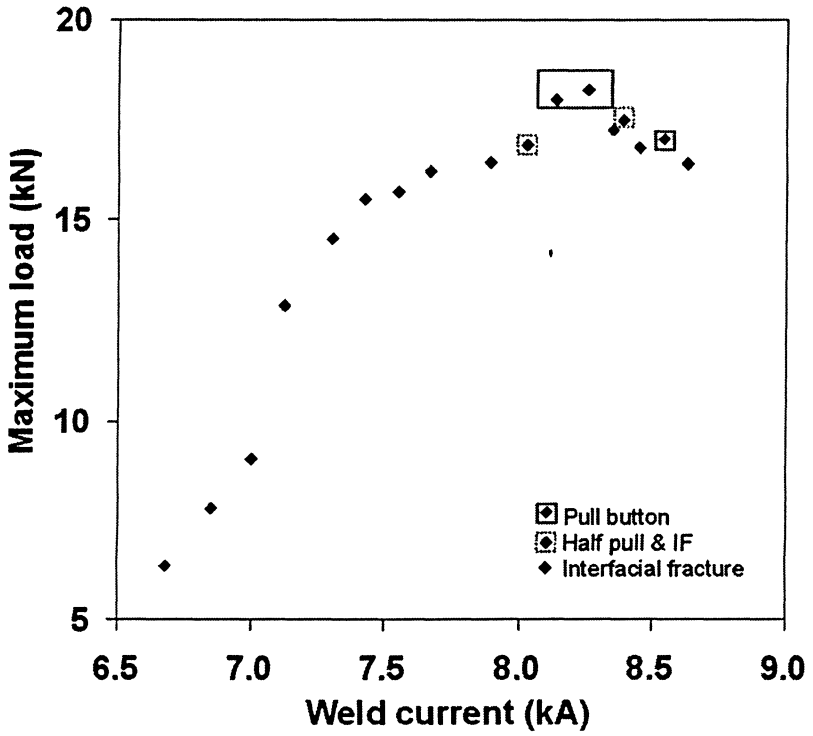

Figure 4.10 Peak fracture force versus the weld current during tensile shear tests.

Table 4.2 Maximum tensile shear force in the tensile test and the ratio of the weld shear strength to the base strength.

Maximum tensile shear force (kN)	Weld hardness (HVN)	Est. weld Strength (MPa)	Base Metal Strength (MPa)	Ratio weld/base
18	420	1357	636	2.1

Note: The estimated weld yield strength was converted from the hardness based on the relationship [77], $\sigma_{0.2} = 3.27HB^{n}$, where $\sigma_{0.2}$ is the 0.2 pct offset yield strength in mega Pascals, H is the Diamond pyramid hardness number, n is the strainhardening exponent, and B is a constant which is equal to 0.1 for steel.

4.2.3 Fatigue Strength

Tensile-shear fatigue life curves for three groups of spot welded samples with different current values are shown in Figure 4.11. Each point represents the result from the test of a single sample. The applied load decreased quickly in the range of 10^3 to 10^6 cycles. Four distinctive failure modes identified from these tests could be categorized as three regions [51], and typical photographs of fracture welds are presented in Figure 4.12. To correlate with the regions of the fatigue curves, the typical features of these failure modes were identified from visual analysis of failed samples based on the fracture characteristics. Mode I and II (Figure 4.12(a)&(b)) represents the very high-load region I (Figure 4.11), where one sample showed interfacial fracture and all other samples exhibited plastic deformation. Mode III (Figure 4.12(c)) corresponds to the steep transition region II (Figure 4.11), in which the fatigue crack initiates and propagates just

within the HAZ (close to the nugget boundary) and along around 10% to 50% of the circumference of the nugget, then into the base metal. Mode IV (Figure 4.12(d)) represents the region III (Figure 4.11) close to the fatigue limits, where the fatigue cracks initiate in the HAZ (in the vicinity of the nugget boundary) and propagate along a straight line in base metal and normal to the loading direction. Typical fatigue initiation, striation, and fast propagation regions are shown in Figure 4.13. The average diameters of three groups of fatigue test samples were determined using the optical microscopy as 4.53 mm with 6.83 kA setting, 5.54 mm with 8.14 kA, and 5.85 mm with 8.54 kA, respectively.

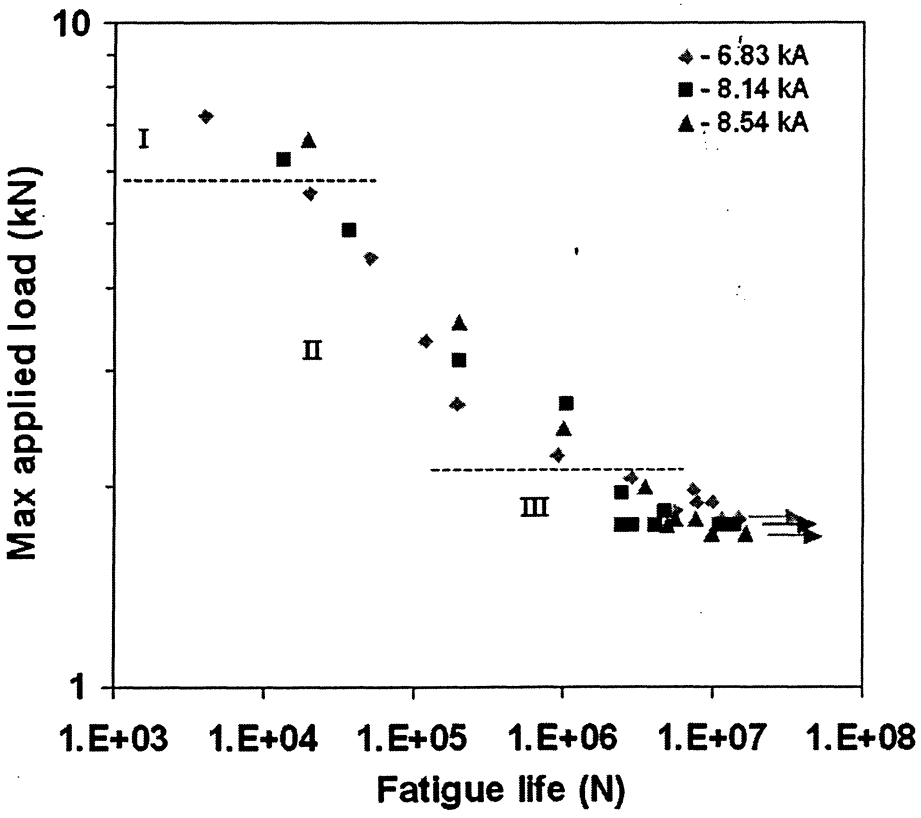

Figure 4.11 S-N curves obtained for three groups of spot welded samples tested at 50 Hz, R=0.1 and room temperature.

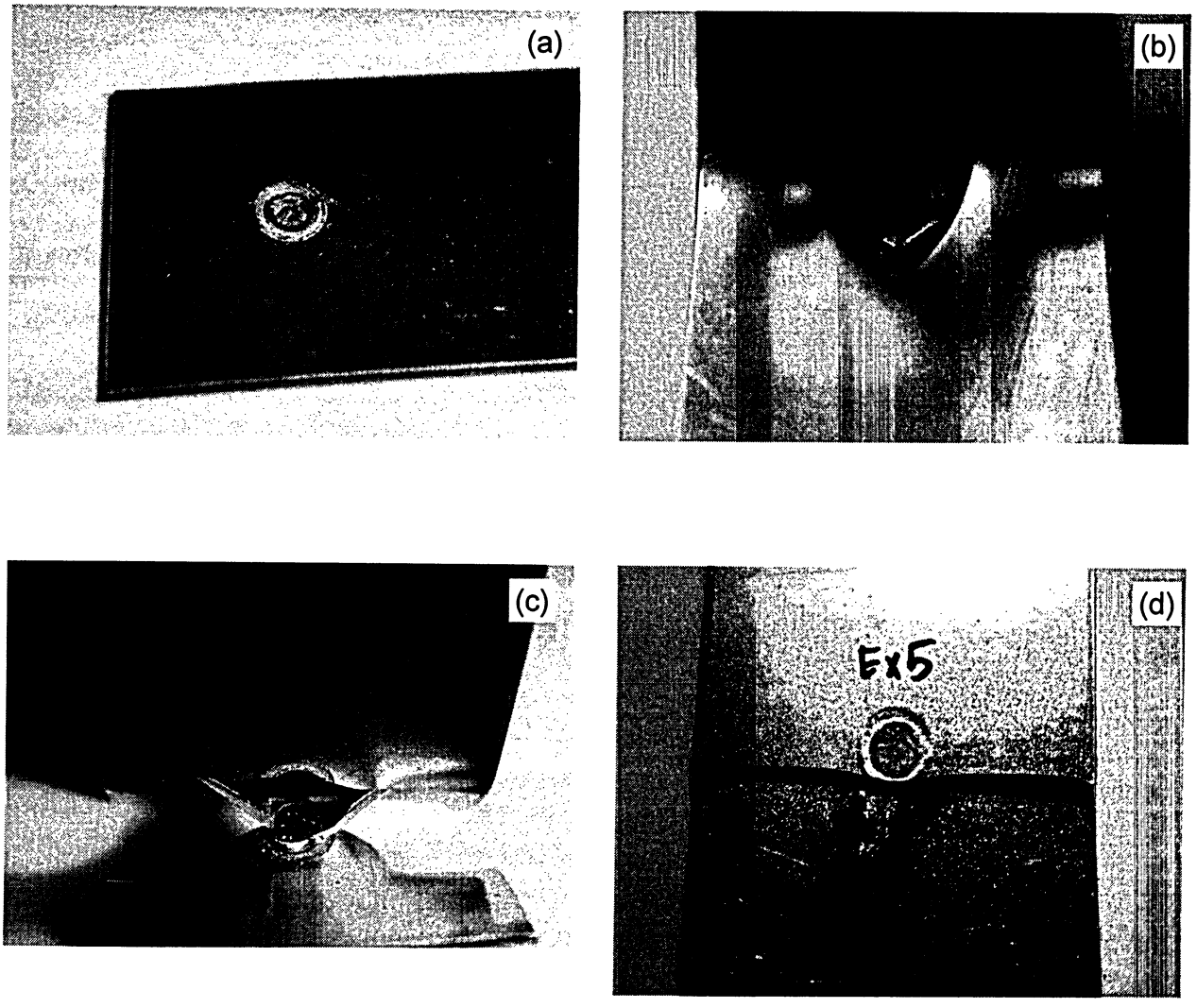

Figure 4.12 Four typical failure modes. (a) Interfacial fracture, Mode I; (b) Plastic deformation, Mode II; (c) Propagation in the circumference, Mode III; (d) Propagation in straight line, Mode IV.

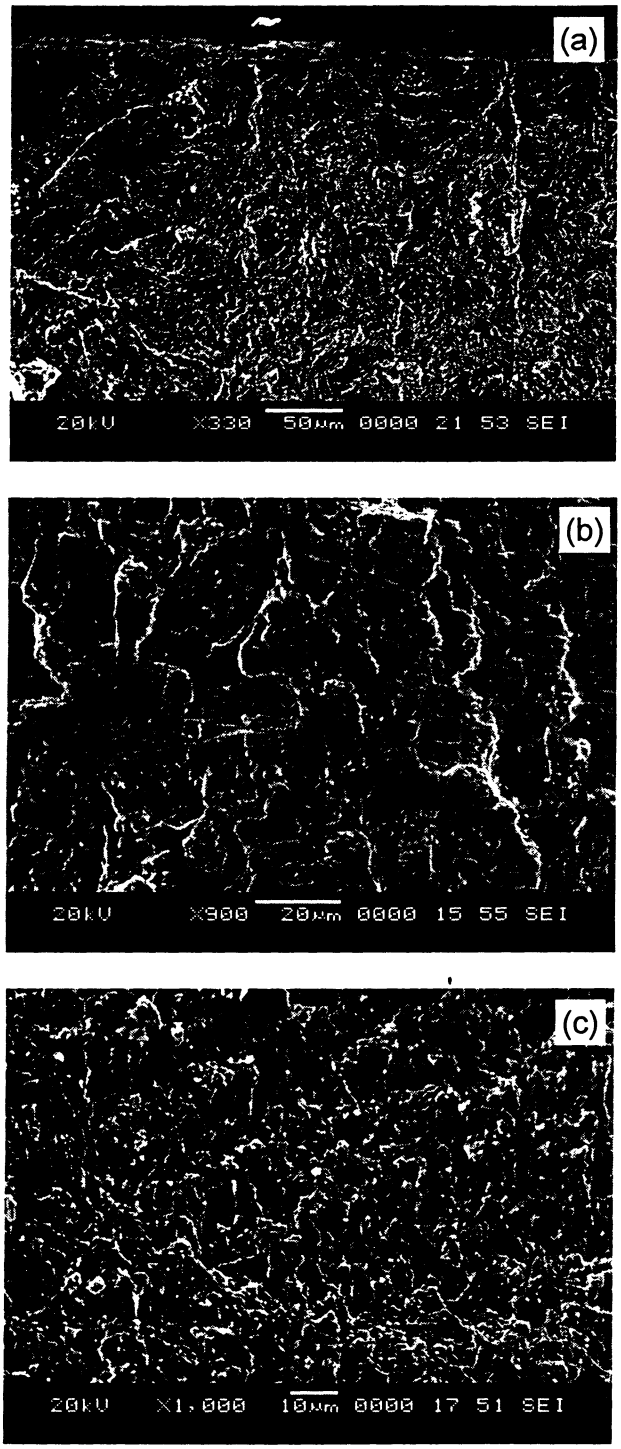

Figure 4.13 Typical characteristics on the fracture surface after fatigue test. (a) Crack initiation area; (b) Crack propagation area - striation coupled with secondary cracks; (c) Crack fast propagation region for the sample welded with 8.14 kA and tested at 2.66 kN.

4.2.4 Microstructural Variations and Imperfections

There are two phases of body-centered-cubic (bcc) α-ferrite and body-centered-tetragonal (bct) martensite in the base metal for the typical DP steels [2, 53]. Using the optical image analysis system, the variations in the microstructure of spot welds were shown in Figure 4.14. The low-magnification optical micrographs in Figure 4.14 present a series of optical micrographs from left of the weld to its centre that illustrate the variation in microstructure across the base metal, HAZ, and fusion zone observed in all welds. The figures show an increasing dark-etched portion where the dark phase indicates martensite, leading to a much higher hardness value in the weld nugget as shown in Figure 4.9.

For a detailed observation, SEM was used to examine the variations as shown in Figure 4.15. Figure 4.15(a) shows that the microstructure in base metal consists of evenly distributed martensite within the ferrite phase, and the layers of the ferrite can be seen. In the HAZ, martensite becomes more and larger than in the base metal as shown in Figure 4.15(b). In Figure 4.15(d) and (e), the fusion zone is nearly full of martensite. The transition region between the fusion zone and HAZ was shown in Figure 4.15(c) and in Figure 4.16 under larger magnifications. The micro-constituents with martensite and ferrite in the HAZ were finer than those of either the base metal or the fusion zone. This is explained by the fact that austenitizing was incomplete in the HAZ and, even when austenite grains formed, grain growth was restricted by the martensite and thermal cycles [53,68,69]. While the grains are fine, in the HAZ, the resulting high density of grain boundaries constitute obstacles against the formation of large lath martensite.

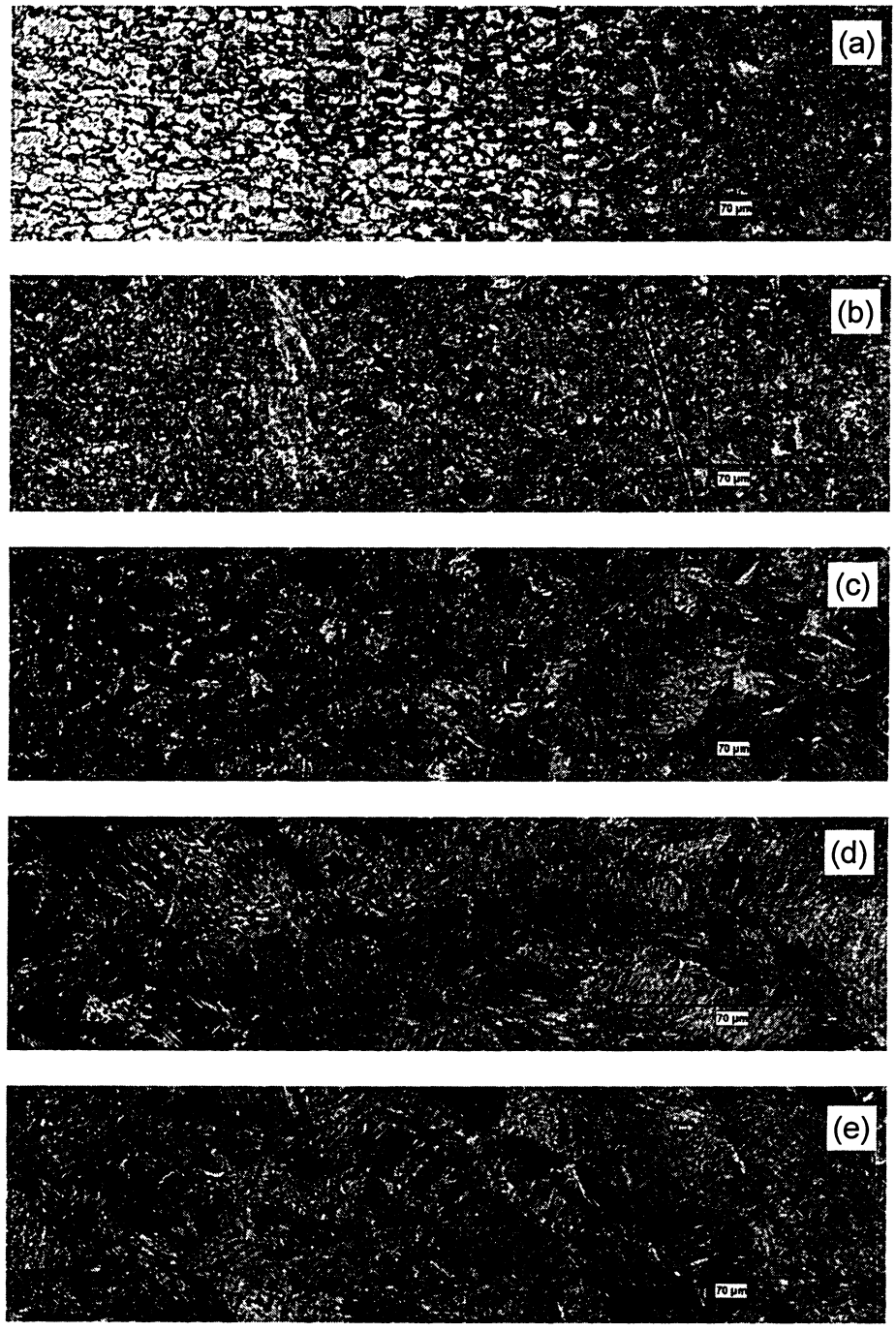

Figure 4.14 Microstructural changes from the base metal to the centre of the nugget with optical microscopy observation. (a) Base metal to HAZ; (b) HAZ; (c) HAZ to fusion zone; (d and e) fusion zone. White phase – ferrite; Black phase – martensite.

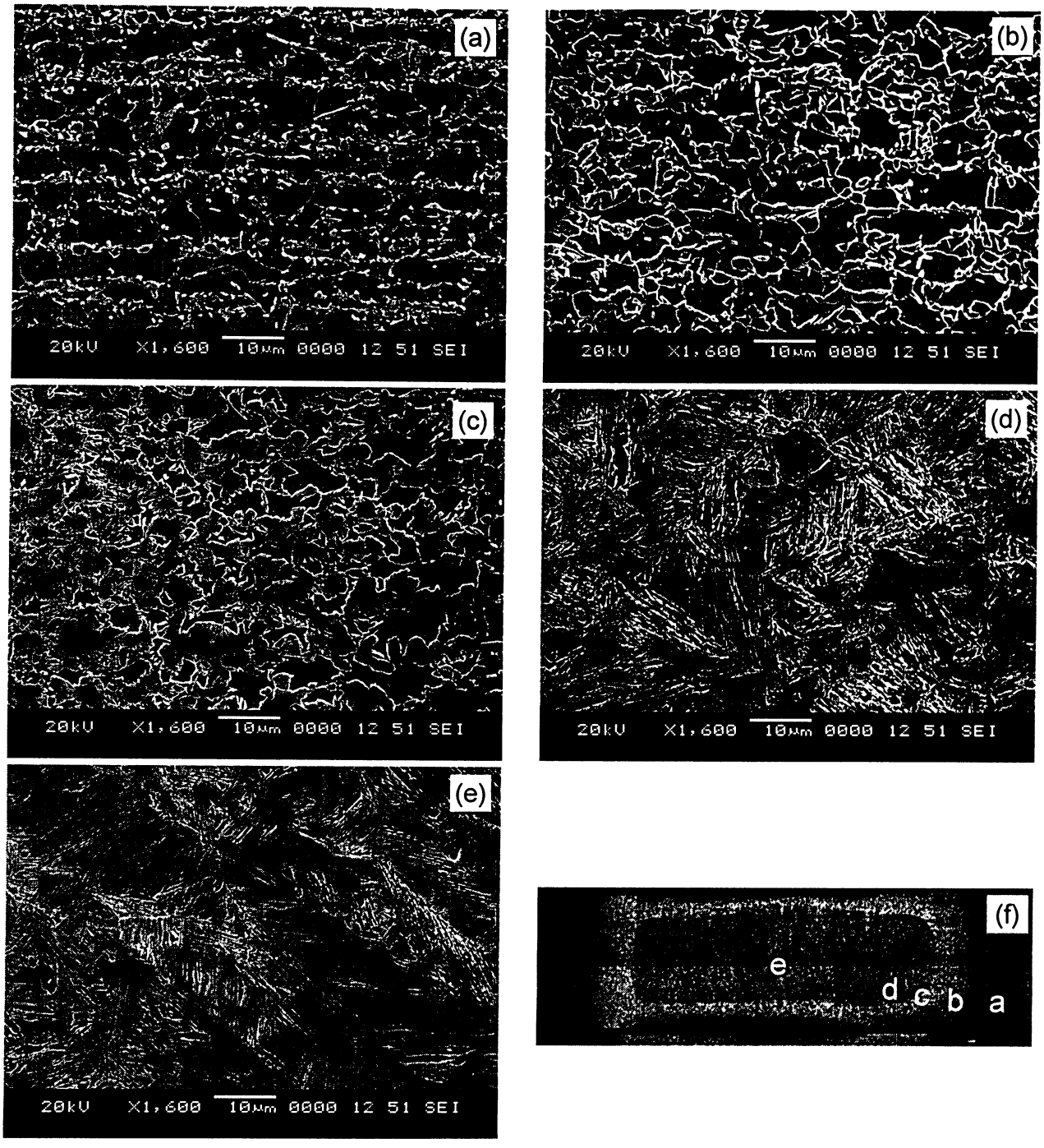

Figure 4.15 Microstructure changes from the base metal to the centre of the nugget with SEM observation. (a) Base metal; (b) Centre of HAZ; (c) Transition zone between fusion zone and HAZ; (d) Fusion Zone close to HAZ; (e) Fusion Zone in the centre; (f) overall view of the etched sample where the locations of micrographys (a), (b), (c), (d), (e) are indicated by a, b, c, d, e. White phase – martensite; black phase – ferrite.

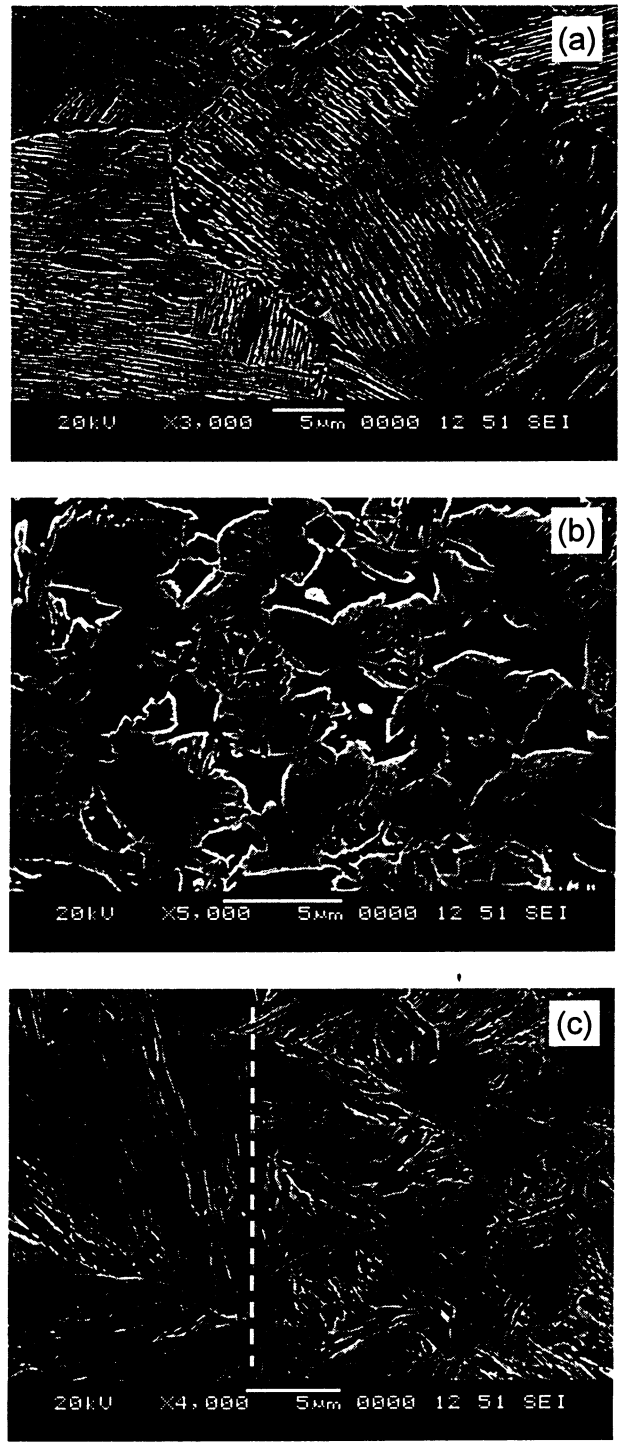

Figure 4.16 The magnified microstructure of fusion zone and HAZ mostly with lath martensite. (a) Fusion zone; (b) HAZ; (c) Transition area between the fusion zone and HAZ.

Thus, the hardness of HAZ is higher than that of the base metal, but lower than that of the fusion zone in the nugget. To understand the variations of the microstructure in spot welds, the welding process needs to be investigated (e.g., welding heat input, cooling rate and phase transformations).

For RSW, the welding cooling rate is at a very high level. Spot welds in sheets of thickness up to 2.0 mm typically solidify in less than 3 to 4 cycles [70]. The cooling rates range from roughly 2000°C/sec at a 2.0 mm gauge to over 10^5°C/sec for gauges less than 0.5 mm. In the current case of 1.25 mm thickness, the cooling rate should be about 6000°C/sec based on the figure [70]. These cooling rates are much faster than those needed to form martensite (which are around 40 to 120°C/sec) in the weld and HAZ in DP steels [69]. There is not enough time for carbon diffusion. Therefore, lath martensite is believed to form and contain very thin regions of retained austenite between laths, or pockets of laths, possibly as well as some lower bainite, as shown in Figure 4.16(c) [71]. Obviously, the process with the above estimated cooling rates will lead to a significant amount of martensite in the fusion zone and be prone to experience brittle fracture [68]. Moreover, besides the high carbon contents, high Mn contents in DP600 results in a higher hardability. To explain why there are different failure modes (some of interfacial while others partial pull button) beyond the current of expulsion, the variation in both steel chemistry and cooling rates for RSW process should always be considered. The possibility of martensite formation is more dependent on the specific chemistry used to achieve the strength levels [69].

Going back to Figure 3.18(a), voids were found to be larger in all samples in the expulsion condition, and very small, or even absent in those samples below the expulsion. Also the welds made with a lower electrode force showed a higher amount of micro-voids than those made with a higher electrode force. In the case of lower electrode force, the weld nugget may not be pressed enough to solidify before the electrodes are removed from the weld area, which can cause the micro-voids. The hold time is also an important factor which can help reduce the micro-voids for a relatively longer time [54]. From Figure 3.18(a), surface cracks were present both under and adjacent to the electrode surface contact area. Zinc coating effects and welding parameters (electrode force, weld time, and current) are more susceptible to surface cracks in the electrode indentation [50,72].

Solidification cracks in the fusion zone were also observed from different sets of samples. A typical example is shown in Figure 4.17, including both the back-scattered electron image (BEI) and secondary-electron image (SEI). Some tiny micro-cracks were observed with approximately 20 to 50μm long. These cracks are shrinkage or solidification cracks since the cooling rate of welding is considerably unevenly and steeply distributed [53,73].

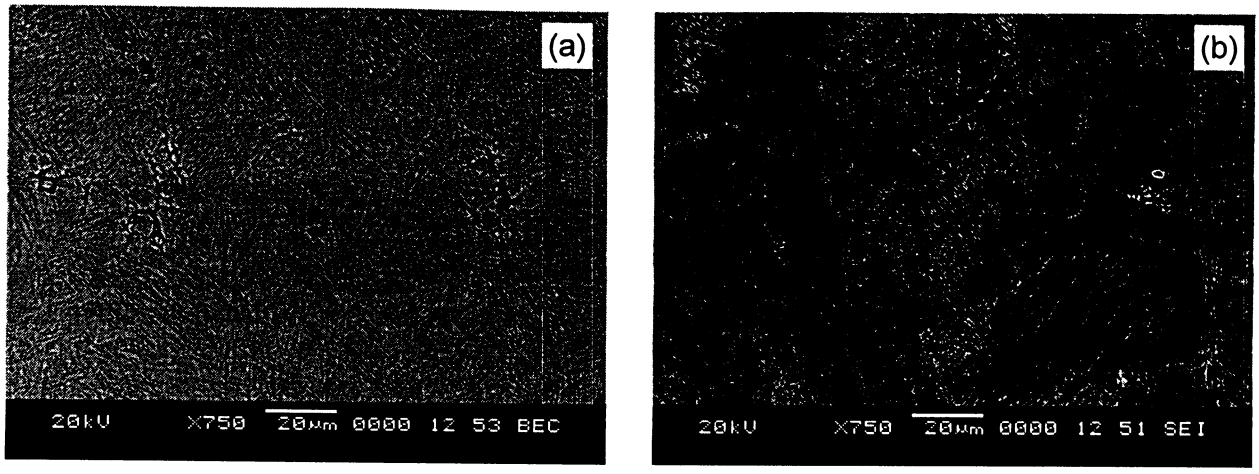

Figure 4.17 Micro-cracks in the fusion zone with the expulsion. (a) Back scattered electron image; (b) Secondary electron image.

4.2.5 Fatigue Crack Initiation Analysis

Some studies showed that crack initiation occupies a significant part of the fatigue life [74,75]. Other studies showed that the initiation occurs immediately with the majority of fatigue life spent in the crack propagation and fast failure [57]. In this study, focus is placed on the crack initiation location and the reasons for it. The opening between two sheets in the nugget-surrounding area is seen as an initial crack, as shown in Figure 4.18(a). This opening results in a larger local stress concentration during the testing. The boundary of the nugget was also weakly bonded and relatively brittle which likely resulted from molten zinc coating, as shown in Figure 4.18(b). With the help of SEM, it was observed that cracks initiated at the boundary of the nugget at the interface between two sheets close to the clamping grips which will be explained later. Then the cracks penetrated the thickness and propagated to the outside surface. Also, the dotted

square in Figure 4.19(a) and (b) showed typical ridges around the fatigue crack initiation location observed with SEM.

Crack initiation locations from pre-existing defects were also checked. Figure 4.19 illustrates some examples in which cracks initiated at the defects. This is extremely important since these defects will ultimately lead to the failure of the material. Cracks can be initiated at different defects, the three that will be discussed here are corrosion products, inclusions, and zinc coating effects from the observations of the fracture surfaces of welds. These defects result in an increase in the triaxiality of the local stress state to easily cause the crack initiation and then further accelerate the crack growth rate.

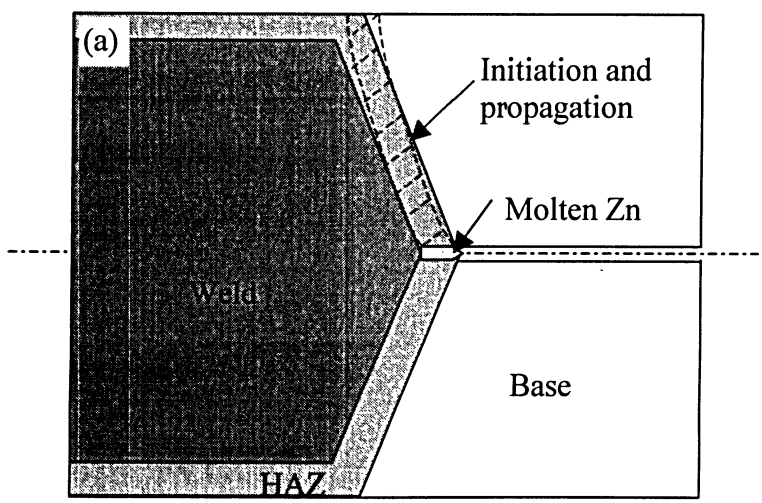

Figure 4.18 Schematic and optical image of fatigue crack propagation. (a) Schematic; (b) Optical image of the cross section near the opening of the weld.

From the fracture surface in Figure 4.19(a), there are some corrosion areas visually shown as some rust due to the expulsion. Carbide and oxide are the typical features from the EDS analysis, as shown in Table 4.3. Figure 4.19(b) and (c) showed some inclusions (e.g., Zn, Al, or Ca oxide) in the weld which likely resulted from the expulsion. By observing the crack propagation directions in Figure 4.19, it is concluded that the cracks originated from the existing inclusions. Figure 4.19(d) revealed zinc without being fully expelled from the nugget in the first four to five cycles if the current was not high enough (e.g., at the minimum current of the lobe) [58].

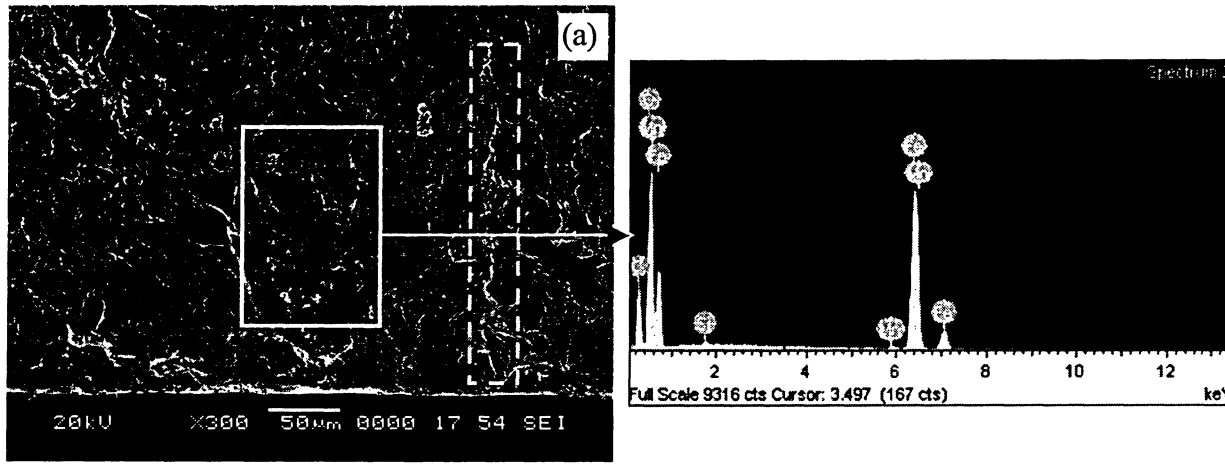
(a)
20kU X300 50µm 0000 17 54 SEI
Spectrum 2
2 4 6 8 10 12
Full Scale 9316 cts Cursor: 3.497 (167 cts)
keV

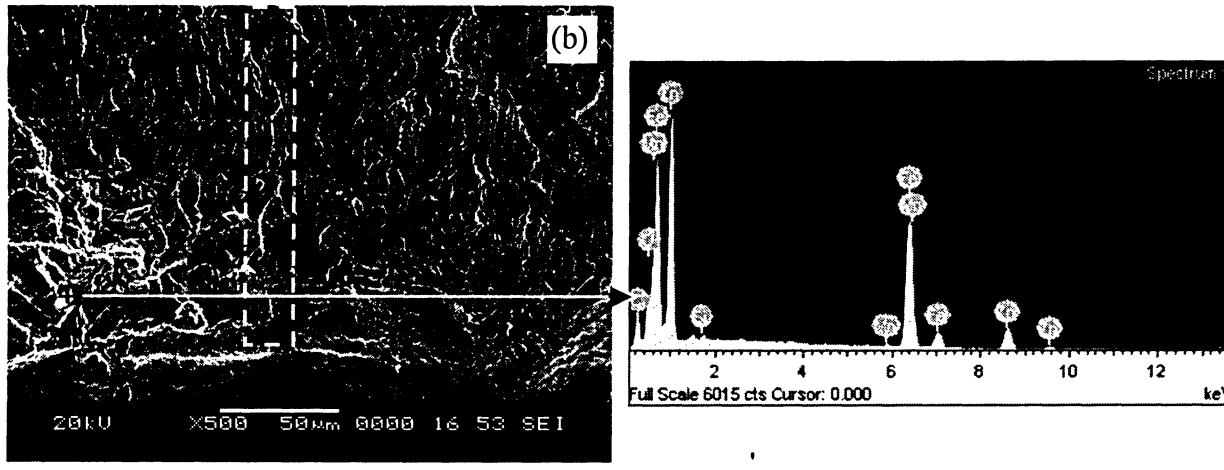
(b)
20kU X500 50µm 0000 16 53 SEI
Spectrum 1
2 4 6 8 10 12
Full Scale 6015 cts Cursor: 0.000
keV

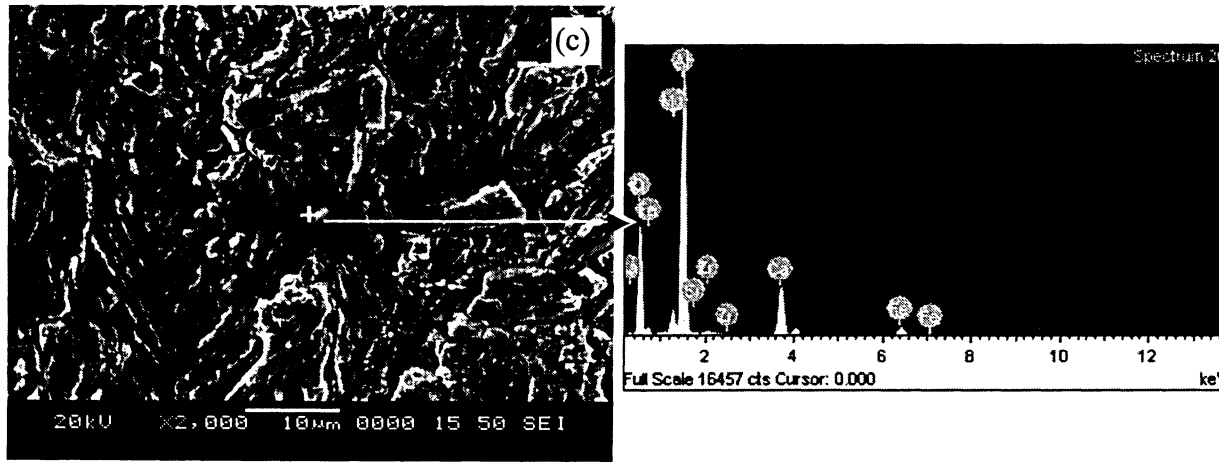
(c)
20kU X2,000 10µm 0000 15 50 SEI
Spectrum 26
2 4 6 8 10 12
Full Scale 16457 cts Cursor: 0.000
keV

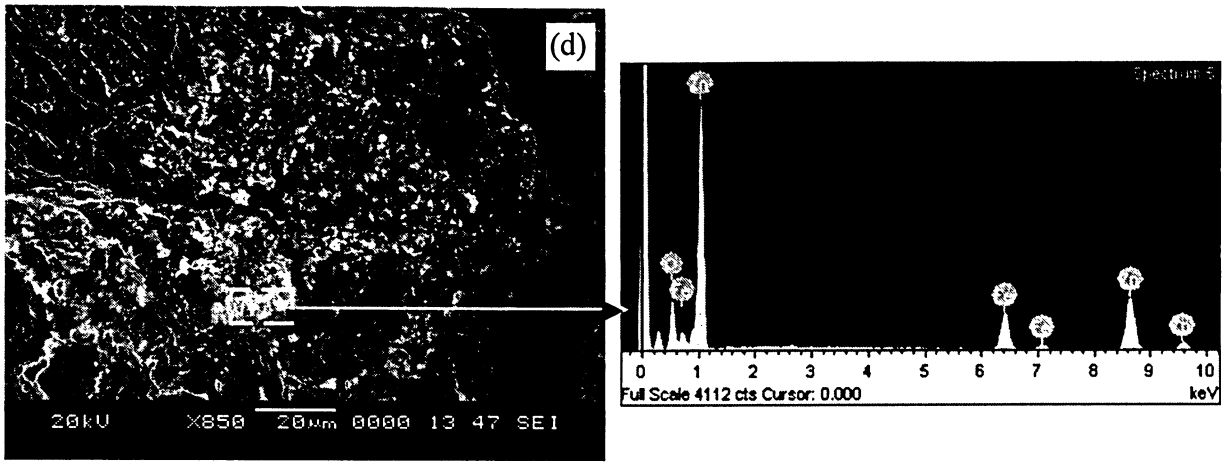

Figure 4.19 Different defects for the crack initiation for the sample welded with 8.35 kA and tested at the load level of region II in Figure 4.11. (a) Corrosion; (b) Zn oxide and carbide inclusion; (c) Al and Ca oxide inclusion; (d) Zinc coating effects.

Table 4.3 EDS analysis at defects on fracture surfaces.

	Element	C K	O K	Si K	Mn K	Fe K	Zn K	Mg K	Al K	Zr K	Ca K
(a)	Weight%	**24.67**	**35.37**	0.27	0.63	39.06	-	-	-	-	-
	Atomic%	**41.20**	**44.35**	0.19	0.23	14.03	-	-	-	-	-
(b)	Weight%	**22.94**	**13.51**	0.54	0.78	44.24	**18**	-	-	-	-
	Atomic%	**49.54**	**21.9**	0.5	0.37	20.55	**7.14**	-	-	-	-
(c)	Weight%	-	**49.08**	0.21	-	4.26	-	3.03	**33.38**	0.98	9.07
	Atomic%	-	**64.58**	0.16	-	1.60	-	2.62	**26.05**	0.23	4.77
(d)	Weight%	-	**19.77**	-	-	17.20	**63.03**	-	-	-	-
	Atomic%	-	**49.27**	-	-	12.28	**38.45**	-	-	-	-

The theoretical stress distribution was calculated to identify the initial position of the cracks. First, the section of a spot welded specimen was modelled as shown in Figure 4.20(a).

Let $ob = 1$, then

$$ab = 1/\sin\theta \tag{4.2}$$

$$\sigma_{rr}\cos\theta = \sigma_{\theta\theta}\sin\theta \tag{4.3}$$

$$\sigma = \sigma_{rr} ab\sin\theta + \sigma_{\theta\theta} ab\cos\theta \tag{4.4}$$

Substituting Eq. (4.2) and (4.3) into Eq.(4.4) yields:

$$\sigma_{rr} = \frac{\sigma}{1+\cot^2\theta} \tag{4.5}$$

From Eq.(4.5),

For $\theta = 0, \pi$, $\cot^2\theta = \infty$, $\sigma_{rr} = 0$

For $\theta = \pi/2$, $\cot^2\theta = 0$, $\sigma_{rr} = \sigma_{\max} = \sigma$

Therefore, the stresses at point A and D in Figure 4.20(a) are the maximum stress.

Secondly, to explain why the crack initiation occurred from the inside of the nugget, the distribution of the stresses in the thickness section need to be considered as shown in Figure 4.20(b). The equations for the tensile, shear stress, and bending moment as shown in Figure 4.20(b) (I & II) are as follows,

$$\sigma = F/A_{cross} \tag{4.6}$$

$$\tau = F/A_{nugget} \tag{4.7}$$

$$M = \int_0 x\sigma dx = \frac{t^2\sigma}{2} \tag{4.8}$$

where, F is the applied force, A_{cross} is the area calculated with sheet thickness and nugget diameter, A_{nugget} is the area with πr^2, r is the nugget radius, M is the moment, t is the thickness.

From the equilibrium equation, the maximum value of shear stress $\tau(x)$ as shown in Figure 4.20(b) (III) is located on the AD plane while zero on the BC plane; the maximum value of tensile stress $\sigma(x)$ as shown in Figure 4.20(b) (IV) is located on the AF plane while zero on the DE plane. The compressive stress (σ_c) as shown in Figure 4.20(b) (V) results from the bending moment (M) as follows,

$$\sigma_c = \frac{My}{I} = \frac{My}{\pi r^2/16} \tag{4.9}$$

Where r is the radius of the nugget, y is the distance from the centre of the nugget.

Therefore, the triaxial stresses at points A and D in Figure 4.20(b) reached the maximum value from the analysis for both sections. The crack initiation would normally occur at points A or D.

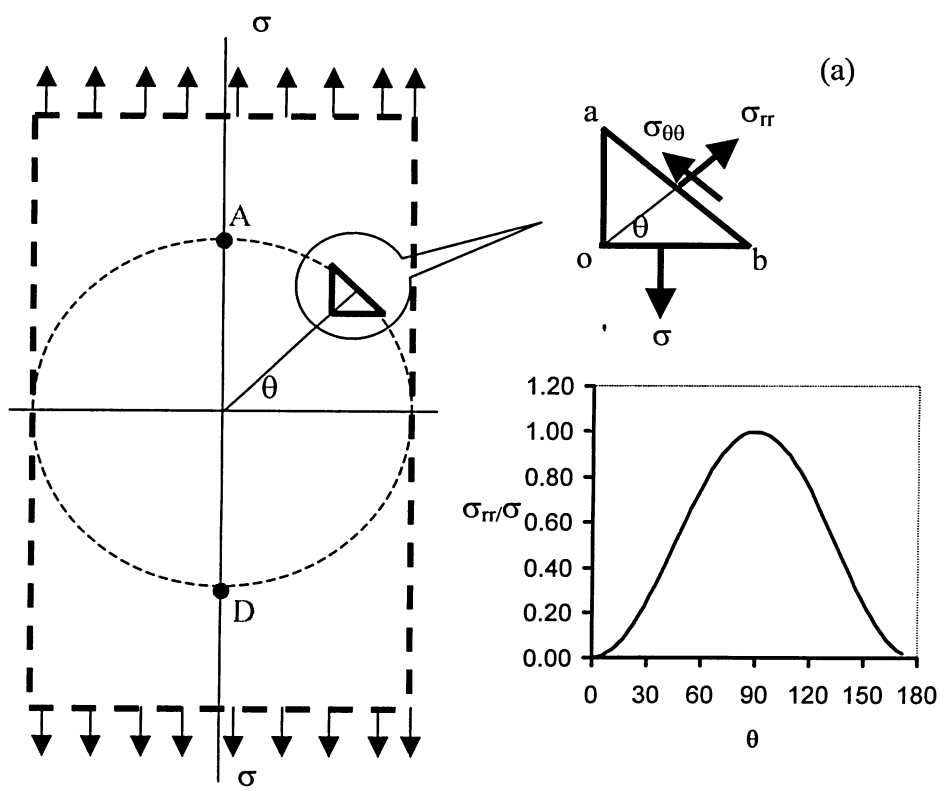

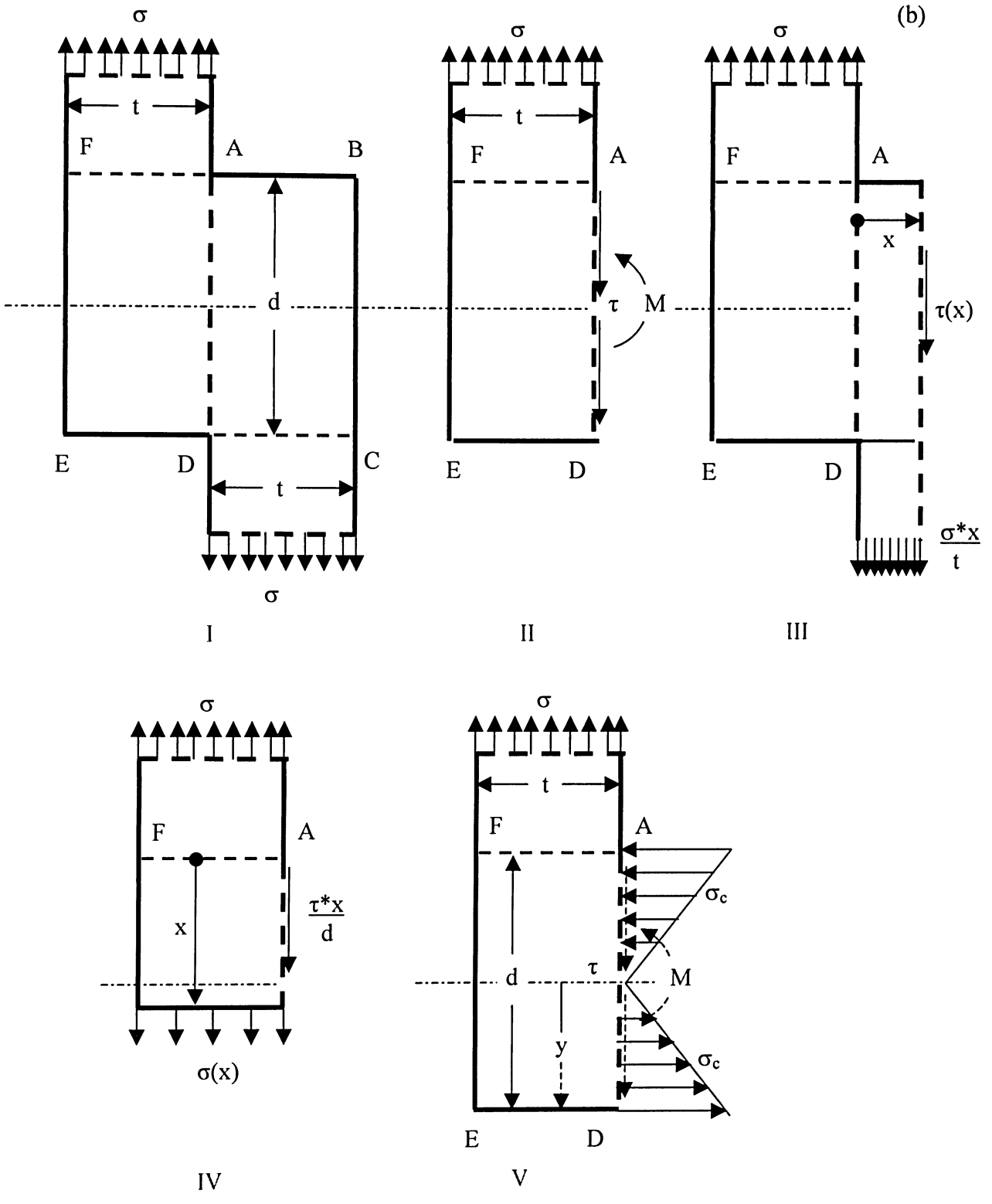

Figure 4.20 Stress analysis in the nugget. (a) View in the spot weld direction; (b) Side view perpendicular to the spot weld direction.

4.2.6 Interfacial Fracture Analysis

Figure 4.21 shows a typical interfacial failure mode in high load tests. Figure 4.21(a) shows a low magnification secondary electron image (SEI) of the failed nugget. Obviously, there are macro-voids or existing cracks in the weld which possibly decrease the weld properties [50,53,54]. Figure 4.21(b) is a high magnification view of the round cave of Figure 4.21(a). The subsequent Figure 4.21(c) reveals part of the weld exhibiting the characteristics of a ductile fracture, as shown in Figure 4.21(e) and (f), and part of the weld exhibiting the brittle fracture – dendrite structure, as shown in Figure 4.21(d), which presents direct evidence that this defect resulted from the solidification shrinkage.

It is not a simple case that the interfacial fracture mode presents a low tensile strength since some ductile regions were observed in this fracture mode. Shrinkage voids are not considered as the only cause for the interfacial fracture, although there are some methods available to control the voids by changing process parameters, including increasing the electrode force, welding time or current in the proper range [53,54]. The interfacial fracture was also linked to the steel compositions, as well from the carbon equivalent (CE). According to the Nippon Steel CE formula and GM CE formula [53,76], 0.242% and 0.367% of CE for DP600 were calculated from Eq.4.10 and Eq.4.11,

$$CE = C + \frac{Si}{30} + \frac{Mn}{20} + 2P + 4S \tag{4.10}$$

$$CE = C + \frac{Mn}{6} \tag{4.11}$$

The higher carbon equivalent from other elements of silicon, manganese, etc., makes the weld hard and brittle, and increases the boundary energy to easily cause the solidification cracks. Eq.4.10 also suggested the weld will fail interfacially if CE is greater than 0.24% [53].

The process parameters are important factors since the interfacial fracture tends to occur for a smaller current or shorter welding time [53]. As first part of this study [58], the most important period for zinc melting and expeling from the nugget is the first 3 to 4 cycles. By observing the fracture surface from a small current group for dendrites, some white spots with rich zinc were found, as shown in the broken square of Figure 4.21(d). Another factor contributing to the brittleness is the microstructure itself. As mentioned above in the section "Microstructural variations and imperfections", the subsequent rapid cooling results in a weld with a martensite structure because of the higher level of carbon and alloying elements. The presence of hard martensite essentially allows easier propagation of cracks and more easily generates interface failures [67].

Therefore, the main reasons for interfacial fracture would be: (I) void/dendrite microstructure; (II) presence of zinc in the centre of the nugget; (III) higher carbon equivalent; (IV) lath martensite microstructure in the fusion zone.

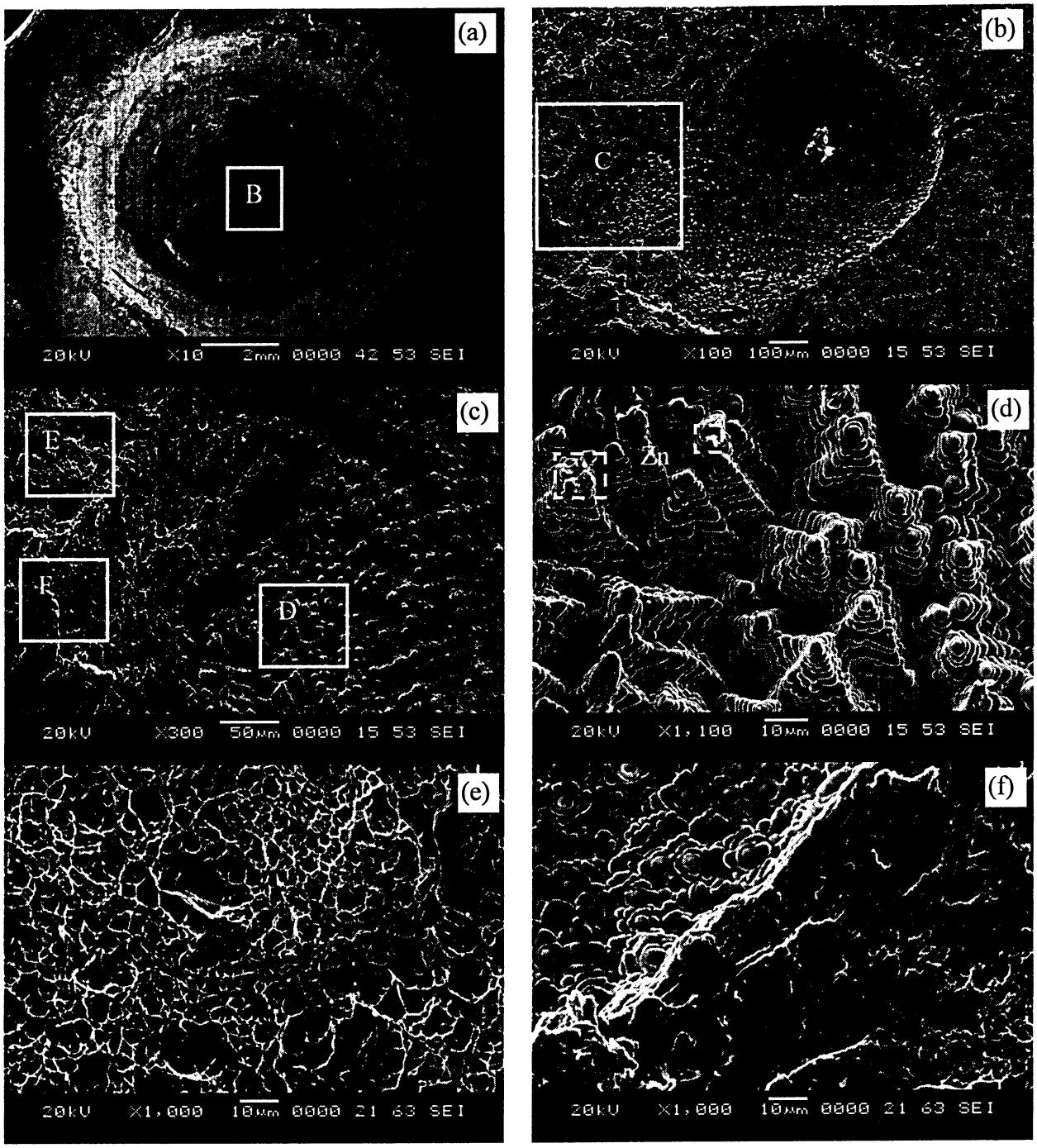

Figure 4.21 Interfacial fracture with dendrite and ductile microstructure. (a) View of low magnification; (b, c) Magnified view of the nugget with dendrite and ductile microstructure. (d) Dendrite. (e) Ductile microstructure. (f) Dendrite and ductile combination area. Where the locations of micrographys (a), (b), (c), (d), (e), (f) are indicated by A, B, C, D, E, F with sample welded with 8.35 kA and tested at the load level of region I in Figure 4.11.

CHAPTER 5

CONCLUSIONS

5.1 Summary

A data acquisition system used to monitor the process of RSW of Zn-coated automotive advanced high strength steels was developed. The output signal features of five variables were identified and correlated to the different stages of weld nugget formation, especially for the welding expulsion. The dynamic resistance, electrode force, and displacement were characterized for an HDG DP600 steel. The following conclusions can be drawn.

1. Output voltage and current signals should not be used to identify expulsion, since no obvious changes could be identified.

2. When the expulsion occurs, the signals of the dynamic resistance, electrode force, and displacement all experience a sudden drop.

3. Monitoring and controlling the slope of the resistance curve between the bottom and the highest peak during a specific period is a proper process control strategy.

4. The rate of increase of the force to the peak and the rate of decrease of the force curve are also a possible process control strategy except for the higher cost of the force transducer and its placement.

5. The average increasing rate of the displacement or the total displacement could also be used for process monitoring and control.

6. Of the three possible control strategies proposed, especially with AC welding equipment, the resistance signal is easily obtained and the least expensive, the force sensor is the least intrusive from the industry viewpoint, and the displacement sensor is most suitable for the research environment.

After examining the expulsion features, the fracture characteristics of spot welded specimens were investigated via both tensile shear tests and fatigue tests.

1. In the static tensile shear tests, the maximum load carried by the group (8.1 – 8.3 kA) reached the highest value. The specimens with the expulsion exhibited a lower load. Even when interfacial fracture occurred, the load-bearing ability of the weld was still high.

2. Fatigue tests showed a weaker trend for the group with the expulsion. Four typical fatigue cracking modes have been observed. At the very high load level, the crack can either be interfacial failure, or initiate away from the nugget and fail with plastic deformation. At the very low load level close to the fatigue limit, the cracks initiate at the nugget root, penetrate through the thickness and propagate in a straight line in the base metal. At the intermediate load level, the cracks initiate at the nugget root and propagate along about 10% to 50% of the circumference and finally into the base metal.

3. For both tensile shear and fatigue tests, the crack initiation was observed to occur basically at the boundary of the nugget at the interface between two sheets close to the clamping grips of the Instron test machine. It was also verified from a theoretical stress analysis, since the triaxial stresses reached maximum at that location.

4. Fusion zone and HAZ mainly consisted of domains of the martensite, with fine domains of martensite in the HAZ and coarse domains of lath martensite in the fusion zone.

5. Improper process parameters led to the presence of voids or cracks from solidification, and dendrite microstructure with zinc diffusion in the nugget and thus resulted in interfacial fracture under the applied static or cyclic loading.

5.2 Recommendations for Future Work

1. Carry on experiments to verify the proposed strategies for other AHSS steels (such as TRIP 590, 780) with the same thickness sheets.

2. Develop methods for expulsion monitoring and control in RSW of dissimilar thickness AHSS steels.

3. Examine the fracture characteristics and mechanisms of different AHSS grades using tensile shear tests, fatigue tests, and other mechanical testing.

References

[1] H. Curt: Great Design in Steel Seminar on 'The future revolution in Automotive High Strength Steel Usage', Livonia, Michigan, USA, February 2004, Track-Two.

[2] ULSAB-AVC Consortium: Technical Transfer Dispatch #6 – Body Structure Materials, May 2001.

[3] W. Li: 'Monitoring And Diagnosis Of Resistance Spot Welding Process', PhD thesis, University Of Michigan, USA, 1999.

[4] N. T. Williams and J. D. Parker: International Materials Reviews, 2004, 2, 45-75.

[5] J. Senkara, H. Zhang, and S. J. Hu: Welding Journal, 2004, 4, 123s-132s.

[6] C.-S. Chien and E. Kannatey-Asibu,Jr.: Welding Journal, 2002, 9, 195s-199s.

[7] H. Zhang: Welding Research Supplement, 1999, 11, 373s-380s.

[8] RWMA: Resistance Welding Manual, 4th Edition, 1989. Sec.1&3.

[9] A. Lee and G. Nagel: 'Basic phenomenon in resistance spot welding', Report 880277, SAE, Detroit, USA, 1988.

[10] S. A. Gedeon, C. D. Sorensen, K. T. Ulrich and T. W. Eagar: Welding Research Supplement, 1987, 12, 378s-385s.

[11] D. W. Dickinson, J. E. Franklin and A. Stanya: Welding Research Supplement, 1980, 6, 170s-176s.

[12] J. E. Gould and W. A. Peterson: 'Resistance Welding Research Evaluations of Coated Steels, Part Two, Dynamic Resistance Studies', Research Report MR8809, Edison Welding Institute, Ohio, USA, 1988.

[13] J. E. Gould and W. A. Peterson: 'Resistance Welding Research Evaluations of Coated Steels, Part Three, Nugget Development Studies', Research Report MR8814, Edison Welding Institute, Ohio, USA, 1988.

[14] S. A. Gedeon and T. W. Eagar: Metallurgical Transactions B, 1986, 12, 887-901.

[15] S. A. Gedeon and T. W. Eagar: Metallurgical Transactions B, 1986, 12, 879-885.

[16] J. E. Gould: Welding Journal, v66, 1, 1987, 1s-10s.

[17] M. Hao, K. A. Osman, D. R. Boomer, and C. J. Newton: Welding Research Supplement, 1996, 1, 1s-8s.

[18] Y. Cho and S. Rhee: Welding Journal, 2002, 6, 104s-111s.

[19] S. J. Vahaviolos, M. F. Carlos, S. J. Slykhous, and S. J. Ternowchek: Materials Evaluation, 1981, 10, 1057-1060.

[20] S. Satonaka and K. Matsuyama: Welding in the World, 2000, 44, 4-10.

[21] N. Blumentritt: Welding in the World, 2002, 46, 297-307.

[22] I. Tatsukawa, S. Satonaka, M.Yamamoto: Quarterly Journal of the Japan Welding Society, v 6, n 2, 1988, 109-114.

[23] D. F. Farson, J. Z. Chen, K. Ely and T. Frech: Science and Technology of Welding and Joining, 2003, 6, 431-436.

[24] P. Podrzaj, I. Polajnar, J. Diaci, and Z. Kariz: Measurement Science and Technology, 2004, 15, 592-598.

[25] G. L. Meur, B. Bourouga and T. Dupuy: Science and Technology of Welding and Joining, 2003, 6, 415-422.

[26] M. Jou: Journal of Materials Processing Technology, 2003, 132, 102-113.

[27] M. Hao, K. A. Osman, D. R. Boomer, C. J. Newton, and P. G. Sheasby: 'On-Line Nugget Expulsion Detection for Aluminum Spot Welding and Weldbonding', Report 960172, SAE, Detroit, USA, 1996.

[28] C. T. Ji and Y. Zhou: Journal of Manufacturing Science and Engineering, 2004, 126, 605-610.

[29] S. H. Lalam and S. Agashe: Sheet Metal Welding Conf., Sterling Heights, MI, USA, May 2004, Ispat Inland Inc..

[30] C. L. Tsai, W. L. Dai, and D. W. Dickinson: 'Analysis and Development of A Real-Time Control Methodology in Resistance Spot Welding', Report 910191, SAE, Detroit, USA, 1991.

[31] D. J. Browne, H. W. Chandler, J. T. Evans and J. Wen: Welding Research Supplement, 1995, 10, 339s-344s.

[32] A. De: Science and Technology of Welding and Joining, 2002, 2, 119-124.

[33] A. De and M. P. Theddeus: Science and Technology of Welding and Joining, 2002, 2, 111-118.

[34] J. A. Khan, L. Xu and Y. –J. Chao: Science and Technology of Welding and Joining, 1999, 4, 201-207.

[35] S. C. Wang and P. S. Wei: Transactions of the ASME, 2001, 123, 576-585.

[36] D. J. Browne, H. W. Chandler, J. T. Evans, P. S. James, J. Wen and C. J. Newton: Welding Research Supplement, 1995, 12, 417s-422s.

[37] A. G. Livshits: Welding Research Supplement, 1997, 9, 383s-390s.

[38] F. Lu and P. Dong: Science and Technology of Welding and Joining, 1999, 5, 285-289.

[39] J. Peng, S. Fukumoto, L. Brown and N. Zhou: Science and Technology of Welding and Joining, 2004, 4, 331-336.

[40] B. H. Chang, Y. Zhou, I. Lum and D. Du: Science and Technology of Welding and Joining, 2005, 1, 61-66.

[41] W. Li: Journal of Manufacturing Science and Engineering, 2005, 127, 709-717.

[42] H. Tang, W. Hou, S. J. Hu, H. Y. Zhang, Z. Feng and M. Kimchi: Welding Journal, 2003, 5, 116s-124s.

[43] Electrode Wear Mechanisms Task Force: ' Finite Element Modelling of Electrode Wear Mechanisms ', Technical report, Auto/Steel Partnership, Michigan, USA, 1995.

[44] K. Haefner, B. Carey, B. Bernstein, K. Overton, and M. D'Andrea: Transactions of The ASME, 1991, 113, 104-112.

[45] K. Araki, X. Chen, J. Chen, Y. Ishino, and T. Mizuno: Proceedings of the SICE Annual Conference, 1996, 1139-1144.

[46] X. Chen, K. Araki, and T. Mizuno: Proceedings of the 36th SICE Annual Conference, No.97TH8323, 1997, 989-994.

[47] S. Lee, Y. Choo, T. Lee, C. Han, and M. Kim: IEEE Industry Applications Conference of 35th IAS Annual Meeting and World Conference on Industrial Applications of Electrical Energy, No.00CH37129,,2000, 2, 1210-1216.

[48] Standardized Welding Test Method Task Force: 'Joining Technologies: Weld Quality Test Method Manual', Technical report, Auto/Steel Partnership, Michigan, USA, 1997.

[49] P. Howe and S. Kelley: 'A Comparison of the Resistance Spot Weldability of Bare, Hot-dipped, Galvannealed, and Electrogalvanized DQSK sheet steels', Report 880280, SAE, Detroit, USA, 1988.

[50] M. Milititsky, E. Pakalnins, C. Jiang, and A. K. Thompson: 'On Characteristics of DP600 Resistance Spot Weld', Report 2003-01-0520, SAE, Detroit, USA, 2003.

[51] W. Peterson, I. Accorsi, and T. Coon: Sheet Metal Welding Conf. XII on 'Review of Weld Mechanical Property Specification Requirements in AWS D8.1', MI, USA, May 2006, Paper 1-3.

[52] G. Wang and M. E. Barkey: : Welding Journal, 2006, 85, 84s-90s.

[53] M. Marya and X. Q. Gayden: Welding Journal, 2005, 80, 172s-182s.

[54] A. Joaquin, A. Elliott, and C. Jiang: Sheet Metal Welding Conf. XII on 'Reduction of Shrinkage Voids in RSW of AHSS', MI, USA, May 2006, Paper 1-2.

[55] R. W. Rathbun, D. K. Matlock, and J. G. Speer: Welding Journal, 2003, 53, 207s-218s.

[56] S. D. Sheppard and M. Strange: Fatigue and Fracture of Engineering Materials and Structures, 1992, 15(6), 531-549.

[57] J. F., Cooper and R. A. Smith: International Journal of Fatigue, 1985, 7(3), 137-140.

[58] C. Ma, S. D. Bhole, D. Chen, A. Lee, E. Biro, and G. Boudreau: Science & Technology of Welding & Joining, 2006, V11(4), 480-487.

[59] G. Tawade: 'Robust Schedules For Spot Welding Zinc-Coated Advanced High-Strength Automotive', M.A.Sc. thesis, Ryerson University, Canada, 2004.

[60] Japanese Standards Association: 'Method of Fatigue Testing for Spot Welded Joint', JIS-Z-3138, Japan, 1989.

[61] A/SP: 'Testing Procedure for Fatigue Testing of Spot Welded Coupons', June 2002.

[62] Leco Corporation: Metallography Principles and Procedures, 1977, MI, USA.

[63] Product information: http://www.jeolusa.com/sem/sem.html, July 2006.

[64] G. Lawes: 'Scanning Electron Microscopy and X-Ray Microanalysis', 5-25, 1987, Wiley_Interscience.

[65] Electrode Wear Mechanisms Task Force: 'Mechanisms of Electrode Wear During Resistance Spot Welding Hot-dipped Galvanized Steel', Technical report, Auto/Steel Partnership, Michigan, USA, 1994.

[66] M. Zhou: 'A Unified Approach to Assessing The Mechanical Performance of RSW', PhD thesis, University Of Michigan, USA, 2001.

[67] G. Shi and S. A. Westgate: Int. J. for the Joining of Materials, 2004, 16(1), 9-14.

[68] K. Easterling: 'Introduction to the Physical Metallurgy of Welding', 2nd Edition, 76-89&191-209; 1992, Butterworth Heinemann.

[69] J. E. Gould, S. P. Khurana, and T. Li: welding Journal, 2006, 85, 111s-116s.

[70] M. D. Tumuluru: Great Designs in Steel Conf. on 'Resistance Spot Welding of Coated High Strength Dual Phase Steel', MI, USA, March 2006, Paper T4-8.

[71] S. Kou: 'Welding Metallurgy', 2nd Edition, 263-295; 2002, Wiley_Interscience.

[72] B. Yan, H. Zhu, SH. Lalam, S. Baczkowski, and T. Coon: 'Spot Weld Fatigue of Dual Phase Steels', Report 2004-01-0511, SAE, Detroit, USA, 2004.

[73] Y. Yang, S. Khurana, F. Orth, W. Peterson, and S. S. Babu: Sheet Metal Welding Conf. XII on 'Development of an Integrated Computational Model to Predict the Performance of AHSS Spot Welds: Methodology and Challenges', MI, USA, May 2006, Paper 8-3.

[74] Y. J. Chao: Science & Technology of Welding & Joining, April 2003, 8(2), 133-137.

[75] J. C. McMahon, G. A. Smith, and F. V. Lawrence: ASTM Special Technical Publication, 1990, 1058, 47-77.

[76] M. L. Kuntz and J. C. Bohr: Sheet Metal Welding Conf. XII on ' Modelling Projection Welding of Fasteners to AHSS Sheet using Finite-Element Method', MI, USA, May 2006, Paper 8-6.

[77] JR. Cahoon, W. H. Broughton, and A. R. Kutzak: Metallurgical Transactions, 1971, Vol 21, p1979-1983

APPENDIX

Weld lobe data for DP600 to DP600 joints (1.24/1.24mm) at 18 cycles with 3.34 kN electrode force.

Time	Minimum Current (kA)			Expulsion Current (kA)			Avg. Min	Avg. Exp	Range
(Cycles)	L1	L2	L3	L1	L2	L3	(kA)	(kA)	(A)
18	6.7	6.67	6.68	8.42	8.34	8.3	6.68	8.35	1670
14	7.31	7.05	7.31	8.68	8.07	8.72	7.22	8.49	1267
10	7.73	7.74	7.77	8.98	8.63	9.24	7.75	8.95	1203

Lobe	Weld		Diameter		Current	Weld
#	Time	Min	Max	Mean	(kA)	Order
1	18	2.55	2.78	2.67	6.29	2
1	18	2.73	2.81	2.77	6.45	4
1	18	3.23	3.45	3.34	6.61	6
1	18	4.25	4.28	4.27	6.66	8
1	18	4.33	4.34	4.34	6.77	10
1	18	4.21	4.74	4.48	6.70	12
1	18	5.05	5.15	5.10	6.92	14
1	18	4.85	5.29	5.07	7.21	16
1	14	4.06	4.27	4.17	7.22	18
1	14	4.53	4.71	4.62	7.31	20
1	18	5.28	5.59	5.44	7.26	22
1	14	4.88	5.06	4.97	7.46	24
1	18	5.63	5.81	5.72	7.41	26
1	18	5.85	6.17	6.01	7.61	28
1	14	6.05	6.21	6.13	7.58	30
1	10	3.75	6.21	4.98	7.73	32
1	10	4.96	5.03	5.00	7.93	34
1	14	5.35	5.64	5.50	7.81	36
1	18	6.00	6.45	6.23	7.79	38
1	18	6.03	6.51	6.27	7.99	40
1	10	4.35	5.50	4.93	8.08	42
1	14	5.45	6.29	5.87	8.05	44
1	14	5.87	6.39	6.13	8.15	46
1	18	6.33	6.41	6.37	8.22	48
1	10	4.38	4.65	4.52	8.27	50
1	18	6.25	6.31	6.28	8.42	52
1	14	5.92	6.30	6.11	8.36	54
1	10	4.98	5.11	5.05	8.40	56
1	10	5.02	5.15	5.09	8.59	58

1	14	6.25	6.71	6.48	8.55	60
1	14	6.15	6.43	6.29	8.68	62
1	10	6.37	6.45	6.41	8.68	64
1	10	5.42	6.28	5.85	8.85	66
1	10	6.42	6.57	6.50	8.98	68
2	18	2.68	3.19	2.94	6.29	70
2	18	3.20	3.56	3.38	6.45	72
2	18	3.90	4.16	4.03	6.54	74
2	18	4.47	4.65	4.56	6.67	76
2	18	4.64	4.72	4.68	6.83	78
2	14	4.46	4.53	4.50	7.05	80
2	18	4.98	5.17	5.08	6.98	82
2	18	5.41	5.87	5.64	7.09	84
2	14	4.51	4.68	4.60	7.27	86
2	18	5.11	5.52	5.32	7.35	88
2	14	4.70	5.09	4.90	7.42	90
2	10	3.35	3.43	3.39	7.57	92
2	10	3.30	3.61	3.46	7.72	94
2	14	4.76	5.38	5.07	7.60	96
2	18	5.96	6.25	6.11	7.51	98
2	14	5.39	5.93	5.66	7.58	100
2	18	6.73	6.95	6.84	7.66	102
2	10	4.30	5.11	4.71	7.74	104
2	14	5.51	5.63	5.57	7.88	106
2	10	4.54	4.61	4.58	7.90	108
2	18	5.74	6.60	6.17	8.34	110
2	10	6.05	6.54	6.30	7.91	112
2	14	6.58	6.76	6.67	7.89	114
2	14	5.94	6.57	6.26	8.07	116
2	10	4.65	4.90	4.78	8.17	118
2	10	4.72	5.29	5.01	8.36	120
2	10	5.34	6.41	5.88	8.57	122
2	10	5.66	6.23	5.95	8.63	124
3	18	3.68	4.15	3.92	6.22	126
3	18	3.39	3.77	3.58	6.45	128
3	18	3.98	4.30	4.14	6.52	130
3	18	4.10	4.59	4.35	6.62	132
3	18	4.45	4.68	4.57	6.68	134
3	18	4.65	4.71	4.68	6.91	136
3	14	3.66	3.91	3.79	6.97	138
3	14	3.98	4.26	4.12	7.21	140
3	18	5.31	5.74	5.53	7.13	142
3	14	4.48	4.75	4.62	7.31	144
3	18	5.37	5.85	5.61	7.31	146
3	18	5.47	6.29	5.88	7.46	148
3	14	4.86	5.01	4.94	7.45	150
3	14	5.04	5.40	5.22	7.57	152
3	18	5.89	6.22	6.06	7.60	154

3	10	3.59	3.76	3.68	7.71	156
3	10	4.46	4.53	4.50	7.77	158
3	14	5.19	5.87	5.53	7.89	160
3	18	6.03	6.75	6.39	7.76	162
3	18	6.06	6.86	6.46	7.84	164
3	14	5.95	6.41	6.18	7.99	166
3	10	4.45	4.77	4.61	7.99	168
3	14	5.71	6.63	6.17	8.11	170
3	10	4.59	5.13	4.86	8.08	172
3	18	6.26	6.59	6.43	8.30	174
3	10	4.78	4.81	4.80	8.34	176
3	14	5.71	6.47	6.09	8.35	178
3	14	5.93	6.81	6.37	8.56	180
3	10	4.83	4.87	4.85	8.58	182
3	10	5.40	6.21	5.81	8.71	184
3	14	5.96	6.54	6.25	8.72	186
3	10	5.15	5.99	5.57	8.90	188
3	10	5.38	6.38	5.88	9.09	190
3	10	6.27	6.51	6.39	9.24	192

Chao Ma

EDUCATION:

Master of Applied Science (2006)
Ryerson University, Toronto, ON, Canada
Major: Mechanical Engineering, GPA: 4.07/4.33

Dual Bachelor of Engineering (1995 &1996)
Harbin Institute of Technology, Harbin, China
Majors: Material Science and Engineering, 80%
Computer and Electrical Engineering, 80%

EXPERIENCE:

Work experience trainee, May 2005 – Jan 2006
Dofasco Inc., Hamilton, ON, Canada

Teaching assistant, Sep. 2004 – Aug. 2006
Ryerson University, Toronto, ON, Canada

Product engineer and manager, 1999 – 2003
Ramaxel Tech. Inc., Shenzhen, China

PUBLICATIONS:

1. C. Ma, S.D. Bhole, D.L. Chen, A. Lee, E. Biro, and G. Boudreau "Expulsion Monitoring in Spot Welded AHSS Auto steels", Journal of Science and Technology of Welding and Joining, 2006, V11, 4, 480-487.
2. C. Ma, D.L. Chen, S.D. Bhole, G. Boudreau, E. Biro and A. Lee, "Fracture Characteristics of Spot Welded AHSS Auto Steels" The 2nd journal paper has been prepared to be submitted.
3. C. Ma, S.D. Bhole, D.L. Chen, G. Boudreau, A. Lee, and E. Biro "Expulsion Investigation in RSW of AHSS Auto steels", 18th Canadian Materials Science Conference, Jun 2006, Montreal, Canada. Abstract Book Edited by M. Brochu, p72-73.
4. C. Ma, "Expulsion monitoring in RSW of DP600", Winner of Poster Competition in Sheet Metal Welding Conference XII, May 2006, Livonia, Michigan, USA. Photo Available Online: http://www.awsdetroit.org/